

---

# Thermal expansion of carbon structures

---

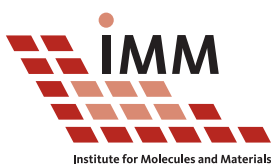
Leendertjan Karssemeijer

Master Thesis

August 2010

*Supervisor:*  
Prof.dr. A. Fasolino

*External advisor:*  
Dr.ir. G.A. de Wijs



Institute for Molecules and Materials

Theory of Condensed Matter  
Institute for Molecules and Materials  
Radboud University Nijmegen

---



# Acknowledgments

First of all I want to express my thanks to my supervisor Prof. Dr. Annalisa Fasolino for her fantastic support during my master research. Despite of her very busy schedule, she always made time to see how I was doing and whenever I had questions she has pointed me in the right direction and motivated me with bright ideas.

Also, I would like to thank Jan Los for helping me with the Monte Carlo routines and explaining the features of the LCBOP<sub>II</sub> potential to me. Furthermore, I want to thank my roommates Misha Akhukov, Koen Reijnders, Linde van Heeringen and Jan-Pieter Boersma for many joyful conversations and a pleasant working environment throughout the year. Many thanks also to the rest of the research group for pleasant and helpful discussions, mainly during the coffee breaks.

Finally, I want to thank my parents for their support and motivation during my years at the university and my girlfriend Charlotte for making my life so much more enjoyable.



# Contents

<b>1</b>	<b>Introduction</b>	<b>1</b>
1.1	Carbon . . . . .	2
1.2	Graphene . . . . .	3
1.2.1	Crystal structure . . . . .	3
1.3	Graphite . . . . .	5
1.3.1	Crystal structure . . . . .	5
1.3.2	Multilayer graphene . . . . .	6
1.4	Carbon nanotubes . . . . .	7
1.4.1	Crystal structure . . . . .	7
1.5	LCBOPII Empirical potential . . . . .	11
<b>2</b>	<b>Atomistic simulations</b>	<b>13</b>
2.1	Monte Carlo simulations . . . . .	15
2.1.1	Results and discussion . . . . .	16
2.1.2	Wave Move Monte Carlo simulations . . . . .	23
2.2	Molecular Dynamics simulations . . . . .	25
2.2.1	Results and discussion . . . . .	25
<b>3</b>	<b>Lattice Dynamics</b>	<b>29</b>
3.1	Theory of lattice dynamics . . . . .	30
3.1.1	Quantization and normal coordinates . . . . .	31
3.1.2	Thermodynamic properties and the quasiharmonic approximation . . . . .	33
3.1.3	Numerical calculation of phonon dispersion relations . . . . .	34
3.1.4	Integration over the Brillouin zone . . . . .	36
3.2	Phonon dispersions . . . . .	37
3.2.1	The 1-dimensional carbon chain . . . . .	37
3.2.2	Graphene . . . . .	38
3.2.3	Graphite . . . . .	48
3.2.4	Bilayer graphene . . . . .	52
3.2.5	Carbon nanotubes . . . . .	52
3.3	Bending rigidity . . . . .	54
3.4	Free energy minimization and thermal expansion . . . . .	58
3.4.1	Graphene . . . . .	58
3.4.2	Graphite . . . . .	64
3.4.3	Bilayer graphene . . . . .	66
3.4.4	Calculations and results . . . . .	66
3.4.5	Carbon nanotubes . . . . .	67
3.5	Discussion of the quasiharmonic results . . . . .	70
<b>4</b>	<b>Summary and conclusions</b>	<b>71</b>



# Introduction

# 1

In the past two decades, enormous advances have been made in the field of carbon-based materials. The discovery of new, exotic allotropes such as buckyballs, carbon nanotubes and two-dimensional graphene has sprouted a great amount of scientific activity. These new materials were shown to have amazing electronic properties making them very promising candidates for applications in nanoelectronics. Carbon is even mentioned as the successor of silicon as the material of choice in the transistor industry. Despite the amount of conducted research however, the thermomechanical properties of these systems are still not fully understood.

As experiments are often difficult to perform on isolated samples of these nanometer-sized materials, computer simulations provide a great tool to gain more insight in their structural properties and stability at finite temperatures. Such knowledge is not only crucial in order to understand the electronic structure of these materials, it is also of fundamental importance, from a statistical mechanics point of view, to understand how these, often low-dimensional, materials can be stable.

In this thesis we will perform computer simulations based on a state-of-the-art description of carbon interactions in order to reveal more about the temperature dependence of the structure of these systems. Emphasis will lie on the thermal expansion of graphitic crystals and in particular of carbon nanotubes. The work is divided into the following four chapters:

*Chapter 1* gives a short introduction to the element carbon and the empirical potential LCBOPII which will be used to describe interactions between carbon atoms. The various crystalline forms of carbon which be studied in this thesis are also introduced.

*Chapter 2* describes, and gives the results of atomistic Monte Carlo and Molecular Dynamics simulations performed on single wall carbon nanotubes.

*Chapter 3* introduces the theory of lattice dynamics and discusses how it can be used to determine the coefficients of thermal expansion by free energy minimization. We present the results of the application of this theory to several graphitic crystals.

*Chapter 4* contains the conclusion, in which the most important results of this thesis will be summarized.

## 1.1 Carbon

The element carbon is one of the most interesting elements from the periodic table due to its great variety of allotropes and its unique role in nature.

Being the fourth most abundant element in the universe by mass makes carbon an important element in physical and chemical processes throughout the universe. But to us, humans, carbon is even more important. Its ability to form large, complicated networks makes carbon the basis element of organic chemistry and the backbone of all life as we know it. Without carbon, life as we know it would not exist.

From a physical point of view, carbon is also very interesting because of its many different forms which together span a large range of physical properties. From hard to soft, conducting to insulating, transparent to opaque etcetera. Today, carbon allotropes of all dimensionalities (from zero to three) are known to exist. The two three-dimensional crystalline phases, diamond and graphite, have been known to man for thousands of years and have countless applications in everyday life. Other three-dimensional forms of carbon include amorphous carbon and hexagonal diamond. In the late 1980's and early 1990's zero-dimensional buckyballs and one-dimensional carbon nanotubes were discovered. Only very recently (2004) has the two-dimensional carbon form, graphene, been observed experimentally for the first time.

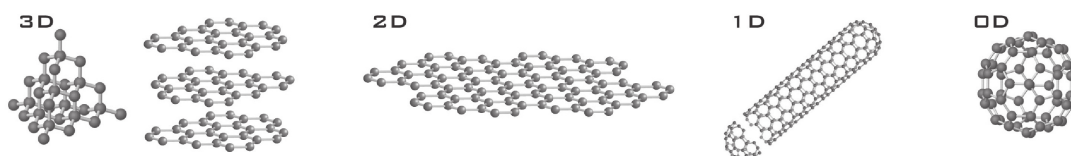


Figure 1.1: Carbon allotropes in all dimensions. From left to right: diamond and graphite, graphene, a nanotube and a buckyball. Picture from [1].

The reason why carbon can form so many different structures is that carbon atoms can form several types of valence bonds due to the hybridization of atomic orbitals. Carbon is the sixth element in the periodic table and thus has six electrons. Two of these occupy the  $1s^2$  orbital and are closely bound to the nucleus. The other four electrons are more weakly bound and have the electronic configuration  $2s^2 2p^2$ . These electrons are responsible for the covalent bonding with other atoms. In carbon, the energy difference between the  $2s$  and the  $2p$  orbitals is rather small compared to the binding energy between carbon atoms. This makes mixing of the wave functions possible in order to obtain a lower binding energy between the atoms. The mixing of one of the  $2s$  orbitals with  $n$   $2p$  orbitals is called  $sp^n$  hybridization. In carbon, three possible hybridizations occur:  $sp$ ,  $sp^2$  and  $sp^3$ . For more detailed information on the electronic wave functions of the hybridized orbitals we refer the reader to [2].

The  $sp$  hybridized bonds are mainly found in carbon-based molecules and linear carbon chains. The bonds in  $sp^2$  hybridized carbon systems form angles of  $120^\circ$  with each other, giving each carbon atom three nearest neighbours. This bond is one of the strongest in nature and it is found, among others, in graphite, graphene and carbon nanotubes. Carbon crystals such as these, which are predominantly bound by  $sp^2$ -bonds, are called graphitic crystals and they will be the subject of this thesis. The third hybridization,  $sp^3$ , is found for example in diamond. The carbon atoms have four nearest neighbours and form a tetragonal structure with angles of  $119.5^\circ$  between the bonds.

In this thesis we shall study the structural properties of the one-, two- and three-dimensional graphitic carbon allotropes at finite temperatures by means of computer simulations. In the subsequent sections the crystal structure of these carbon materials is further discussed.

## 1.2 Graphene

Graphene was discovered in 2004 by A. Geim and K. Novoselov as the world's first truly two-dimensional material [3]. It is a single layer of carbon atoms packed in a hexagonal lattice and it is the building block of all other graphitic materials such as graphite, carbon nanotubes and fullerenes.

Before the discovery of graphene it was always assumed that two-dimensional crystals could not exist due to the Mermin-Wagner theorem [4] which states that long-range order is destroyed at any finite temperature due to divergent contributions from thermal fluctuations. The discovery of graphene obviously required an explanation and nowadays it is believed that small height fluctuations, or 'ripples', in the carbon sheet suppress the thermal fluctuations making graphene a stable crystal even at finite temperatures [5].

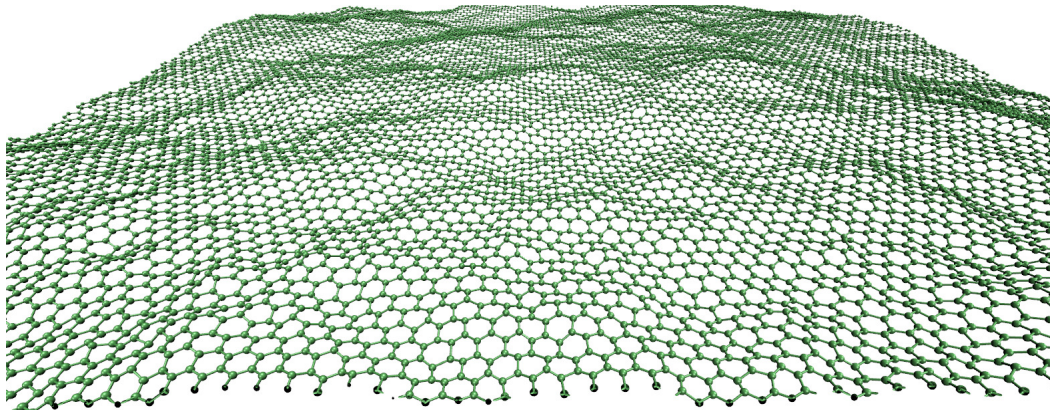


Figure 1.2: Graphene is a single sheet of carbon atoms packed in a honeycomb lattice. Sheets are rippled at any finite temperature to ensure structural stability. Shown is a simulation of a graphene sheet performed on the basis of the LCBOPII empirical potential [6].

Since its discovery graphene has attracted an enormous amount of scientific interest, mainly because of its unusual electronic properties. Its unique two-dimensional honeycomb lattice (in fact made up of two interpenetrating triangular lattices) gives rise to low energy quasiparticles described by a massless Dirac Hamiltonian (the speed of light replaced by an effective speed of about  $10^6 \text{ ms}^{-1}$ ) with a conical energy dispersion at the corners of the Brillouin zone. This makes graphene a perfect system for experiments on effects predicted by relativistic quantum mechanics such as Klein tunneling and the anomalous quantum Hall effect.

In this work however, we will not be interested in the electronic properties of graphene. Our interest is in its structural properties. Graphene represents the prototype membrane studied extensively in statistical mechanics and biochemical sciences. It is important to understand how such a system behaves and can remain structurally stable. Moreover, graphene is the building block of other graphitic crystals such as graphite and carbon nanotubes. In order to understand the properties of these systems it is important to first have a good understanding of graphene.

### 1.2.1 Crystal structure

It was already mentioned above that the crystal lattice of graphene is made up of two interpenetrating triangular lattices. We will call these sublattices  $A$  and  $B$ . This means that graphene in fact has a triangular lattice with a two atom basis. The atoms in sublattice  $A$  are located at  $\mathbf{R} = n\mathbf{a}_1 + m\mathbf{a}_2$  ( $n, m \in \mathbb{Z}$ ), where  $\mathbf{a}_1$  and  $\mathbf{a}_2$  are the two primitive translation vectors as shown in figure 1.3:

$$\mathbf{a}_1 = a \begin{pmatrix} 1 \\ 0 \end{pmatrix}, \quad \mathbf{a}_2 = \frac{a}{2} \begin{pmatrix} 1 \\ \sqrt{3} \end{pmatrix}. \quad (1.1)$$

Here we use the standard notation as found in literature. The lattice parameter,  $a$ , is related to the distance between neighbouring carbon atoms  $a_{CC}$  by  $a = \sqrt{3}a_{CC}$ . The value of  $a_{CC}$  is about 1.42 Å. The atoms in sublattice  $B$  are connected to the sublattice  $A$  atoms by the vector  $\delta$ :

$$\delta = \frac{a}{\sqrt{3}} \begin{pmatrix} 0 \\ 1 \end{pmatrix}. \quad (1.2)$$

The reciprocal lattice vectors  $\mathbf{b}_j$  satisfy  $\mathbf{a}_i \cdot \mathbf{b}_j = 2\pi\delta_{ij}$  and are given by

$$\mathbf{b}_1 = \frac{2\pi}{\sqrt{3}a} \begin{pmatrix} \sqrt{3} \\ -1 \end{pmatrix}, \quad \mathbf{b}_2 = \frac{2\pi}{\sqrt{3}a} \begin{pmatrix} 0 \\ 2 \end{pmatrix}. \quad (1.3)$$

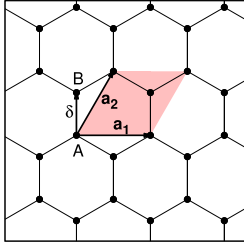


Figure 1.3: The graphene crystal has a triangular lattice with two atoms per unit cell, denoted by  $A$  and  $B$ , which are connected by the vector  $\delta$ . The lattice translation vectors are  $\mathbf{a}_1$  and  $\mathbf{a}_2$ . The shaded region is the unit cell.

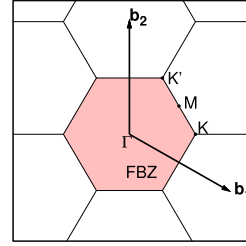


Figure 1.4: Reciprocal lattice of graphene. The shaded region is the first Brillouin zone and the high symmetry points  $M$ ,  $K$  and  $K'$  are also indicated.

The first Brillouin zone (FBZ), shown in figure 1.4, also has a hexagonal shape. There are a few special points with high symmetry in the FBZ also indicated in this figure. To begin with there is of course the zone center  $\Gamma$  where the wavevector  $\mathbf{q}$  is zero. The corners of the hexagon are called the  $K$  points, these are very important point in the electronic band structure of graphene because here the conduction and valence bands touch each other. There are six corners in the FBZ but only two are nonequivalent, namely  $K$  and  $K'$ . The other corners are connected to these two by the addition of a reciprocal lattice vector. The coordinates of  $K$  and  $K'$  are

$$\mathbf{K} = \frac{2\pi}{3a} \begin{pmatrix} 2 \\ 0 \end{pmatrix}, \quad \mathbf{K}' = \frac{2\pi}{3a} \begin{pmatrix} \sqrt{3} \\ 1 \end{pmatrix}. \quad (1.4)$$

Finally, the centers of the edges are called the  $M$  points, the  $M$  point shown in figure 1.4 is at

$$\mathbf{M} = \frac{\pi}{\sqrt{3}a} \begin{pmatrix} \sqrt{3} \\ 1 \end{pmatrix}. \quad (1.5)$$

## 1.3 Graphite

Graphite is one of the best known forms of carbon. People use it daily whenever they write with an ordinary pencil. Surprisingly perhaps it is also graphite, and not diamond, which has the lowest cohesive energy, and is thus the most stable form of carbon under standard conditions.

Graphite is a layered compound consisting of layers of graphene stacked on top of each other. This layered structure makes graphite a highly anisotropic material at atomic length scales, but also at macroscopic scales one can clearly see the effects of the layers. The simple fact that a graphite pencil works so well is because the van der Waals forces binding the layers together are very weak compared to the  $sp^2$  hybridized bonds binding the atoms in the layers themselves. This makes it very easy to slide off layers of graphite while moving a pencil across a piece of paper. Thermal and electrical conductivity are also highly anisotropic as a consequence of the layered structure.

### 1.3.1 Crystal structure

The crystal structure of graphene was already discussed in the previous section. Adding an extra dimension to the system also means introducing an extra lattice parameter. This parameter is called  $c$  and is equal to twice the distance between the graphene layers in graphite, its value is approximately 6.69 Å.

Graphene layers can be stacked on top of each other in a great number of different orientations. Normally two subsequent layers are oriented such that the atoms of the  $A$  sublattice of the upper layer are positioned directly above the atoms of sublattice  $B$  of the lower layer. This means that the atoms of sublattice  $B$  of the upper layer are positioned above the centers of the hexagons of the lower layer. This is shown in figure 1.5b). A third layer can be added on top of the second just as the second layer was placed on top of the first. These three different orientations are energetically the most favourable and the most common in nature, we will denote them by  $A$ ,  $B$  and  $C$ .

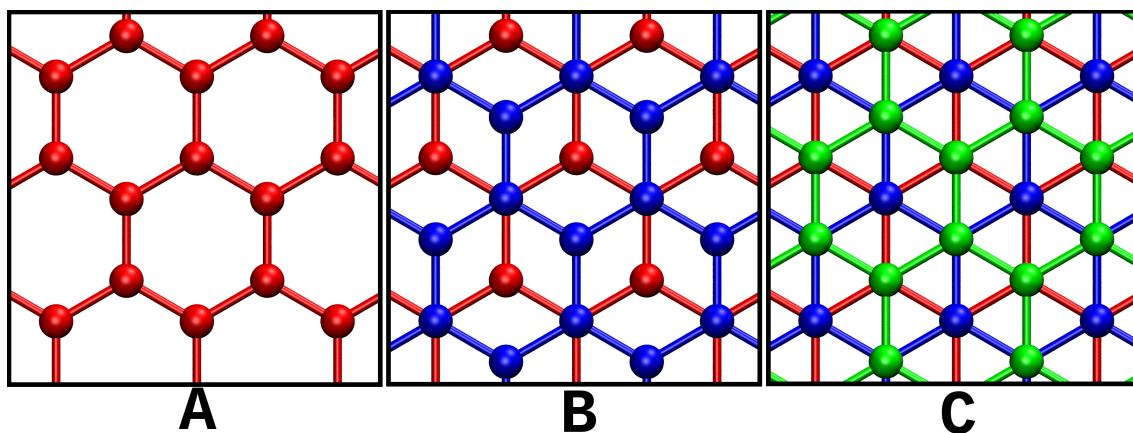


Figure 1.5: Top view of the three different orientations in which graphene sheets can be stacked. From left to right there is a single layer (stacking  $A$ ), two layers (stacking  $AB$ ) and three layers (stacking  $ABC$ )

The most abundant type of graphite is the so called Bernal stacking type in which the layers are stacked in an  $ABAB \dots$  pattern, 85% of all natural graphite has this stacking. This means that the unit cell has height  $c$  and will contain four carbon atoms, two in each layer. In the remainder of this work we will mean this type of stacking whenever we refer to graphite. Other possible stacking orders are simple hexagonal ( $AAA \dots$  stacking) which has two atoms per unit cell and is not found in natural graphite. Rhombohedral ( $ABCABC \dots$  stacking) graphite makes up for about 15% of natural graphite and has six atoms per unit cell. Finally there is turbostratic graphite in which the layers are oriented randomly on top of each other.

The in-plane primitive lattice vectors of graphite are the same as those of graphene, the new lattice vector has only one component in the  $z$ -component which is equal to  $c$  for Bernal stacked graphite. So

the primitive translation vectors of graphite are the following:

$$\mathbf{a}_1 = a \begin{pmatrix} 1 \\ 0 \\ 0 \end{pmatrix}, \quad \mathbf{a}_2 = \frac{a}{2} \begin{pmatrix} 1 \\ \sqrt{3} \\ 0 \end{pmatrix}, \quad \mathbf{a}_3 = \begin{pmatrix} 0 \\ 0 \\ c \end{pmatrix}. \quad (1.6)$$

Just like graphene, graphite also has a hexagonally shaped first Brillouin zone, the only difference being the addition of the third dimension. The FBZ is therefore a hexagon of height  $\frac{2\pi}{c}$ . The reciprocal lattice vectors are

$$\mathbf{b}_1 = \frac{2\pi}{\sqrt{3}a} \begin{pmatrix} \sqrt{3} \\ -1 \\ 0 \end{pmatrix}, \quad \mathbf{b}_2 = \frac{2\pi}{\sqrt{3}a} \begin{pmatrix} 0 \\ 2 \\ 0 \end{pmatrix}, \quad \mathbf{b}_3 = \frac{2\pi}{c} \begin{pmatrix} 0 \\ 0 \\ 1 \end{pmatrix}. \quad (1.7)$$

The high symmetry points in reciprocal space are the same as those of graphene, with the addition of the points  $A$ ,  $H$ , and  $L$  as shown in figure 1.6. The coordinates of the special points in reciprocal space are the following:

$$\begin{aligned} \mathbf{K} &= \frac{2\pi}{3a} \begin{pmatrix} 2 \\ 0 \\ 0 \end{pmatrix}, & \mathbf{K}' &= \frac{2\pi}{3a} \begin{pmatrix} \sqrt{3} \\ 1 \\ 0 \end{pmatrix}, & \mathbf{M} &= \frac{\pi}{\sqrt{3}a} \begin{pmatrix} \sqrt{3} \\ 1 \\ 0 \end{pmatrix}, \\ \mathbf{A} &= \begin{pmatrix} 0 \\ 0 \\ \frac{\pi}{c} \end{pmatrix}, & \mathbf{H} &= \begin{pmatrix} \frac{2\pi}{\sqrt{3}a} \\ \frac{2\pi}{3a} \\ \frac{\pi}{c} \end{pmatrix}, & \mathbf{L} &= \begin{pmatrix} \frac{\pi}{\sqrt{3}a} \\ \frac{\pi}{c} \end{pmatrix}. \end{aligned} \quad (1.8)$$

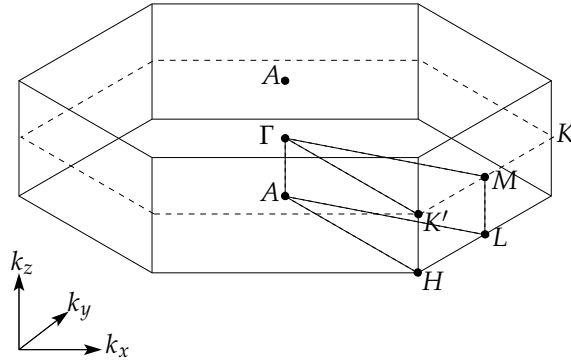


Figure 1.6: The first Brillouin zone of graphite.

### 1.3.2 Multilayer graphene

Whereas graphene consists of just a single layer and graphite has, in principle, an infinite amount of layers it is of course also possible to create a crystal with any finite number of graphene layers stacked in some order. These structures are referred to as multilayer graphene. Especially bilayer graphene, consisting of two graphene layers stacked on top of each other in  $AB$  order, is a very interesting system and has received a lot of scientific attention lately. This interest is mainly because of its electronic properties. In contrast to a single layer, bilayer graphene quasiparticles have a parabolic dispersion and has to possibility to open up a band gap which makes it a promising candidate for graphene-based electronic devices.

## 1.4 Carbon nanotubes

After the discovery of carbon buckyballs in 1985 ([7]) people started speculating whether or not one could also form tubes of graphitic carbon. These tubes would be some kind of limiting case of the buckyball. In 1991 carbon nanotubes were experimentally observed for the first time by S. Iijima using transmission electron microscopy [8]. This observation was of so called multi-wall carbon nanotubes (MWCNs) consisting of several single-wall carbon nanotubes (SWCNs) of different diameters nested inside one another. Only two years later, in 1993, the same group discovered SWCNs experimentally for the first time [9].

### 1.4.1 Crystal structure

What follows is a short description of the different types of SWCNs and their atomic structure. For a more detailed discussion we refer the reader to [2].

The structure of a single-wall carbon nanotube is most easily described by looking at the tube as a rolled up rectangular sheet of graphene. The vectors along which the graphene layer is ‘cut’ to form the rectangle determine the dimensions of the tube and the orientation of the hexagons with respect to the tube axis. One commonly distinguishes two different types of nanotubes, namely tubes which have a mirror plane parallel to the tube axis, achiral nanotubes, and tubes that do not, chiral nanotubes. There are two types of achiral nanotubes, namely armchair and zigzag nanotubes, named after the shape of their cross-sections perpendicular to the axis. There are in principle infinitely many chiral nanotubes. An example of each of the three basic nanotube types is given in figure 1.7. We will choose our Cartesian

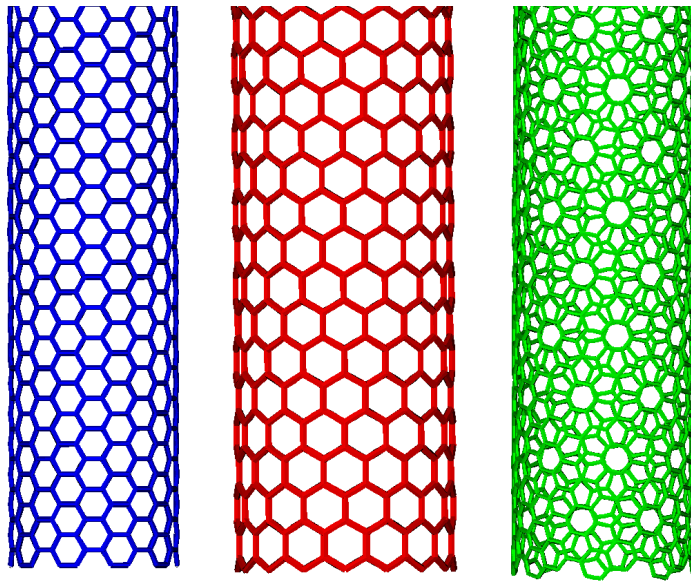


Figure 1.7: Three basic nanotube types, from left to right: achiral armchair (blue), achiral zigzag (red) and chiral (green)

coordinate system such that the axes of the nanotubes are along the  $z$ -direction. Furthermore we will only consider the structure of the unit cell of the nanotubes, as we can always stack multiple unit cells on top of each other to form longer tubes. To characterize the unit cell of a nanotube it is sufficient to specify one lattice translation vector of graphene, the so called chiral vector  $C$ , in the graphene sheet. This is the vector that will be rolled up to a circle when constructing the tube. The chiral vector is expressed in terms of the graphene basis vectors by means of two integers,  $n$  and  $m$ :

$$C = na_1 + ma_2. \quad (1.9)$$

A nanotube with a certain chiral vector is denoted as an  $(n, m)$  nanotube. As an example, the unrolled unit cell of a  $(4, 2)$  nanotube is shown in figure 1.8.

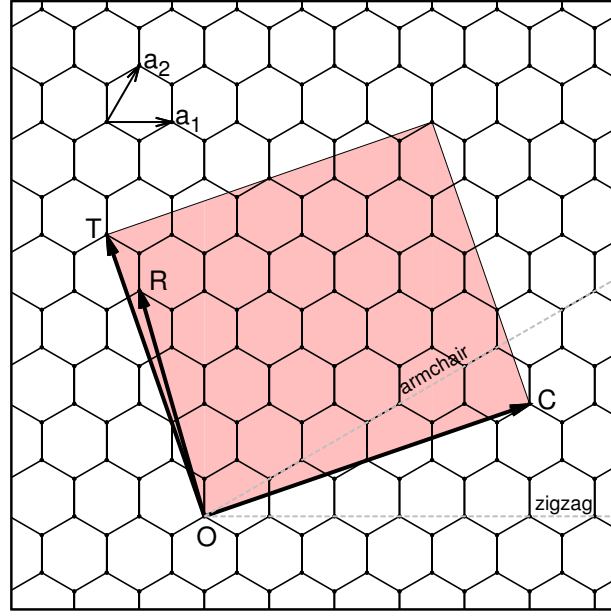


Figure 1.8: Unrolled unit cell of a (4,2) carbon nanotube spanned by the vectors  $C$  and  $T$ . The unit cell is entirely determined by the chiral vector  $C = na_1 + ma_2$ . Dotted lines indicate the directions of the chiral vector for  $(n,0)$  zigzag, and  $(n,n)$  armchair nanotubes. The vector  $R$  is the symmetry vector discussed in the text.

Due to the hexagonal symmetry of the honeycomb lattice it is sufficient to restrict the choice of  $n$  and  $m$  such that they satisfy  $0 \leq m \leq n$ . We define the chiral angle  $\theta_C$  as the angle  $C$  makes with  $a_1$ . The symmetry of the graphene sheet limits  $\theta_C$  between 0 and 30 degrees. To complete our rectangular sheet we need to construct the vector  $T$ , which is the smallest lattice translation vector perpendicular to  $C$ . The perpendicularity condition ensures that the sheet is rectangular so it can be rolled up to form a tube of constant radius. The requirement that  $T$  is the smallest lattice translation vector ensures that we obtain just one unit cell of the nanotube.

The  $T$  vector will remain parallel to the nanotube axis when the sheet is rolled up. In terms of the graphene basis vectors it is written as

$$T = t_1 a_1 + t_2 a_2. \quad (1.10)$$

To find  $t_1$  and  $t_2$  we rotate  $C$  by 90 degrees and equate the resulting vector to  $T$  times a constant  $A$ . This gives the following two equations:

$$\begin{aligned} t_1 + t_2 &= \frac{A}{\sqrt{3}}(m - n), \\ t_1 - t_2 &= \sqrt{3}A(n + m), \end{aligned} \quad (1.11)$$

with the following solution

$$\begin{aligned} t_1 &= \frac{1}{g}(n + 2m), \\ t_2 &= -\frac{1}{g}(2n + m), \end{aligned} \quad (1.12)$$

where  $g$  is the greatest common divisor of  $n + 2m$  and  $2n + m$ . Since the vector  $T$  remains parallel to the axis of the nanotube, its length is also the length of the nanotube unit cell  $L$ :

$$L = |T| = \frac{3a}{g} \sqrt{n^2 + m^2 + nm}. \quad (1.13)$$

The radius  $R$  of the nanotube follows from the length of the chiral vector (which is equal to the circumference):

$$R = \frac{|\mathbf{C}|}{2\pi} = \frac{\sqrt{3}a}{2\pi} \sqrt{n^2 + m^2 + nm}. \quad (1.14)$$

The surface area of the nanotube is equal to  $|\mathbf{C} \times \mathbf{T}|$ . Dividing this by the area of one hexagon gives us the number of hexagons,  $N$ , in the nanotube unit cell:

$$N = \frac{|\mathbf{C} \times \mathbf{T}|}{|\mathbf{a}_1 \times \mathbf{a}_2|} = \frac{2}{g}(n^2 + m^2 + nm). \quad (1.15)$$

The number of atoms in the unit cell is equal to  $2N$  since there are two carbon atoms per hexagon. To find the coordinates of all the atoms in the unit cell we will make use of the symmetry vector  $\mathbf{R}$ . This is the lattice translation vector in the rectangular graphene sheet starting from the origin,  $O$ , which has the smallest projection on the chiral vector  $\mathbf{C}$ . In the  $\mathbf{a}_{1,2}$  basis we will write it as

$$\mathbf{R} = r_1 \mathbf{a}_1 + r_2 \mathbf{a}_2. \quad (1.16)$$

The restriction of  $\mathbf{R}$  to the rectangle imposes the following constraints:

$$0 < \frac{\mathbf{R} \cdot \mathbf{C}}{|\mathbf{C}|^2} \leq 1 \quad \text{and} \quad 0 < \frac{\mathbf{R} \cdot \mathbf{T}}{|\mathbf{T}|^2} \leq 1. \quad (1.17)$$

When written in terms of  $r_1$  and  $r_2$  the first restriction reads

$$\begin{aligned} 0 < \frac{\mathbf{R} \cdot \mathbf{C}}{|\mathbf{C}|^2} &\leq 1 \\ 0 < \frac{(r_1 \mathbf{a}_1 + r_2 \mathbf{a}_2) \cdot (n \mathbf{a}_1 + m \mathbf{a}_2)}{4\pi^2 R^2} &\leq 1 \\ 0 < \frac{1}{2} \frac{r_1(2n + m) + r_2(2m + n)}{n^2 + m^2 + nm} &\leq 1 \\ 0 < \frac{g}{2} \frac{-r_1 t_2 + r_2 t_1}{n^2 + m^2 + nm} &\leq 1 \\ 0 < r_2 t_1 - r_1 t_2 &\leq N. \end{aligned} \quad (1.18)$$

Since the projection of  $\mathbf{R}$  on  $\mathbf{C}$  must be as small as possible we will require that  $r_2 t_1 - r_1 t_2 = 1$  which can always be achieved since all quantities are integers. The second restriction of equation (1.17) becomes

$$\begin{aligned} 0 < \frac{\mathbf{R} \cdot \mathbf{T}}{|\mathbf{T}|^2} &\leq 1 \\ 0 < \frac{g}{2} \frac{r_1 m - r_2 n}{n^2 + m^2 + nm} &\leq 1 \\ 0 < r_1 m - r_2 n &\leq N. \end{aligned} \quad (1.19)$$

So the two conditions that  $r_1$  and  $r_2$  have to fulfill are

$$r_2 t_1 - r_1 t_2 = 1 \quad \text{and} \quad 0 < r_1 m - r_2 n \leq N, \quad (1.20)$$

since  $t_1$  and  $t_2$  do not have a common divisor greater than 1 these two conditions are enough to uniquely specify  $\mathbf{R}$ . When the sheet is rolled up, the vector  $\mathbf{R}$  will correspond to a rotation of  $\psi$  around the nanotube axis and a translation  $\tau$  along the tube axis. The angle  $\psi$  is equal to  $\frac{2\pi}{N}$  which follows immediately from the fact that  $\mathbf{R}$  is the lattice vector with the smallest projection on  $\mathbf{C}$ . We can also prove this explicitly by

calculating the projection of  $\mathbf{R}$  on  $\mathbf{C}$ :

$$\begin{aligned}
\psi &= \frac{\mathbf{R} \cdot \mathbf{C}}{|\mathbf{C}|^2} 2\pi \\
&= \frac{3a^2 (r_1(n + \frac{m}{2}) + r_2(m + \frac{n}{2}))}{4\pi^2 R^2} 2\pi \\
&= \frac{3a^2 g(-r_1 t_2 + r_2 t_1)}{8\pi^2 R^2} 2\pi \\
&= \frac{g}{2(n^2 + m^2 + nm)} 2\pi \\
&= \frac{2\pi}{N}.
\end{aligned} \tag{1.21}$$

We will denote the symmetry vector by  $\mathbf{R} = (\psi|\tau)$ . The two-dimensional Cartesian coordinates of the atoms in the graphene rectangle can be found from the  $2N$  vectors  $i\mathbf{R}$  ( $A$  sublattice) and  $i\mathbf{R} + \delta$  ( $B$  sublattice) with  $i = 0 \dots N - 1$  where we must only subtract an integer multiple of  $\mathbf{T}$  to make sure the atoms stay inside the rectangle. This integer can be found by calculating the projection on  $\mathbf{T}$ . The coordinates  $\mathbf{r}_{i,A/B}$  of the  $i$ 'th atom in the  $A/B$  sublattice are:

$$\begin{aligned}
\mathbf{r}_{i,A} &= i\mathbf{R} - \left\lfloor \frac{i\mathbf{R} \cdot \mathbf{T}}{|\mathbf{T}|^2} \right\rfloor \mathbf{T}, \\
\mathbf{r}_{i,B} &= i\mathbf{R} + \delta - \left\lfloor \frac{(i\mathbf{R} + \delta) \cdot \mathbf{T}}{|\mathbf{T}|^2} \right\rfloor \mathbf{T},
\end{aligned} \tag{1.22}$$

where again  $i$  runs from 0 to  $N$  and the half brackets indicate the floor function defined by  $\lfloor x \rfloor = \max\{n \in \mathbb{Z} | n \leq x\}$ . The vector  $\delta$  is one of the graphene nearest neighbour vectors which can also be written in terms of an angle  $\psi_B$  around the tube axis and a translation  $\tau_B$  along the tube axis, e.g:  $\delta = (\psi_B|\tau_B)$ . These can be calculated from the Cartesian components of  $\delta$  in the following way:

$$\begin{aligned}
\psi_B &= \frac{\delta \cdot \mathbf{C}}{|\mathbf{C}|^2} 2\pi, \\
\tau_B &= \frac{\delta \cdot \mathbf{T}}{|\mathbf{T}|^2} |\mathbf{T}|.
\end{aligned} \tag{1.23}$$

Now that we have the Cartesian coordinates of the atoms in the sheet we can roll it up along the chiral vector and write down the coordinates in a cylindrical coordinate system  $(r, \phi, z)$  with  $z$  axis parallel to  $\mathbf{T}$  and the origin on the nanotube axis such that the  $z$ -coordinate of  $\mathbf{r}_{0,A}$  is 0. In this coordinate systems the positions of the atoms in the  $A$  sublattice are given by

$$\mathbf{r}_{i,A} = \begin{pmatrix} r_{i,A}^R \\ r_{i,A}^\phi \\ r_{i,A}^z \end{pmatrix} = \begin{pmatrix} R \\ i\psi \\ i\tau - \left\lfloor \frac{i\tau}{|\mathbf{T}|} \right\rfloor |\mathbf{T}| \end{pmatrix}. \tag{1.24}$$

To get the positions of the  $B$  atoms we just need to add  $\psi_B$  to  $\phi$  and  $\tau_B$  to  $z$  and make sure that the resulting position lies inside the nanotube unit cell:

$$\mathbf{r}_{i,B} = \begin{pmatrix} r_{i,B}^R \\ r_{i,B}^\phi \\ r_{i,B}^z \end{pmatrix} = \begin{pmatrix} R \\ i\psi + \psi_B - \left\lfloor \frac{i\psi + \psi_B}{2\pi} \right\rfloor 2\pi \\ i\tau + \tau_B - \left\lfloor \frac{i\tau + \tau_B}{|\mathbf{T}|} \right\rfloor |\mathbf{T}| \end{pmatrix} \tag{1.25}$$

Even though the structure of the unit cell is rather complicated for carbon nanotubes, the underlying crystal lattice is extremely simple. Carbon nanotubes are one-dimensional crystals with just one lattice translation vector,  $\mathbf{a}$ , and one reciprocal lattice vector,  $\mathbf{b}$ , given in Cartesian coordinated by:

$$\mathbf{a} = L \begin{pmatrix} 0 \\ 0 \\ 1 \end{pmatrix}, \quad \mathbf{b} = \frac{2\pi}{L} \begin{pmatrix} 0 \\ 0 \\ 1 \end{pmatrix}. \tag{1.26}$$

Besides the zone center  $\Gamma$  there is one special symmetry point at the edge of the first Brillouin zone called  $X$  which is located at

$$\mathbf{X} = \frac{\pi}{L} \begin{pmatrix} 0 \\ 0 \\ 1 \end{pmatrix}. \quad (1.27)$$

## 1.5 LCBOP II Empirical potential

In general, there are two methods one can use to simulate systems at the atomic level: the quantum methods and the empirical methods. The most rigorous quantum methods, called *ab initio* techniques are aimed at solving the Schrödinger equation and do not require any additional input besides some fundamental constants. The empirical methods, which we will use in this work, are often based on classical chemical concepts and rely on experimental observations as input. The advantage of these empirical methods is that they are generally a lot faster than *ab initio* techniques making them suitable to study large samples containing tens of thousands of atoms.

In this thesis we will describe the interactions between the carbon atoms in our samples by means of an empirical potential energy function. This function allows us to calculate the energy of a system of carbon atoms as a function of their coordinates. The empirical potential we use is called LCBOP II ([10]) which stands for 'Long range Carbon Bond Order Potential'. This potential is capable of giving accurate descriptions of the thermodynamic properties of several phases and allotropes of carbon [5, 11]. Below we will give a short description of main features and ideas of the LCBOP II potential. A more detailed discussion can be found in [12] and [10].

As the name implies, LCBOP II is a so called bond order potential. This family of potentials is based on the idea that the strength of a bond between two atoms is dependent on the environment. Bonds between atoms with few neighbours will be stronger than those between atoms with many neighbours because the electrons available to form bonds have to be shared between less atoms. In the case of carbon, every atom provides four valence electrons. These electrons have to form four bonds in the case of diamond whereas they only have to provide three bonds in the case of graphite. This means that the bonds in graphite will be stronger (have a lower energy) than in diamond, but on the other hand, there will be more bonds in the diamond structure than in graphite. The total cohesive energy will thus be a competition between the strength of the bonds and the number of bonds in the system. For carbon, the result is that the graphitic structure is the most stable (-7.37 eV/Atom for graphite versus -7.35 eV/Atom for diamond [12]).

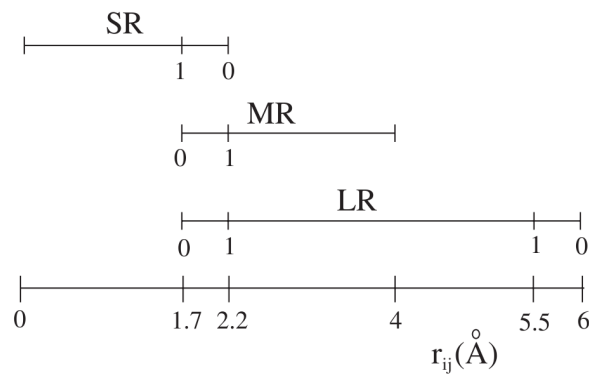


Figure 1.9: Schematic representation of the different interaction domains of the LCBOP II potential. The short-range (SR) interactions are active from 0 to 2.2 Å. The middle-range (MR) interactions contribute from 1.7 to 4.0 Å and the long-range (LR) potential also starts from 1.7 Å and is cut off at 6 Å. The numbers 0 and 1 indicate the domains in which the switch functions are used to cut off the different interaction potentials in a smooth manner.

The functional form of the LCBOPII is built up from three potential energy functions which each have their own domains of bond length in which they give contributions to the cohesive energy. These domains are shown schematically in figure 1.9. The total binding energy  $U$  of a system of  $N$  atoms is given by

$$U = \frac{1}{2} \sum_{ij}^N \left( S_{ij}^{\text{sr}} V_{ij}^{\text{sr}} + (1 - S_{ij}^{\text{sr}}) V_{ij}^{\text{lr}} + \frac{1}{\sqrt{Z_i^{\text{mr}}}} S_{ij}^{\text{mr}} V_{ij}^{\text{mr}} \right), \quad (1.28)$$

where the subscript  $ij$  indicates a dependence on the interatomic distance  $r_{ij} = |\mathbf{r}_i - \mathbf{r}_j|$  between atom  $i$  and atom  $j$ . The function  $V_{ij}^{\text{sr}}$  describes the short-range, covalent bonds. This term contains the bond-order dependence described above. The middle-range potential  $V_{ij}^{\text{mr}}$  represents attractive interactions between atoms at distances just beyond the range of the short-range potential. The prefactor  $Z_i^{\text{mr}}$  includes an environment-dependence in this term as well. The middle-range interactions play an important role in situations where bonds are broken or created but are unimportant in the 'chemically static' situations we are considering in this thesis<sup>1</sup>. For this reason, and also because the implementation of this term in the simulation routines was not completely finished in the updated version of the code used here, we have not included this term in our calculations.

Finally there is the function  $V_{ij}^{\text{lr}}$  which represents the long-range, non-bonded interactions which include the van der Waals forces between the layers in graphite. The  $S$  functions are switch functions which smoothly cut-off or turn on the interactions in specified range intervals thereby limiting the effect of the three potential functions to the ranges shown in figure 1.9.

---

<sup>1</sup>Defects in graphene are observed for temperatures higher than 3500 K, much higher than the temperatures we will consider in this work.

# Atomistic simulations

Atomistic simulations are designed to model materials at the atomic level. In this type of simulation, interactions between atoms are often described by empirical potential energy functions, like the LCBOPII potential used in this thesis. The use of empirical potentials makes these simulations relatively fast, compared to other techniques such as *ab initio* simulations. This means that they can be used to efficiently study large systems containing thousands of atoms.

In this chapter we will use atomistic simulations to model the structure of carbon nanotubes at finite temperatures. Our main objective is to determine the coefficient of thermal expansion (CTE) in the radial and axial directions which we will denote by  $\alpha_r$  and  $\alpha_l$  respectively. They are defined as follows:

$$\alpha_r = \frac{1}{R} \frac{dR}{dT}, \quad \alpha_l = \frac{1}{L} \frac{dL}{dT}. \quad (2.1)$$

Here,  $R$  is the radius of the nanotube and  $L$  is its length. Our interest in these coefficients arises because there is still discussion on this subject, in the scientific literature. For graphene the CTE is predicted to be negative at low temperatures [13, 14, 15], which was recently confirmed by experiments [16]. For nanotubes however, the results on the CTE vary such a lot that no unique conclusion can be drawn. Some studies state that the CTE is positive in the whole temperature range [15, 17, 18] while others argue that it is negative at low temperature (usually this means  $T \lesssim 400$  K) and becomes positive at higher temperatures [19, 20, 21]. Even if the works agree on this point, there are still large differences in the actual values of the reported CTEs.

In any case, most studies agree that the low temperature behaviour of the CTE should be largely determined by low energy vibrational modes while at higher temperatures anharmonic bond length expansion starts playing a larger role [17, 19, 21, 22]. Atomistic simulation techniques, combined with the high accuracy of the LCBOPII potential, provide a good tool to study finite temperature effects such as the CTE of large systems like carbon nanotubes. The reason for this is that all anharmonic effects are included in these simulations and that we can simulate large scale samples to allow for low energetic, long-wavelength, vibrational excitations.

We continue with a short description of the two simulation techniques we will use, namely Monte Carlo and Molecular Dynamics. For a much more in-depth discussion of Monte Carlo and Molecular Dynamics techniques, we refer the reader to [23].

## Monte Carlo

In Monte Carlo simulations, physical quantities are calculated as statistical averages over a large number of configurations of the system. These configurations are generated in such a way that configurations with large Boltzmann factors,  $\exp(-E/k_B T)$ , are more likely to be generated than configurations with negligible Boltzmann factors. This is a useful criterion since we know from statistical mechanics that configurations with small Boltzmann factors will barely contribute to the thermal averages of physical quantities. The most common way to generate these configurations is by using the Metropolis algorithm [24]. If the system is in a certain state, say state  $o$ , a new state is generated by displacing a random particle in a random direction. This gives a new state, called  $n$ . The energy difference between  $o$  and  $n$  is evaluated and the state  $n$  is accepted as the new state of the system with probability

$$P(o \rightarrow n) = \min \left[ 1, \exp \left( -\frac{E(n) - E(o)}{k_B T} \right) \right]. \quad (2.2)$$

This method has proven to be very efficient at probing the configuration space of the system. The natural ensemble of a system in Monte Carlo simulations is the canonical, or  $NVT$ , ensemble which has a fixed number of particles  $N$ , a fixed volume  $V$  and a fixed temperature  $T$ . This ensemble however, is not the most suitable for our purposes. Since we are interested in the thermal expansion of systems, we need to allow the system to change its volume. This can be done by using the isobaric-isothermal, or  $NpT$ , ensemble. As the name implies, this ensemble has a fixed number of particles, a fixed pressure  $p$ , and a fixed temperature.

Monte Carlo simulations in the  $NpT$  ensemble require the introduction of an additional way (or Monte Carlo move) to generate system states. This move changes the volume of the system by a random amount from  $V$  to  $V'$  and scales all atom coordinates by the appropriate factor. We will call this kind of move a volume fluctuation. The probability that a volume fluctuation will be accepted is equal to

$$P(V \rightarrow V') = \min \left[ 1, \exp \left( -\frac{E(V') - E(V) + p(V' - V)}{k_B T} + N \ln \frac{V'}{V} \right) \right]. \quad (2.3)$$

In addition to the fact that this ensemble can be used to determine the average volume of a system at some temperature it is also more resemblant of experimental conditions which are usually also carried out at constant pressure rather than at constant volume.

### Molecular Dynamics

Molecular Dynamics is a technique based on the assumption that the nuclear motion of a system is described by the laws of classical mechanics. This assumption might seem unjustified at first because quantum effects should have a significant influence on systems of atomic scale. It turns out however, that only for the lightest atoms and molecules (He, H<sub>2</sub>, D<sub>2</sub>) the the Broglie wavelengths become comparable to typical distances in the systems. This justifies the use of the classical approximation for heavier elements such as carbon. Also, the nuclei of the atoms however are so much heavier than the surrounding electrons that the timescales at which the nuclei move are also much lower than those of the electrons. This means that the electronic states of the system will change almost instantaneously with the positions of the nuclei. The potential which describes the interactions between the atoms is of course based on experiments and *ab initio* calculations, which include quantum effects. In this way it is possible to describe the motion of the nuclei by classical means with a potential energy function which is derived from quantum mechanical calculations.

A Molecular Dynamics simulation starts from a configuration of atoms with initial positions and initial velocities. One then calculates the forces on the atoms based on the potential energy function. Finally Newton's equation of motion are integrated to find the trajectory of each atom as a function of time.

The temperature of the system is found from the theorem of the equipartition of energy. The average kinetic energy per degree of freedom is equal to  $\frac{1}{2}k_B T$ . The instantaneous temperature of a system with  $N$  particles and  $D$  degrees of freedom (usually  $D = 3N - 3$  for a three dimensional system with fixed momentum) can hereby be defined as

$$T(t) = \sum_{i=1}^N \frac{m_i v_i^2(t)}{k_B D}, \quad (2.4)$$

where  $m_i$  is the mass, and  $v_i$  the velocity of the  $i$ 'th particle.

The advantage which Molecular Dynamics has that it is truly dynamic. It allows to determine the real timescales of physical effects and to dynamically study the response of the system to perturbations. At the downside, Molecular Dynamics is usually quite a bit slower than Monte Carlo in determining physical quantities because the calculation of the forces and the integration of the equation of motion is computationally quite expensive.

## 2.1 Monte Carlo simulations

We have performed atomistic Monte Carlo simulations based on the LCBOP-II potential to calculate physical properties describing the structure of carbon nanotubes as a function of temperature. The simulations are performed with periodic boundary conditions in the  $z$ -direction (along the tube axis) in the  $NpT$  ensemble at zero pressure. This means that we allow for volume fluctuations in the  $z$ -dimension of the simulation box. In the  $x$  and  $y$  directions we added a sufficient amount of empty space to allow the nanotube to move and expand freely. We start with a perfect nanotube configuration described by equations (1.24) and (1.25) with  $a_{CC} = 1.42 \text{ \AA}$  at  $T = 10 \text{ K}$  or  $T = 50 \text{ K}$  and slowly heat the system in  $2 \times 10^4$  MC steps<sup>1</sup> to the desired temperature. Then we leave the system at that temperature for a further  $5 \times 10^4$  steps and save 101 equally spaced configurations, from the second half of these steps, to evaluate average physical data. From this final configuration the system is then again heated to the next temperature in  $2 \times 10^4$  steps.

Simulations are performed on a selection of different nanotubes, both chiral and achiral, which cover a range in radius from about 8 to 19  $\text{\AA}$ . Since some types of nanotubes have very small unit cells, especially the armchair and zigzag types, we have stacked several unit cells to perform simulations. This is necessary for two reasons. The first is that the simulation box must be larger than the cutoff radius of the potential (6  $\text{\AA}$  for LCBOP-II) in order to apply periodic boundary conditions. The second reason is that a larger sample allows for larger (longer wavelength) fluctuations. To represent this so-called supercell, we introduce a new notation,  $(n, m, c)$ , to specify a certain nanotube sample. The  $n$  and  $m$  indices are the usual nanotube indices and  $c$  is an extra integer indicating how many units cells have been stacked on top of each other. For the case of just one unit cell we will skip the index  $c$ , so  $(n, m, 1) \equiv (n, m)$ . The types of nanotubes used in the simulations are listed in table 2.1.

Table 2.1: List of nanotube types and their basic dimension used in simulations.

C	Type	# Atoms	Length ( $\text{\AA}$ )	Radius ( $\text{\AA}$ )
(14,10)	Chiral	872	44.48	8.17
(16,8,10)	Chiral	2240	112.71	8.29
(25,9)	Chiral	3724	129.98	11.94
(20,20,30)	Armchair	2400	73.79	13.56
(39,0,10)	Zigzag	1560	42.60	15.27
(29,26)	Chiral	3028	67.67	18.65

### Structural analysis

Our first interest, once the simulations are finished, is the behaviour of the nanotube radius and length with temperature. The length is easily determined from the size of the simulation box in the  $z$ -direction. To obtain the radius of a given nanotube configuration we calculate the average distance of the atoms in the nanotube to the axis of the tube. The axis of a nanotube however is not expected to remain fixed during the heating process. Rather, we expect it to show translational movement and, more importantly, to vary with height,  $z$ , in the nanotube. To correct for these variations of the nanotube axis we calculate the radius of a given configuration with respect to a  $z$ -dependent axis. This axis,  $A(z)$ , is calculated as a weighted average of the  $x$  and  $y$  coordinates of the  $2N$  atoms in the nanotube:

$$A^j(z) = \frac{\sum_{i=1}^{2N} w(|z - r_i^z|) r_i^j}{\sum_{i=1}^{2N} w(|z - r_i^z|)}, \quad (j = x, y), \quad (2.5)$$

where  $r_i^j$  denotes the  $j$ 'th Cartesian coordinate of the  $i$ 'th atom and  $w(|z|)$  is the weight function defined by

$$w(|z|) = \frac{1}{e^{3(|z|-2)} + 1}, \quad (2.6)$$

<sup>1</sup>1 MC step corresponds to  $N$  attempted moves

which ensures that only atoms within a range of about  $z \pm 2 \text{ \AA}$  are weighted in. Of course, the calculated  $A(z)$  also provides information about the bending of the nanotube.

Length and radius are quantities which apply to the nanotube as a whole. To learn more about the structure of the nanotubes we also look on a smaller scale. To this end we divide the nanotube into a number of disks of height  $\Delta z$ , and divide every disk into  $n$  slices of angle  $\Delta\phi = \frac{2\pi}{n}$  as illustrated in figure 2.1. The average distance of the atoms from the axis in each slice separately gives information about deviations from the cylindrical structure and about possible ripples on the nanotube surface.

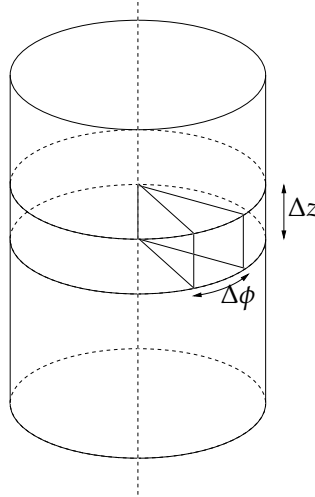


Figure 2.1: Nanotube sample with a disk of height  $\Delta z$  and a slice of angle  $\Delta\phi$ .

Finally we will also calculate the radial distribution function,  $g(r)$ . This function gives the probability to find an atom at a distance  $r$  from any given atom. It is defined as

$$g(r) = \frac{\rho(r)}{\rho}, \quad (2.7)$$

where  $\rho$  is the average density and  $\rho(r)$  is the average local density at distance  $r$  from an atom. At zero temperature  $g(r)$  will consist of sharp, delta-like peaks at the equilibrium neighbour distances (approximately  $1.42 \text{ \AA}$  for first nearest neighbours and  $2.46 \text{ \AA}$  for second nearest neighbours in graphitic systems). At higher temperatures the peaks will broaden due to the increasing motion of the atoms and the position and shape of the peaks can also change due to anharmonicities in the potential or, for example, due to a phase transition.

## 2.1.1 Results and discussion

### Radial structure

Our results for the average nanotube radius as a function of temperature are shown in figure 2.2. We have plotted the computed radius as a fraction of the theoretical radius,  $R_0$ , given by equation (1.14). The radius at  $T = 0$  is calculated directly from the initial sample and is of course equal to the theoretical value. It appears that the average tube radius varies very little with temperature compared to the fluctuations in radius which are represented through the errorbars. The overall behaviour though, shows a small increase in radius with increasing temperature for all simulated nanotubes. This increase reaches about 0.5% at 1300 K for the smallest tubes.

An interesting feature is the jump in radius at the first simulated temperature, which suggests that the initial configuration is not the most energetically favorable. This jump shows the best for three tubes which we have simulated well below room temperature, and is the largest for the smallest diameter tubes.

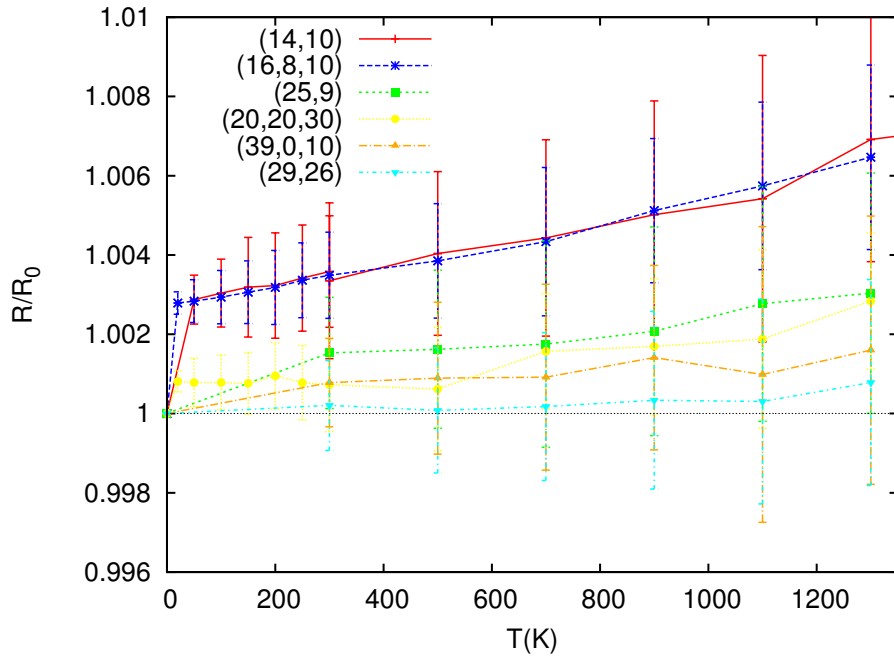


Figure 2.2: Fractional radius as a function of temperature for several nanotubes. The nanotubes are listed in order of increasing zero temperature, theoretical radius  $R_0$ . The zero temperature value is from the unrelaxed initial sample which explains the apparent discontinuity at  $T = 0$  K.

The larger the theoretical radius of the nanotube, the smaller the jump. There are at least two reasons for this jump, both of which have to do with the curvature of the nanotube. The first is that we construct our nanotube unit cell from a perfect graphene sheet, in which all distances are equal to  $1.42 \text{ \AA}$ . This sheet is then rolled up to form a cylinder in such a way that all atoms are at a distance  $R_0$  from the axis of the tube. This rolling up process however reduces the distance between the carbon atoms due to the curvature of the cylinder. The second reason is that the angles between the nearest neighbour bonds are also reduced due to the rolling up of the graphene sheet, and are thus smaller than  $120^\circ$ . For such configurations the equilibrium nearest neighbour distance is larger than  $1.42 \text{ \AA}$ . Both of these effects will make the nanotube expand slightly, thereby increasing the radial bond length and lowering the energy of the sample.

A peek at the atomic configurations confirms the finding that there is no big increase in nanotube radius with temperature. Figure 2.3 shows a typical cross-section of the configuration of the (29,26) nanotube. The two cross-sections are taken at respectively  $T = 0$  K (initial sample) and  $T = 1300$  K.

From this cross-section it seems that the surface is not smooth but rather rippled. To investigate these ripples further we divide every nanotube configuration into disks and slices as show in figure 2.1. The height  $\Delta z$  of the disks is set at about  $3 \text{ \AA}$  and the number of slices into which we divide every disk ranges from 8 to 12 depending on the radius of the nanotube. To get an impression of the height of the ripples we calculate the average distance to the axis of the atoms in each slice separately (typically a slice contains about 8 to 10 atoms). This gives us a  $\phi$ -dependent radius. Then we calculate, per disk, the difference in radius between the slice with the biggest radius,  $R_{max}$ , and the slice with the smallest radius,  $R_{min}$ . This is denoted by  $\Delta R$ .

$$\Delta R = R_{max} - R_{min} \quad (2.8)$$

The temperature dependence of the average  $\Delta R$  is shown in figure 2.4 for all

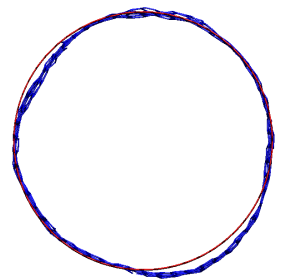


Figure 2.3: Typical cross section of (29,26) nanotube at  $T = 1300$  K. Initial sample cross section is shown in red.

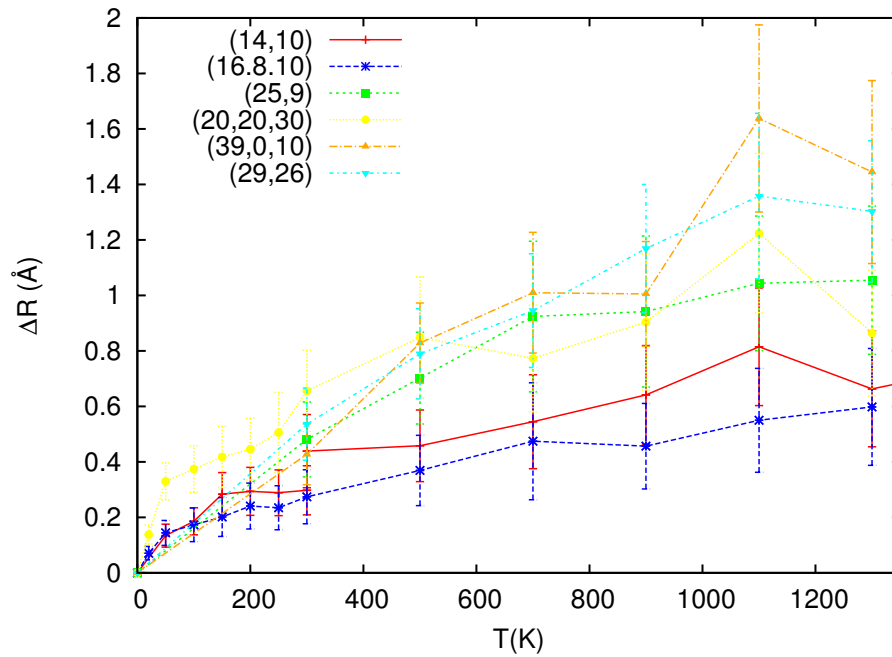


Figure 2.4: Average difference in radius between 'biggest' and 'smallest' slice in a disk of height  $\Delta z \approx 3 \text{ \AA}$  for different nanotubes.

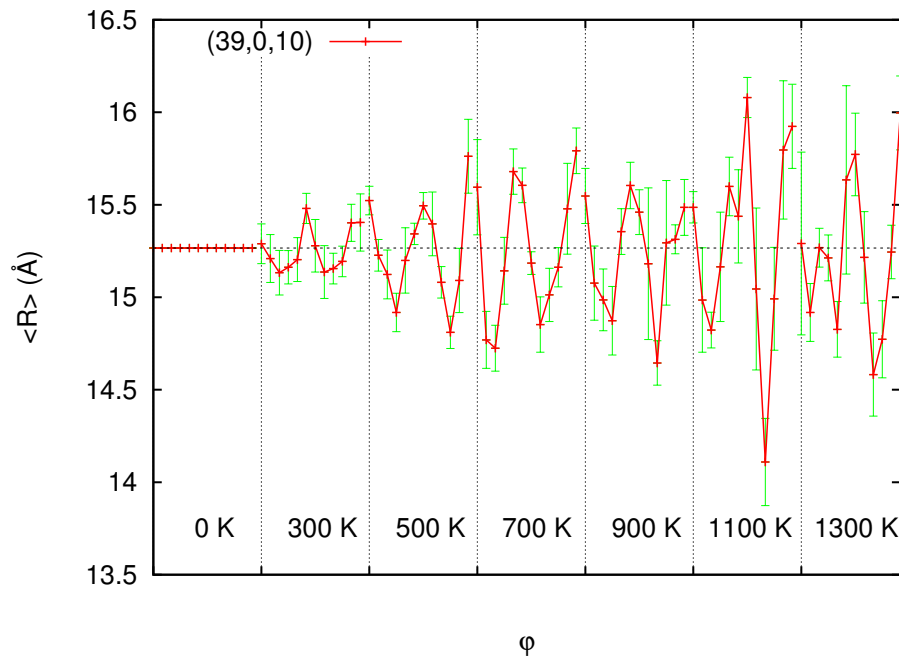


Figure 2.5: Average radius as a function of  $\phi$  and  $T$  in a disk of height  $\Delta z = 2.84 \text{ \AA}$  at  $z = 11.36 \text{ \AA}$ .

simulated nanotubes. This figure shows that, as expected, the height of the ripples grows with temperature. It is also clear that the largest diameter tubes show the biggest  $\Delta R$ . As an example of a typical configuration, the average radius per slice (as a function of  $\phi$ ) in a disk of the (39,0,10) nanotube is shown in figure 2.5. It is clearly visible that the fluctuations in radius increase with temperature. On average there appear to be about two maxima and minima per circumference of the nanotube.

From the obtained radius as a function of temperature we calculate the radial coefficient of thermal expansion,  $\alpha_r$ , by making a fit to the data from figure 2.2 based on the exponential solution to equation (2.1). In general, the CTE is temperature dependent, but given the size of the errorbars on the data, we will not be able to determine this temperature dependence. The value of  $\alpha_r$  will thus be an average value over the temperature range from 300 to 1300 K (50 to 1300 K for the three nanotubes which we have simulated at lower temperatures). The resulting CTEs are listed in table 2.2. As we already knew from figure 2.2, all coefficients are positive. A general behaviour is the decrease of  $\alpha_r$  with increasing nanotube radius. This is probably due to the higher curvature in the smaller diameter nanotubes.

Table 2.2: Radial, axial and bond length coefficients of thermal expansion. Values were obtained by making a fit to the simulations data from figures 2.2, 2.6 and 2.9.

Nanotube	Radius (Å)	Radial CTE $\alpha_r$ ( $10^{-6} \text{ K}^{-1}$ )	Axial CTE $\alpha_l$ ( $10^{-6} \text{ K}^{-1}$ )	bond length CTE $\alpha_b$ ( $10^{-6} \text{ K}^{-1}$ )
(14,10)	8.17	(2.83 ± 0.17)	(2.71 ± 0.07)	(4.40 ± 0.03)
(16,8,10)	8.29	(2.80 ± 0.08)	(2.67 ± 0.07)	(4.48 ± 0.01)
(25,9)	11.94	(1.60 ± 0.25)	(2.32 ± 0.18)	(4.44 ± 0.04)
(20,20,30)	13.56	(1.41 ± 0.20)	(1.91 ± 0.11)	(4.45 ± 0.03)
(39,0,10)	15.27	(0.695 ± 0.266)	(2.24 ± 0.33)	(4.36 ± 0.11)
(29,26)	18.65	(0.532 ± 0.197)	(1.96 ± 0.25)	(4.38 ± 0.09)

### Axial structure

The length of the nanotubes as a function of temperature is calculated as the average dimension of the simulation box in the  $z$ -direction. The results are shown in figure 2.6. As we saw with the results on the radius, there is a jump at  $T = 0$  K because the initial sample is not the minimal energy configuration. All nanotubes show an increase in length with temperature so the axial coefficients of the thermal expansion will also be positive. From this data we calculated an average  $\alpha_l$  for each nanotube. These values are listed in the fourth column of table 2.2. From this data we can see no clear dependence of  $\alpha_l$  on the radius of the nanotube. The differences in  $\alpha_l$  might be due to the different chiralities of the nanotubes but the errors on the data are too large to draw conclusions from this.

### Local structure

The radial distribution function,  $g(r)$ , provides us with information about the bond lengths between the carbon atoms. As an example  $g(r)$  is shown in figure 2.7 for the (16,8,10) nanotube between  $r = 1.2$  Å and  $r = 3.0$  Å at different temperatures. The peaks at the first, second and third nearest neighbour distances are clearly visible. The peaks broaden with increasing temperature due to the increased motion of the atoms. The jump at  $T = 0$  from figures 2.2 and 2.6 can be found back when comparing the radial distribution functions around nearest neighbour distance of the initial sample and a configuration at low temperatures. This is shown in figure 2.8 for the (16,8,10) nanotube. Three different bond lengths, all lower than 1.42 Å, occur in the initial sample as indicated by the blue vertical lines. The average radial distribution function at  $T = 20$  K has its peak well to the right of the three initial bond lengths indicating an increase in average bond length. This increase in bond length in turn causes the sudden increase in radius.

In the harmonic approximation the nearest neighbour peak in  $g(r)$ , which we will denote by  $g(R_{nn})$  from now on, should be a Gaussian distribution. To investigate the nearest neighbour bond length we fitted Gaussians to the radial distribution functions. The peaks of the fitted distributions,  $R_{nn}(T)$ , are shown in figure 2.9. As a function of temperature the average bond length increases linearly. The different curvatures of the nanotubes are responsible for the slight differences in bond lengths. From this data we calculate the coefficient of thermal expansion of the nearest neighbour bond length,  $a_{CC}$ . This CTE, named  $\alpha_b$ , is defined as

$$\alpha_b = \frac{1}{a_{CC}} \frac{da_{CC}}{dT}. \quad (2.9)$$

The values for  $\alpha_b$ , for the different nanotubes are also listed in table 2.2. The coefficient has a value of  $4.4 \times 10^{-6} \text{ K}^{-1}$  with no significant dependence on the radius or chirality of the nanotube. This is no surprise as the bond length is a purely local property with its temperature dependence determined by the anharmonicity of the potential.

More interesting is the fact that the axial,  $\alpha_l$ , and radial,  $\alpha_r$ , CTEs are smaller than  $\alpha_b$  for all studied nanotubes. This leads to the conclusion that the thermal expansion of carbon nanotubes is not just governed by the increase in bond length. After all, the unit cell length and the nanotube radius are both linear functions of the carbon-carbon distance (see equations (1.13) and (1.14)). There must be other effects which lead to thermal contraction. It is suggested that long-wavelength bending vibrations, as well as elliptical deformations of the nanotube cross-section, lead to an effective contraction of the nanotube length and radius [15, 19]. The overall CTE will be the result of a competition between these vibrational modes and the anharmonicity related expansion of the bond lengths.

### Comparison with other studies

Our Monte Carlo simulations have thus far shown positive coefficients of thermal expansion in both the axial and radial directions for all studied nanotubes over the whole temperature range. Numerous other scientific studies have been done on this subject with a wide variety of results. Below is an overview of these other studies. Because there are rather many studies, and most of them involve several different nanotubes, we will only qualitatively discuss their results. The actual values of the CTEs differ per study of course, but generally they are within the range of  $-1 \times 10^{-5} \text{ K}^{-1}$  to  $1 \times 10^{-5} \text{ K}^{-1}$ .

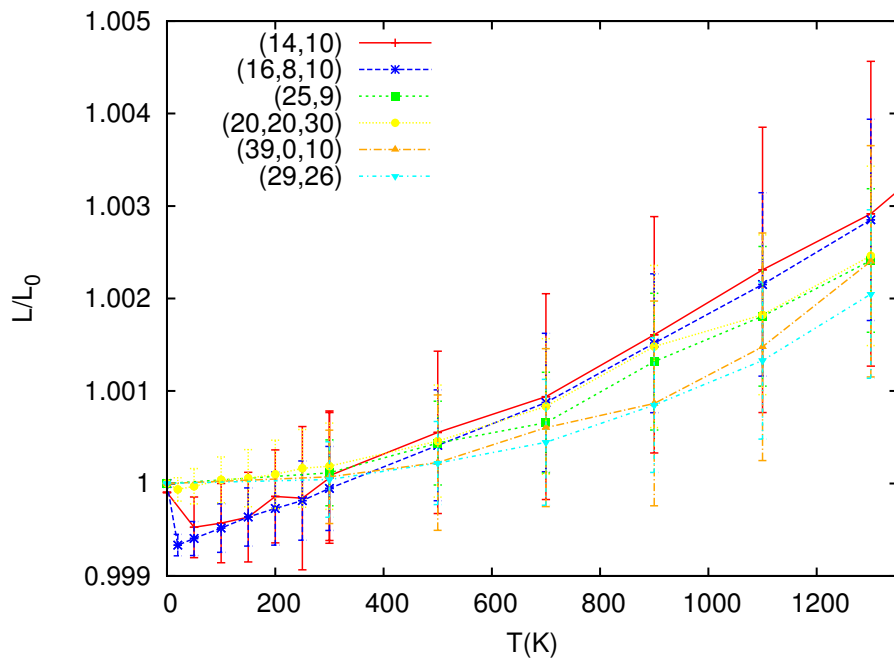


Figure 2.6: Fractional length of the simulated carbon nanotubes as a function of temperature. Nanotubes are listed in the order of increasing radius  $R_0$ . The zero temperature value is from the unrelaxed initial sample which explains the apparent discontinuity at  $T = 0$  K.

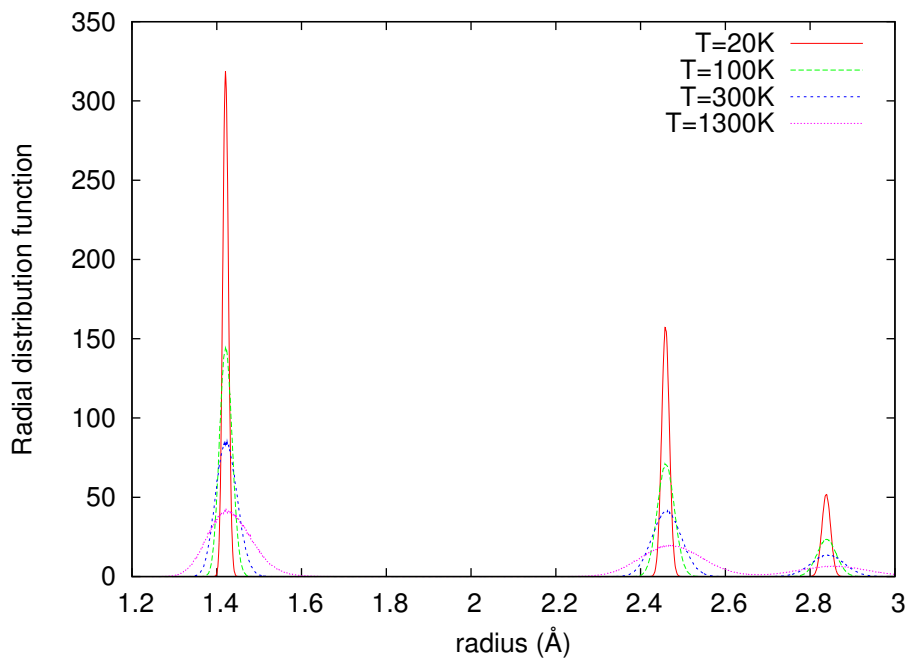


Figure 2.7: Radial distribution function for different temperatures for (16, 8, 10) nanotube

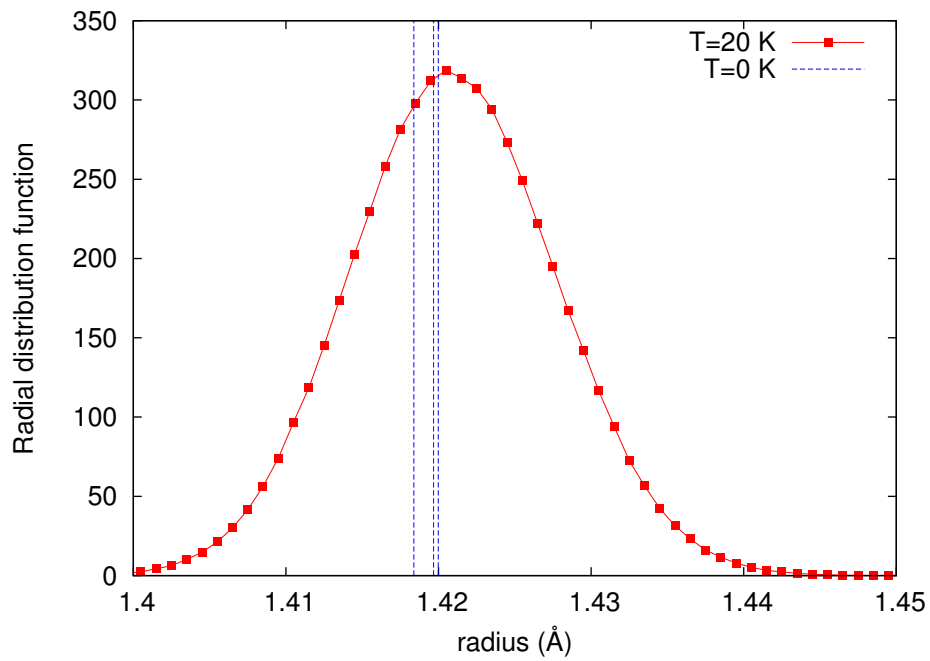


Figure 2.8: Nearest neighbour peak of  $g(r)$  for the (16, 8, 10) tube at  $T = 20$  K, and for the initial, unequilibrated sample.

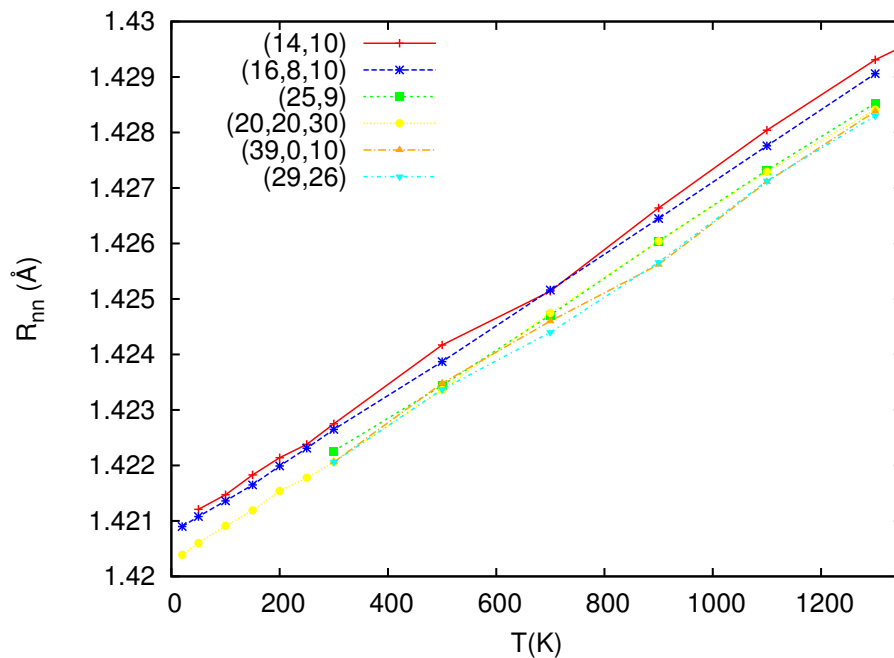


Figure 2.9: Temperature dependence of the nearest neighbour distance,  $a_{CC}$ , for different nanotubes. Data is obtained from the nearest neighbour peaks of the radial distribution functions.

Several studies report the same trend in the CTEs as we have found. Among these are Molecular Dynamics studies by Ravivikar et al. [17] and Schelling and Koblinski [15] based on the Tersoff bond-order potential [25]. Li et al. [18] also report positive CTEs over the whole studied temperature range (0 to 2000 K) based on molecular structural mechanics. Then, there are several papers which report a negative CTE at low temperatures which becomes positive at higher temperatures. These include two theoretical studies based on the Brenner empirical bond-order potential [26] by J. Jiang et al. [21] and H. Jiang et al. [20]. The first study, which uses the nonequilibrium Green's function method, finds negative CTEs up to about 500 K followed by expansion at higher temperatures in both the radial and axial directions. The second study, which takes a more geometrical approach, finds a positive CTE in the axial direction for all temperatures. Molecular Dynamics simulations by Kwon et al. [19] also lead to this negative-positive trend in the CTEs in both directions. Finally there is an elaborate Molecular Dynamics study by Cao et al. [22] which reports negative CTEs over the whole temperature range (0 to 800K).

Experimentally, the CTE of single walled carbon nanotubes is extremely difficult to measure. In the first place, this is because it is hard to isolate a single nanotube and perform experiments on it. There is one experimental result available from X-ray diffraction studies of carbon nanotube bundles by Maniwa et al. [27]. They report a radial CTE of  $(-1.5 \pm 2.0) \times 10^{-6} \text{ K}^{-1}$  and an axial CTE of  $(0 \pm 1) \times 10^{-6} \text{ K}^{-1}$ . Apart from the large errors on the measurements it is unclear how this result relates to isolated nanotubes.

Regardless of the results, all studies agree that low energy vibrations play an important role at low temperatures. These modes contribute to negative CTEs. Especially the transverse acoustic (TA) bending mode, which causes bending deformations in the  $x$ - and  $y$ -directions, has a large contribution because its energy has a quadratic dependence on the wavevector rather than usual linear dependence. Schelling and Koblinski [15] demonstrated this in a convincing manner by using the theory of lattice dynamics which we will employ later in chapter 3. The longer the wavelength of the vibrations, the larger their contribution to negative CTEs.

This means of course, that rather long nanotube samples are needed in simulations to allow for the long-wavelength modes. It must be noted that the Molecular Dynamics studies we have cited above all used free boundary conditions whereas our Monte Carlo studies have been done with periodic boundary conditions along the nanotube axis, albeit with volume fluctuations in the  $NpT$  ensemble. These free boundary conditions leave the ends of the nanotube more free to move than periodic boundary conditions do. This could make the bending of the nanotube easier resulting in lower CTEs due to the increased amplitude of the bending modes. We believe however, that, in order to properly determine the coefficients of thermal expansion one should use periodic boundary conditions in order to mimic the huge length to radius ratio of true carbon nanotubes<sup>2</sup>.

## 2.1.2 Wave Move Monte Carlo simulations

The axial and radial CTEs from our Monte Carlo simulations are all positive but smaller than the expansion coefficient of the bond lengths themselves. This means that vibrational modes do have an influence on the CTEs, but that the effect of anharmonic bond length expansion is larger.

The question remains whether or not our samples were large enough to allow for long-wavelength vibrations and if Monte Carlo is a suitable technique to simulate these modes. The negative coefficient of thermal expansion of graphene however, has been obtained by means of Monte Carlo simulation (with periodic boundary conditions) with the LCBOPII potential by Zakharchenko et al. [13]. Since a graphene sheet with periodic boundary conditions is basically a carbon nanotube of infinite radius, it seems reasonable that we should be able to observe negative CTEs if they do in fact exist in nanotubes. It must be noted though, that this Monte Carlo study was not solely based on the random displacement of one randomly picked atom at a time, but included a special move called a wave move [29]. These moves more or less artificially introduce long-wavelength vibrations (which also in graphene play a crucial role in the thermal contraction). This was necessary because ordinary Monte Carlo sampling proved inefficient at probing the long-wavelength excitations. Based on the above, it could be that our results are not reliable because simple MC sampling is not sufficient to account for the effects of long-wavelength phonons and because our nanotube samples might not be long enough.

<sup>2</sup>Nanotubes have been observed with length-to-diameter ratios of up to 132,000,000:1 [28].

To determine the temperature dependence of length and radius of the nanotubes more accurately we will introduce wave moves in our Monte Carlo routine. These moves consist of wavelike displacements corresponding to the transverse acoustical (TA) phonon mode. There are two degenerate TA modes, one corresponds to bending in the  $x$ -direction and the other to bending in the  $y$ -direction. The wavevectors  $\mathbf{q}$  only have a component in the  $z$ -direction and are restricted by the periodic boundary conditions over the length  $L$  of the nanotube sample

$$\mathbf{q} = n \frac{2\pi}{L} \hat{z}, \quad n = 1, 2, 3, 4. \quad (2.10)$$

The upper bound on  $n$  is 4, to restrict the wavemoves to long wavelengths, since we assume that short wavelength vibrations are already well described by the traditional MC sampling. Given a wavevector, the Cartesian displacement of atom  $i$  at position  $\Delta \mathbf{r}_i$  is calculated as follows:

$$\Delta \mathbf{r}_i = p A_q \begin{pmatrix} \cos \psi & -\sin \psi & 0 \\ \sin \psi & \cos \psi & 0 \\ 0 & 0 & 1 \end{pmatrix} \begin{pmatrix} \sin(\mathbf{q} \cdot \mathbf{r}_i + \phi) \\ 0 \\ 0 \end{pmatrix}, \quad \text{with} \quad \begin{array}{l} -1 \leq p \leq 1 \\ 0 \leq \psi \leq \frac{\pi}{2} \\ 0 \leq \phi \leq \frac{\pi}{2} \end{array}$$

where the number  $p$ ,  $\phi$  and  $\psi$  are randomly chosen. The maximum amplitude of the wave,  $A_q$ , depends on the wavevector and possibly also on the dimensions of the nanotube, the amplitude is multiplied by a random,  $p$  number between  $-1$  and  $1$ . The phase angle  $\phi$  ensures we also include the  $\cos(\mathbf{q} \cdot \mathbf{r}_i)$  wave and any phase in between. Finally there is a rotation over an angle  $\psi$  in the  $x, y$ -plane which ensures we have both the  $x$ - and  $y$ -directed bending mode vibrations, and any direction in between.

The amplitude of the wavemoves is scaled while the simulation is running to obtain an acceptance ratio between 0.4 and 0.5. The same criterion is used to determine the amplitude of the volume fluctuations. A wavemove or a volume fluctuation, decided randomly between the two, is attempted every MC step.

## Results and discussion

We performed Monte Carlo simulations with the wavemove routines on (10,10) nanotubes because these are often used in other studies. Their small radius of 6.78 Å also allows for long samples without the number of atoms becoming too extreme, thus keeping simulation time within reasonable limits. The two samples we have used have 220, and 440 unit cells stacked on top of each other yielding supercell lengths of 541 and 1082 Å respectively (see table 2.3 for details). These long lengths mean that long-wavelength modes can clearly manifest themselves in the system. Our longest sample is over a factor 4 longer than the 244 Å long, (5,5) sample studied by Cao et. al [22], who report thermal contraction due to the TA modes. Schelling and Koblinski [15] report that the effect of the TA modes should start to dominate the axial CTE for (10,10) nanotubes of more than 200 unit cells long. We thus believe that our samples are sufficiently long to study the effects of the wavemoves.

Table 2.3: Basic dimensions of the nanotubes used in Monte Carlo simulations with wavemoves.

C	Type	# Atoms	Length (Å)	Radius (Å)
(10,10,220)	Armchair	8800	541.01	6.78
(10,10,440)	Armchair	17600	1082.19	6.78

The large number of atoms, 8800 and 17600 for the shorter and longer sample respectively yield large simulation times. One simulation run, at a single temperature, takes about two weeks for the largest sample on a 2.4 GHz AMD Opteron processor. It is therefore very time consuming to simulate both samples at all the temperatures we used in the previous section. We have decided to perform simulations at 50 and 400 K. We used  $5 \times 10^4$  MC steps for equilibration and another  $5 \times 10^4$  step for averaging of physical data. Most other studies reporting negative CTEs, find that the thermal contraction has its minimum around 400 K. Therefore, if thermal contraction appears, there should be a significant length difference between these two temperatures.

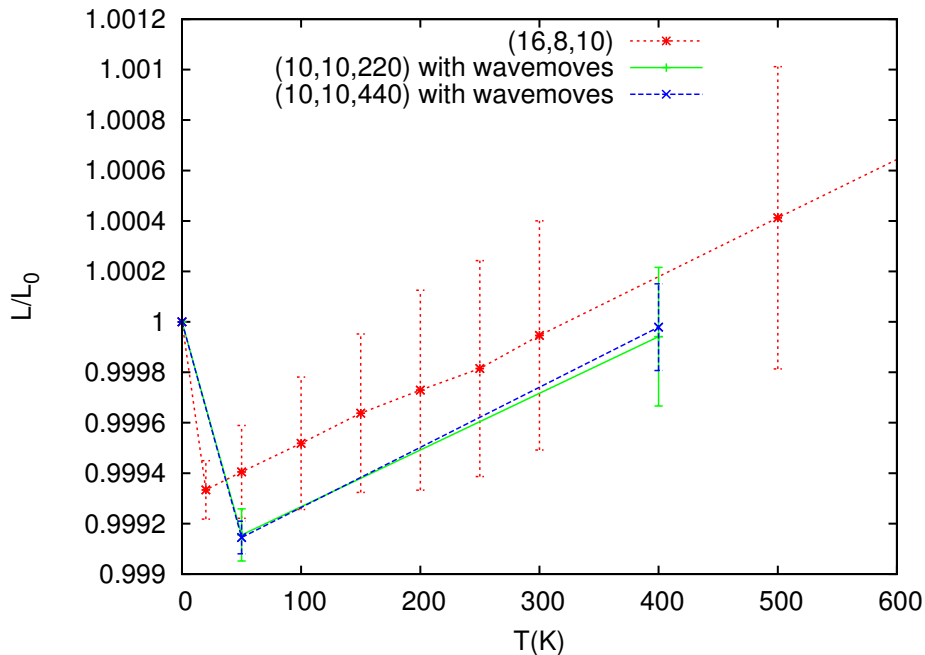


Figure 2.10: Length of the nanotubes as a fraction of their initial, unrelaxed length,  $L_0$ , as a function of temperature. The two (10,10) nanotubes are simulated with wavemoves while the data for (16,8,10) is the same as in figure 2.6.

The average length at the two simulated temperatures is shown in figure 2.10. The data for the (16,8,10) nanotube from figure 2.6, taken without the wavemoves in the Monte Carlo routine, is also shown for comparison. Clearly, there is no sign of thermal contraction from these data, the initial decrease is an effect of the unequilibrated initial sample as explained in the previous section. The values of  $\alpha_l$  are  $2.24 \times 10^{-6} \text{ K}^{-1}$  and  $2.38 \times 10^{-6} \text{ K}^{-1}$  for the (10,10,220) and the (10,10,440) nanotube respectively. In the radial direction, we have also not seen any signs of thermal contraction.

Comparing the values of  $\alpha_l$  to the results in table 2.2 we can conclude that the inclusion of wavemoves in the Monte Carlo routine has had a negligible effect. When we compare this to the amplitude of the vibrations that are applied in the simulation, this is not so surprising. At 400 K, the amplitude of the longest wave ( $n = 1$  in equation (2.10)) is only 0.3 Å. This is very small compared to the amplitudes of 3 Å found by Cao et. al [22] from their Molecular Dynamics simulation, which even used shorter samples.

## 2.2 Molecular Dynamics simulations

The Monte Carlo simulations performed thus far have not shown signs of negative coefficients of thermal expansion in the studied nanotubes. Atomistic simulations which have shown negative CTEs however, have been done by Molecular Dynamics (MD). Even though MD simulations are generally slower than Monte Carlo (MC) simulations, one can argue that MD simulations are intrinsically somewhat better suited to study these systems. The main argument is that the thermal contraction is believed to arise from lattice vibrations which are clearly dynamical effects and are thus better captured by dynamical techniques such as MD than by statistical methods like MC.

### 2.2.1 Results and discussion

We will also perform MD simulations of carbon nanotubes based on the LCBOPII empirical potential. Because MD is slower than MC we cannot use the large (10,10,440) nanotube we used in the MC simulations with wavemoves. Instead, we use a (5,5,100) armchair nanotube, the same as used in the MD study

by Cao et. al [22]. This sample contains 2000 atoms, has a radius of 3.39 Å and a length of 245.9 Å. The MD routine cannot perform simulations in the  $NpT$  ensemble which we used for the MC simulations. Instead we use the canonical  $NVE$  ensemble, which has a fixed-size simulation box. We can calculate the pressure in this box as a function of time, from which we can see if the systems wants to expand or contract.

We performed the MD simulations at  $T = 400$  K, again with periodic boundary conditions along the nanotube axis. We start from an initial configuration which is obtained by equilibrating the (5,5,100) nanotube by MC simulations. This sample has a length of 244.53 Å. Starting from an equilibrated sample from the MC routine enables comparison between the two methods regarding the thermal expansion. The timestep used to integrate the equations of motion was set to  $\Delta t = 5 \times 10^{-16}$  s, which is generally considered as a value which enables simulations of long timescales while still yielding only small errors in the numerical integration procedure. Cao et. al found that the lowest frequency of the lateral vibration is equal to 0.037 THz. This corresponds to an oscillation period of 27 ps, which gives us an idea of the relevant timescales in the system. We let the simulation run for 150 ps, saving the atomic positions and extracting physical quantities such as pressure every 500 timesteps. This gives about 100 data points per period.

To compare the difference between the MD and MC simulations qualitatively we have calculated the position of the axis,  $A(z)$ , in the nanotube by equation (2.5) as a function of the coordinate along the nanotube axis,  $z$ . The results are shown in figures 2.11 and 2.12. The difference between the two methods is very clearly visible in this figures. Whereas the bending of the nanotube is visible in the MC data, the axis remains at a more or less fixed position over the entire sampling period. In the MD data however, we clearly see the nanotube axis oscillating in time. The amplitude of the MC oscillation seems somewhat larger than the MD oscillation but the amplitude of 3 Å found by Cao et. al is not nearly reached by both methods.

The average pressure, during the last 50 ps of the simulations, in the  $z$ -direction in the simulation box is equal to  $5.08 \times 10^8$  Pa. This even means that there is outward pressure from the box on the surroundings, and that the nanotube wants to expand further. This means, that also with MD simulations we find no thermal contraction of nanotubes. To make sure that the outward pressure is not an effect of an increase in bond length (which should not be the case since the MC and MD simulations were done at the same temperature) we calculated the radial distribution functions for both simulations techniques. The results, around the nearest neighbour distance are shown in figure 2.13. The two peaks overlap neatly proving that the bond lengths are the same in MC and MD simulations. From this brief excursion into the world of Molecular Dynamics simulations we can thus conclude that the bending modes are indeed present in the system but that it is unlikely to find negative CTEs with MD which is not found by MC sampling.

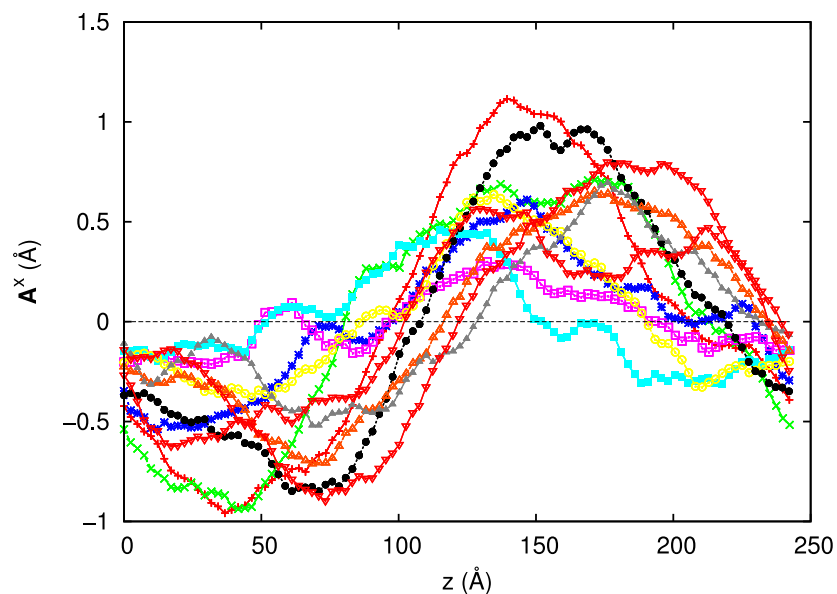


Figure 2.11: The  $x$ -coordinate of the axis,  $A^x$ , of the (5,5,100) nanotube as a function of height  $z$  obtained from Monte Carlo simulations. Data was taken every 5000 MC steps.

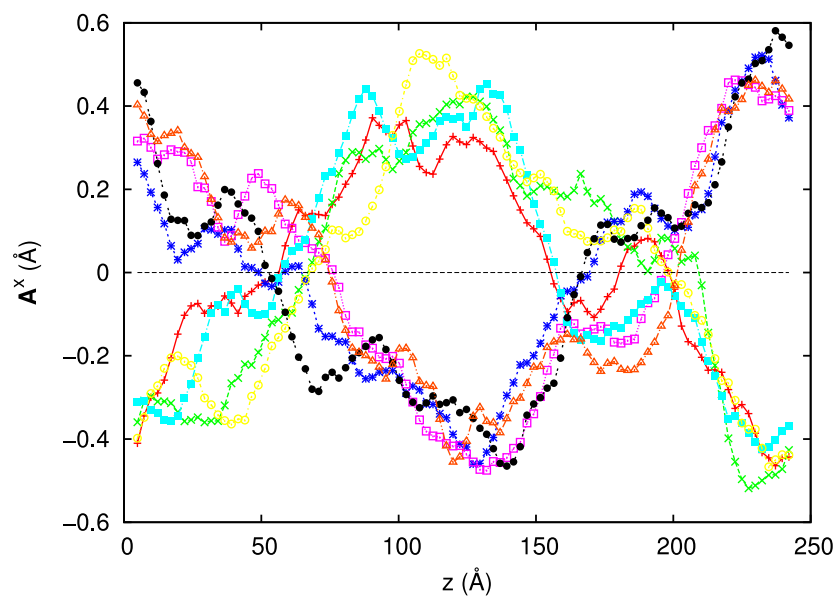


Figure 2.12: The  $x$ -coordinate of the axis,  $A^x$ , of the (5,5,100) nanotube as a function of height  $z$  obtained from Molecular Dynamics simulations. Data was taken every 5 ps.

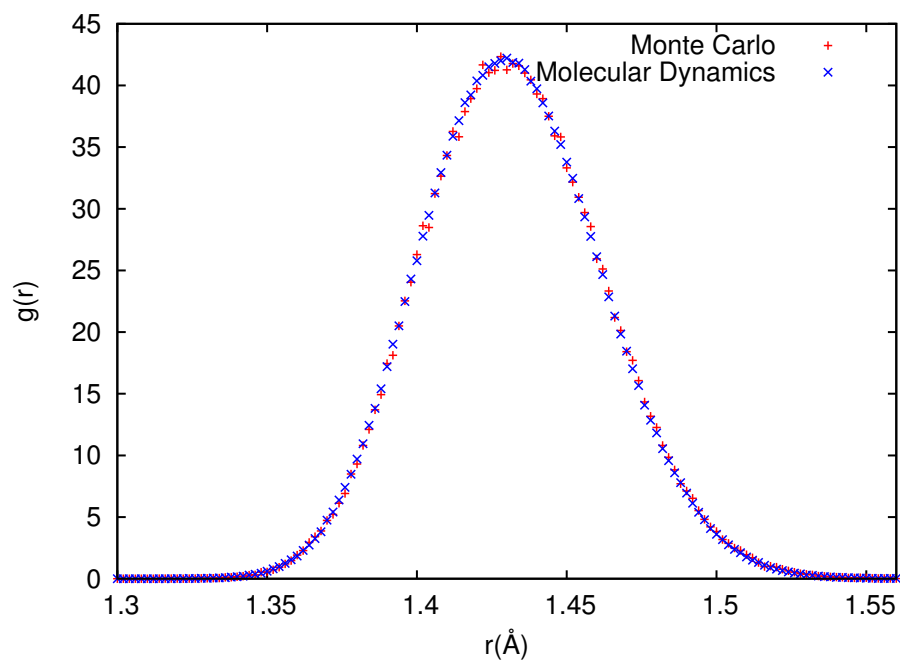


Figure 2.13: Radial distribution functions of the (5,5,100) nanotube at  $T = 400$  K computed from MC and MD results

# 3

## Lattice Dynamics

Although atomistic simulations are a great tool for studying large systems with complex, long-range, interactions they do not always provide a lot of insight in the fundamental physical processes at the source of the behaviour of the system. The reason for this is that the output which we receive from these simulations is always the sum of all processes going on and from that sum it is often difficult to isolate the contribution of a specific process.

In this chapter we will take a more theoretical approach by means of the theory of lattice dynamics. This theory describes the elementary structural excitations of crystalline solids which, in turn, have their impact on the structure of the crystal. When applying this theory to our carbon systems we will still be relying on LCBOPII to describe the interactions between carbon atoms so the results can be compared to those of the previous chapter. However, some approximations have to be made in order to apply the theory.

Using lattice dynamics we will be able to calculate the energy of vibrational modes of various graphitic crystals which play a key role in the thermal expansion. We will calculate the coefficients of thermal expansion by minimizing the quasiharmonic free energy of the systems with respect to their structural parameters.

### 3.1 Theory of lattice dynamics

In order to understand the vibrational modes of a certain crystal we consider the potential energy,  $U$ , which is a function of the coordinates. The crystal contains an infinite number of unit cells labeled by an integer vector  $\mathbf{l} = (l_x, l_y, l_z)$ . Every unit cell contains  $N$  atoms labeled by an integer  $k$ . The position of atom  $k$  in unit cell  $\mathbf{l}$  is denoted by  $\mathbf{r}(\mathbf{l}k) = \mathbf{r}^0(\mathbf{l}k) + \mathbf{u}(\mathbf{l}k)$  where  $\mathbf{r}^0$  and  $\mathbf{u}$  are the equilibrium position and the displacement vectors of atom  $(\mathbf{l}k)$ . The equilibrium position of atom  $(\mathbf{l}k)$  is written as  $\mathbf{r}^0(\mathbf{l}k) = \mathbf{R}_\mathbf{l} + \mathbf{x}_k$  where  $\mathbf{R}_\mathbf{l}$  denotes the position of cell  $\mathbf{l}$  and  $\mathbf{x}_k$  the position of atom  $k$  with respect to  $\mathbf{R}_\mathbf{l}$ . The Cartesian components of the vectors are denoted by Greek indices  $\alpha$  and  $\beta$ .

We expand the potential energy function in terms of the displacements  $\mathbf{u}$ , which we assume to be small<sup>1</sup> so we only expand up to second order. This is known as the harmonic approximation:

$$U \approx U_0 + \sum_{\mathbf{l}k\alpha} \left( \frac{\partial U}{\partial u_\alpha(\mathbf{l}k)} \right)_0 u_\alpha(\mathbf{l}k) + \frac{1}{2} \sum_{\mathbf{l}k\alpha, \mathbf{l}'k'\beta} \left( \frac{\partial^2 U}{\partial u_\alpha(\mathbf{l}k) \partial u_\beta(\mathbf{l}'k')} \right)_0 u_\alpha(\mathbf{l}k) u_\beta(\mathbf{l}'k'). \quad (3.1)$$

The first term is a constant,  $U_0$ , which is just the equilibrium cohesive energy of the crystal. The second term is actually equal to zero because we have expanded the potential around its minimum. So the only term of importance depends on the second derivatives of the potential which we will from now on call the force constant matrix, denoted by  $\phi_{\alpha\beta}(\mathbf{l}k, \mathbf{l}'k')$ . This means that equation (3.1) can be written as

$$U \approx U_0 + \frac{1}{2} \sum_{\mathbf{l}k\alpha, \mathbf{l}'k'\beta} \phi_{\alpha\beta}(\mathbf{l}k, \mathbf{l}'k') u_\alpha(\mathbf{l}k) u_\beta(\mathbf{l}'k'). \quad (3.2)$$

The name force constant matrix arises because this matrix describes the force on atom  $(\mathbf{l}k)$  arising from the displacements of the other atoms. This becomes clear upon taking the gradient of the expansion of  $U$  to compute the force  $F(\mathbf{l}k)$  on atom  $(\mathbf{l}k)$ :

$$F_\alpha(\mathbf{l}k) = - \frac{\partial U}{\partial u_\alpha(\mathbf{l}k)} \approx - \sum_{\mathbf{l}'k'\beta} \phi_{\alpha\beta}(\mathbf{l}k, \mathbf{l}'k') u_\beta(\mathbf{l}'k'), \quad (3.3)$$

where we have made use of the symmetry of the second derivative. Because of the periodicity of the crystal the force constant matrix actually does not depend on the unit cells  $\mathbf{l}$  and  $\mathbf{l}'$  separately but only on the difference  $\mathbf{R}_\mathbf{l} - \mathbf{R}_{\mathbf{l}'}$ . Since the force constant matrix can, in principle, be calculated by simply taking derivatives of the potential energy we can now write down the equations of motion for each atom. If atom  $k$  in the unit cell has mass  $m_k$  then the equations of motion become

$$m_k \ddot{u}_\alpha(\mathbf{l}k) = - \sum_{\mathbf{l}'k'\beta} \phi_{\alpha\beta}(\mathbf{l}k, \mathbf{l}'k') u_\beta(\mathbf{l}'k'). \quad (3.4)$$

We look for periodic solutions to this equation of the following form

$$u_\alpha(\mathbf{l}k, t) = \frac{A_{\alpha,k}(\mathbf{q})}{\sqrt{m_k}} \exp \{i(\mathbf{q} \cdot \mathbf{R}_\mathbf{l} - \omega(\mathbf{q})t)\}, \quad (3.5)$$

where we have introduced a wavevector  $\mathbf{q}$  and frequency  $\omega(\mathbf{q})$ . The vector  $A_{\alpha,k}(\mathbf{q})$  is simply the amplitude of the wave. Inserting this ansatz into the equation of motion gives

$$\omega^2(\mathbf{q}) \exp \{i\mathbf{q} \cdot \mathbf{R}_\mathbf{l}\} A_{\alpha,k}(\mathbf{q}) = \sum_{\mathbf{l}'k'\beta} \frac{1}{\sqrt{m_k m'_k}} \phi_{\alpha\beta}(\mathbf{l}k, \mathbf{l}'k') \exp \{i\mathbf{q} \cdot \mathbf{R}_{\mathbf{l}'}\} A_{\beta,k'}(\mathbf{q}), \quad (3.6)$$

which we can rewrite in the form of an eigenvalue equation in the following way:

$$\omega^2(\mathbf{q}) A_{\alpha,k}(\mathbf{q}) = \sum_{k'\beta} \left[ \frac{1}{\sqrt{m_k m'_k}} \sum_{\mathbf{l}'} \phi_{\alpha\beta}(\mathbf{l}k, \mathbf{l}'k') \exp \{i\mathbf{q} \cdot (\mathbf{R}_{\mathbf{l}'} - \mathbf{R}_\mathbf{l})\} \right] A_{\beta,k'}(\mathbf{q}). \quad (3.7)$$

<sup>1</sup>this is generally true for stable crystals at low temperatures

This equation motivates us to define the expression inside the square brackets as the  $3N \times 3N$ , hermitian, dynamical matrix  $D_{\alpha\beta}(k, k', \mathbf{q})$

$$D_{\alpha\beta}(k, k', \mathbf{q}) \equiv \frac{1}{\sqrt{m_k m'_k}} \left[ \sum_{l'l'} \phi_{\alpha\beta}(lk, l'k') \exp \{i\mathbf{q} \cdot (\mathbf{R}_{l'} - \mathbf{R}_l)\} \right]. \quad (3.8)$$

With this definition equation (3.7) takes the following final form:

$$\omega^2(\mathbf{q}) A_{\alpha,k}(\mathbf{q}) = \sum_{\beta k'} D_{\alpha\beta}(k, k', \mathbf{q}) A_{\beta,k'}(\mathbf{q}) \quad (3.9)$$

This system of  $3N$  linear equations has nontrivial solutions if the following determinant is equal to zero

$$\left| D_{\alpha\beta}(k, k', \mathbf{q}) - \delta_{\alpha\beta} \delta_{kk'} \omega^2(\mathbf{q}) \right| = 0. \quad (3.10)$$

The frequencies of the vibrational modes can thus be calculated as the square root of the eigenvalues of the dynamical matrix at any value of the wavevector  $\mathbf{q}$ . Because the dynamical matrix is hermitian, the eigenvalues are necessarily real and the resulting frequencies thus either purely real or purely imaginary. In view of equation (3.5) however, we see that purely imaginary frequencies lead to oscillations which grow exponentially and will thus destroy the stability of the crystal.

At every value of  $\mathbf{q}$  there will be  $3N$  solutions which we will label by an integer  $j$ . So we will have  $3N$  frequency branches  $\omega(\mathbf{q}, j)$ , with corresponding eigenvectors  $A_{\alpha,k}(\mathbf{q}, j)$ . These eigenvectors are not fully determined by equation (3.9) and we are free to choose them such that they satisfy the orthonormality relations

$$\sum_{\alpha,k} A_{\alpha,k}(\mathbf{q}, j) A_{\alpha,k}^*(\mathbf{q}, j') = \delta_{j,j'}, \quad (3.11a)$$

$$\sum_j A_{\alpha,k}(\mathbf{q}, j) A_{\beta',k'}^*(\mathbf{q}, j) = \delta_{\alpha,\beta} \delta_{k,k'}. \quad (3.11b)$$

From the definition of the dynamical matrix (3.8) we also see that

$$D_{\alpha\beta}(k, k', \mathbf{q}) = D_{\alpha\beta}^*(k, k', -\mathbf{q}). \quad (3.12)$$

Upon taking the complex conjugate of equation (3.9) this implies that (since  $\omega^2(\mathbf{q}, j)$  is always real)

$$A_{\alpha,k}(\mathbf{q}, j) = A_{\alpha,k}^*(-\mathbf{q}, j). \quad (3.13)$$

Equations (3.12) and (3.13) imply, through equation (3.9) that

$$\omega^2(\mathbf{q}, j) = \omega^2(-\mathbf{q}, j). \quad (3.14)$$

### 3.1.1 Quantization and normal coordinates

In the harmonic approximation, the Hamiltonian of the crystal can be written in the following way:

$$H = T + V = \frac{1}{2} \sum_{lk\alpha} \frac{p_\alpha(lk) p_\alpha(lk)}{m_k} + \frac{1}{2} \sum_{\substack{lk\alpha \\ l'k'\beta}} \phi_{\alpha\beta}(lk, l'k') u_\alpha(lk) u_\beta(l'k'), \quad (3.15)$$

where we have used the second order expansion of the potential energy from equation (3.2), and introduced the momenta of the particles  $p_\alpha(lk) = m_k \dot{u}_\alpha(lk)$ . Next, we will diagonalize this Hamiltonian by introducing the normal coordinates  $Q(\mathbf{q}, j)$  and  $P(\mathbf{q}, j)$  in the following way:

$$u_\alpha(lk) = \sum_{\mathbf{q}, j} \frac{1}{\sqrt{m_k N_c}} A_{\alpha,k}(\mathbf{q}, j) Q(\mathbf{q}, j) e^{i\mathbf{q} \cdot \mathbf{R}_l}, \quad (3.16a)$$

$$p_\alpha(lk) = \sum_{\mathbf{q}, j} \sqrt{\frac{m_k}{N_c}} A_{\alpha,k}(\mathbf{q}, j) P(\mathbf{q}, j) e^{i\mathbf{q} \cdot \mathbf{R}_l}, \quad (3.16b)$$

where  $N_c$  is the number of unit cells in the crystal. Since the displacements  $u_\alpha(\mathbf{l}k)$  must be real it follows from condition (3.13) that

$$Q(\mathbf{q}, j) = Q^*(-\mathbf{q}, j) \quad \text{and} \quad P(\mathbf{q}, j) = P^*(-\mathbf{q}, j). \quad (3.17)$$

Using these transformations on the Hamiltonian (3.15), together with equation (3.9) and the fact that  $N_c^{-1} \sum_{\mathbf{l}} \exp(i\mathbf{q} \cdot \mathbf{R}_{\mathbf{l}})$  equals 1 if  $\mathbf{q}$  is a reciprocal lattice vector and zero otherwise gives us

$$H = \frac{1}{2} \sum_{\mathbf{q}, j} \left( P^*(\mathbf{q}, j) P(\mathbf{q}, j) + \omega^2(\mathbf{q}, j) Q^*(\mathbf{q}, j) Q(\mathbf{q}, j) \right). \quad (3.18)$$

So the Hamiltonian is indeed diagonalized and we recognize the Hamiltonian of a set of harmonic oscillators with frequencies  $\omega(\mathbf{q}, j)$ . The modes corresponding to the numbers  $(\mathbf{q}, j)$  are called the normal modes of the crystal, and the coordinates  $Q$  and  $P$  are the normal coordinates.

To quantize these lattice vibrations we replace the normal coordinates and momenta by the operators  $\hat{Q}(\mathbf{q}, j)$  and  $\hat{P}(\mathbf{q}, j)$ . We can calculate the commutator between these operators from the inverse transformation of (3.16):

$$Q(\mathbf{q}, j) = \sum_{\mathbf{l}k\alpha} \sqrt{\frac{m_k}{N_c}} A_{\alpha,k}^*(\mathbf{q}, j) u_\alpha(\mathbf{l}k) e^{-i\mathbf{q} \cdot \mathbf{R}_{\mathbf{l}}}, \quad (3.19a)$$

$$P(\mathbf{q}, j) = \sum_{\mathbf{l}k\alpha} \frac{1}{\sqrt{m_k N_c}} A_{\alpha,k}^* p_\alpha(\mathbf{l}k) e^{-i\mathbf{q} \cdot \mathbf{R}_{\mathbf{l}}}, \quad (3.19b)$$

and the fundamental commutation relations

$$[\hat{u}_\alpha(\mathbf{l}k), \hat{p}_\beta(\mathbf{l}'k')] = i\hbar \delta_{\alpha,\beta} \delta_{\mathbf{l},\mathbf{l}'} \delta_{k,k'} \quad \text{and} \quad [\hat{u}_\alpha(\mathbf{l}k), \hat{u}_\beta(\mathbf{l}'k')] = [\hat{p}_\alpha(\mathbf{l}k), \hat{p}_\beta(\mathbf{l}'k')] = 0. \quad (3.20)$$

The result of this calculation is

$$[\hat{Q}(\mathbf{q}, j), \hat{P}(\mathbf{q}', j')] = i\hbar \delta_{\mathbf{q}, -\mathbf{q}'} \delta_{j, j'}. \quad (3.21)$$

Next we perform one more transformation on the normal coordinate operators and introduce the bosonic quasiparticle creation and annihilation operators  $\hat{b}^\dagger(\mathbf{q}, j)$  and  $\hat{b}(\mathbf{q}, j)$ :

$$\hat{Q}(\mathbf{q}, j) = \sqrt{\frac{\hbar}{2\omega(\mathbf{q}, j)}} \left[ \hat{b}(\mathbf{q}, j) + \hat{b}^\dagger(-\mathbf{q}, j) \right], \quad (3.22a)$$

$$\hat{P}(\mathbf{q}, j) = -i\sqrt{\frac{\hbar\omega(\mathbf{q}, j)}{2}} \left[ \hat{b}(\mathbf{q}, j) - \hat{b}^\dagger(-\mathbf{q}, j) \right]. \quad (3.22b)$$

Using the relations (3.21) it is easily verified that these new operators indeed satisfy the bosonic commutation relations

$$[\hat{b}(\mathbf{q}, j), \hat{b}^\dagger(\mathbf{q}', j')] = \delta_{\mathbf{q}, \mathbf{q}'} \delta_{j, j'} \quad \text{and} \quad [\hat{b}(\mathbf{q}, j), \hat{b}(\mathbf{q}', j')] = [\hat{b}^\dagger(\mathbf{q}, j), \hat{b}^\dagger(\mathbf{q}', j')] = 0. \quad (3.23)$$

With this transformation, the Hamiltonian takes the following, more compact, and very well known form

$$\hat{H} = \sum_{\mathbf{q}, j} \left( \hat{b}^\dagger(\mathbf{q}, j) \hat{b}(\mathbf{q}, j) + \frac{1}{2} \right). \quad (3.24)$$

The vibrating lattice is thus now described as a gas of quantized harmonic oscillators with frequencies  $\omega(\mathbf{q}, j)$ . The operator  $\hat{b}^\dagger(\mathbf{q}, j) \hat{b}(\mathbf{q}, j)$  is the operator numbering the quasiparticles which we will refer to as phonons. The energy levels of each oscillator are quantized in quanta of  $\hbar\omega(\mathbf{q}, j)$  with a zero point energy of  $\frac{1}{2}\hbar\omega(\mathbf{q}, j)$ . The total energy  $E$  is specified by the occupation numbers  $n_{\mathbf{q}, j}$  and is given by

$$E_{\{n_{\mathbf{q}, j}\}} = U_0 + \sum_{\mathbf{q}, j} \hbar\omega(\mathbf{q}, j) \left( n_{\mathbf{q}, j} + \frac{1}{2} \right), \quad (n_{\mathbf{q}, j} = 0, 1, 2, \dots), \quad (3.25)$$

where we have included the ground state cohesive energy  $U_0$ .

### 3.1.2 Thermodynamic properties and the quasiharmonic approximation

At zero pressure, the equilibrium structure of the crystal at a finite temperature  $T$  can be found by minimizing the Helmholtz free energy  $F = U - TS$ . The free energy can be calculated through the partition function  $Z$  which we now know since we have the energy eigenvalues from equation (3.25)

$$Z = \sum_{\{n_{q,j}\}} e^{-\beta E_{\{n_{q,j}\}}} = e^{-\beta U_0} \prod_{q,j} \frac{e^{-\frac{\beta \hbar \omega(q,j)}{2}}}{1 - e^{-\beta \hbar \omega(q,j)}}, \quad (3.26)$$

where  $\beta = (k_B T)^{-1}$ . The free energy is

$$F = -k_B T \ln Z = U_0 + \sum_{q,j} \frac{\hbar \omega(q,j)}{2} + k_B T \sum_{q,j} \ln \left[ 1 - \exp \left( -\frac{\hbar \omega(q,j)}{k_B T} \right) \right] \quad (3.27)$$

The first term is simply the cohesive energy of the crystal. The sums over  $qj$  run over all allowed wavevectors in the first Brillouin zone and over all phonon branches. The second term is the zero point motion associated with the nonzero ground state energy of the quantum harmonic oscillator.

If the crystal is perfectly harmonic, as we have assumed up to this point, the only dependence of the free energy on the crystal structure is due to the dependence of the internal energy on the lattice parameters. This means that lattice parameters minimizing the free energy do not depend on temperature and there is no thermal expansion in the system. One of the methods to include some level of anharmonicity is to make the phonon frequencies dependent on the structural parameters of the crystal,  $\{\mathbf{a}_i\}$ . The expression for the free energy then becomes

$$F(\{\mathbf{a}_i\}, T) = U(\{\mathbf{a}_i\}) + \sum_{q,j} \frac{\hbar \omega(q,j, \{\mathbf{a}_i\})}{2} + k_B T \sum_{q,j} \ln \left[ 1 - \exp \left( -\frac{\hbar \omega(q,j, \{\mathbf{a}_i\})}{k_B T} \right) \right]. \quad (3.28)$$

This procedure is known as the quasiharmonic approximation [30] which has proven very successful in describing the thermodynamic properties of solids. The thermal expansion of crystals within the quasiharmonic approximation is described by Grüneisen theory [15, 30]. For an isotropic solid, the coefficient of thermal expansion is given by

$$\alpha = \frac{\sum_{q,j} c_{q,j} \gamma_{q,j}}{3VB}, \quad (3.29)$$

where  $V$  is the system volume,  $B$  is the bulk modulus,  $\gamma_{q,j}$  are the mode-dependent Grüneisen parameters and  $c_{q,j}$  is the contribution to the specific heat from mode  $qj$ :

$$c_{q,j} = k_B \left( \frac{\hbar \omega(q,j)}{2k_B T} \right)^2 \left[ \sinh \left( \frac{\hbar \omega(q,j)}{2k_B T} \right) \right]^{-1}. \quad (3.30)$$

The Grüneisen parameters are defined as the logarithmic derivatives of the phonon frequencies with respect to volume:

$$\gamma_{q,j} = -\frac{\partial \ln \omega(q,j)}{\partial \ln V} \quad (3.31)$$

The Grüneisen parameters are generally positive in solids because with increasing volume, force constants become lower causing phonon frequencies decrease. Since the mode heat capacities,  $c_{q,j}$ , are always positive, this gives rise to positive coefficients of thermal expansion. Some systems however, have phonon modes with negative Grüneisen parameters. This usually occurs in transverse modes, where an increase in volume leads to higher frequencies (think for example of a simple vibrating string held by its two ends, its vibrational frequency goes up if you pull harder on the string). In this case, the overall sign of  $\alpha$  is determined by the competition between the modes with positive and negative Grüneisen parameters.

For anisotropic solids the expressions for the thermal expansion tensor  $\alpha_{ij}$  are more complicated but the sign of the thermal expansion is still determined by the mode-dependent Grüneisen parameters, albeit derivatives are now taken with respect to components of the strain tensor.

In this thesis we will perform direct numerical minimization of the free energy (3.28) as a function of the structural parameters of the crystal. Calculation of the Grüneisen parameters however, is still useful because it provides insight into the role which different phonon play in the thermal expansion of contraction of the crystal.

### 3.1.3 Numerical calculation of phonon dispersion relations

The formalism described in the previous section provides us with a very straightforward method for calculating phonon dispersions numerically. If the potential energy of the crystal as a function of the atom coordinates is known, then the force constant matrix can be calculated by taking the second derivatives of the potential energy. Once these are known, equation (3.8) can be used to compute the dynamical matrix  $D$ . The final step is computing the eigenvalues of this, often rather large, matrix at the desired values of  $\mathbf{q}$ . This approach of calculating the phonon dispersion relations of a crystal is known as the small displacement method.

Even though the procedure is quite straightforward, there are a couple of issues. The first is the calculation of the force constants. To calculate all force constants between two atoms, both atoms are displaced over a distance of  $\epsilon$  in three independent directions. In this work we have chosen  $\epsilon = 5 \times 10^{-3}$  Å, which is 0.35% of the nearest neighbour distance,  $a_{CC}$ , in graphitic systems. The potential energy is evaluated for every configuration and the derivatives are calculated by means of the central difference algorithm. Since both atoms are given positive and negative displacements along three directions this means we have to calculate the cohesive energy of the crystal 36 times in order to obtain all force constants between the two atoms. Luckily, the number of force constants that need to be calculated can be greatly reduced by making use of the symmetries of the crystal. Translational invariance between the different unit cells for instance means that we only have to calculate the force constants connecting every atom in *one* cell with all other atoms. The symmetry of the second derivative also reduces the amount of constants to be calculated:

$$\phi_{\alpha\beta}(\mathbf{l}k, \mathbf{l}'k') = \phi_{\beta\alpha}(\mathbf{l}'k', \mathbf{l}k). \quad (3.32)$$

Other symmetries of the crystal can of course also be exploited. If for example we have an element,  $S$ , of the point group of the crystal; application of  $S$  leaves the crystal, and thus also the potential energy invariant. Application of  $S$  on the position vector of atom  $(\mathbf{l}k)$  sends it to the position vector of atom  $S(\mathbf{l}k)$ :

$$r_{\alpha}^0(S(\mathbf{l}k)) = S_{\alpha\beta} r_{\beta}^0(\mathbf{l}k), \quad (3.33)$$

where  $S_{\alpha\beta}$  is the  $3 \times 3$  Cartesian matrix representation of  $S$  and summation over repeated indices is assumed. When applied to the force constant matrix the symmetry operation has the following effect:

$$\phi_{\alpha\beta}(S(\mathbf{l}k), S(\mathbf{l}'k')) = S_{\alpha\delta} \phi_{\delta\gamma}(\mathbf{l}k, \mathbf{l}'k') S_{\gamma\beta}^{-1}. \quad (3.34)$$

With this equation it is possible to quickly generate a bunch of new force constants once the force constant between two atoms has been explicitly calculated. This not only reduces the number of constants that need to be calculated but also imposes the symmetry of the crystal on the force constants in an exact way, reducing numerical errors.

Perhaps the most important symmetry one has to consider when calculating phonon dispersions based on this force constant model is the condition of translational invariance of the crystal as a whole. This symmetry is very important because it is the reason why every crystal in three dimensions has at least three acoustic branches with zero frequency at  $\mathbf{q} = 0$ . Translational invariance requires that the potential energy does not change when we displace all atoms in the crystal by the same amount, thus setting  $u_{\alpha}(\mathbf{l}k) = u_{\alpha}$  in equation (3.1). Since equation (3.1) must be independent of the specific values of  $u_{\alpha}$  this imposes the following conditions on the derivatives of  $U$ :

$$\sum_{\mathbf{l}k} \left. \frac{\partial U}{\partial u_{\alpha}(\mathbf{l}k)} \right|_0 = 0 \quad \text{and} \quad \sum_{\mathbf{l}'k'} \left. \frac{\partial^2 U}{\partial u_{\alpha}(\mathbf{l}k) \partial u_{\beta}(\mathbf{l}'k')} \right|_0 = 0 \quad \forall \mathbf{l}, k, \alpha, \beta, \quad (3.35)$$

or in terms of the force constant matrix:

$$\sum_{\mathbf{l}'k'} \phi_{\alpha\beta}(\mathbf{l}k, \mathbf{l}'k') = 0 \quad \forall \mathbf{l}, k, \alpha, \beta. \quad (3.36)$$

Insertion of this condition into equation (3.9) immediately shows that at  $\mathbf{q} = 0$  there are three linearly independent eigenvectors with corresponding eigenvalues  $\omega^2(\mathbf{0}) = 0$ . To make sure that the acoustic modes go exactly to zero frequency at the zone center, equation (3.36) has to be exactly satisfied. Due to numerical errors this is not always the case in our calculations. We therefore reimpose the condition after the force constant matrix has been calculated in such a way that the symmetry condition (3.32) is not violated.

In this work, we calculate the force constants from the LCBOPII potential numerically. These calculations are carried out in a supercell with periodic boundary conditions in the appropriate directions for the system under consideration. The dimensions in the periodic directions of the supercell are at least 6 Å, which is the radius of the potential. If symmetry properties are used, according to equation (3.34), it will be noted. Once the force constant matrix is known, its eigenvalues are determined numerically by means of the `ZHEEV()` routine from the LAPACK linear algebra package [31].

### 3.1.4 Integration over the Brillouin zone

In the calculation of the thermodynamic properties of a system one often needs to perform integrations (or summations) of some function over the Brillouin zone in reciprocal space. This is for example the case when we want to calculate the free energy of a system from equation (3.28). To compute such integrals numerically a suitable mesh of  $q$ -points is needed over which to integrate the function. The convergence of the integral highly depends on the choice of this mesh. One of the most common and proven ways to construct such a mesh was proposed by Monkhorst and Pack [32]. The Monkhorst-Pack (MP) mesh is a homogeneous grid of  $q$ -points with the rows of points parallel to the reciprocal lattice vectors. If we denote the number of points along each reciprocal lattice vector by  $n_i$  ( $i = 1, 3$ ) the resulting grid contains  $N = n_1 \times n_2 \times n_3$  points labeled by three integers  $m_i$  ( $i = 1, 3$ ) at positions

$$\mathbf{q}_{m_1, m_2, m_3} = \frac{m_1}{n_1} \mathbf{b}_1 + \frac{m_2}{n_2} \mathbf{b}_2 + \frac{m_3}{n_3} \mathbf{b}_3 \quad (m_i = 0, \dots, n_i - 1). \quad (3.37)$$

This set of  $q$  vectors specifically includes the zone center when all three  $m_i$ 's are equal to zero. This is often not desirable for a fast convergence and therefore one often adds an offset vector  $\Delta$  to the  $q$  points in the mesh so the total mesh becomes

$$\mathbf{q}_{m_1, m_2, m_3} = \frac{m_1}{n_1} \mathbf{b}_1 + \frac{m_2}{n_2} \mathbf{b}_2 + \frac{m_3}{n_3} \mathbf{b}_3 + \Delta \quad (m_i = 0, \dots, n_i - 1). \quad (3.38)$$

As an example a MP mesh for graphene is shown in figure 3.1 with an offset  $\Delta$ . This offset is chosen at the center of the 'bin' cornered by four neighbouring meshpoints. The number of meshpoints may still be greatly reduced by making use of the point group symmetry operations of the crystal, since the point groups of the real space and the reciprocal space of a lattice are the same.

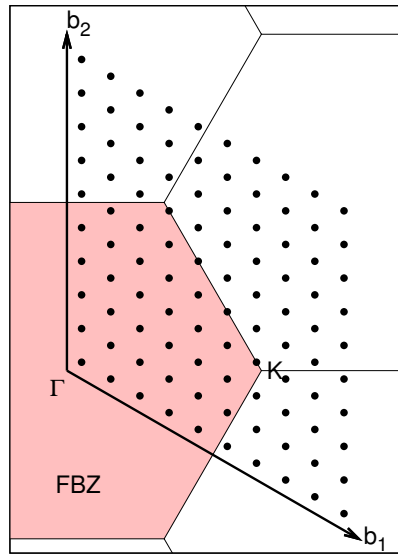


Figure 3.1:  $10 \times 10$  Monkhorst Pack grid in the reciprocal space of graphene with an offset from the zone center  $\Gamma$ .

## 3.2 Phonon dispersions

### 3.2.1 The 1-dimensional carbon chain

To put the developed code to test, the first system we will consider is the one dimensional chain of carbon atoms. The phonon dispersion of the infinite linear mono atomic array can easily be solved analytically and is therefore a useful system to start with. If only nearest neighbour interactions are taken into account the solution is [33, chap. 4]

$$\omega(q) = \sqrt{\frac{4C_1}{m}} \left| \sin\left(\frac{1}{2}qa\right) \right|, \quad (3.39)$$

where  $q$  is the wavevector,  $C_1$  is the force constant between nearest neighbours,  $a$  is the distance between the carbon atoms and  $m$  is the carbon atomic mass. In our calculations however, interactions will not be limited to first neighbours and we need a bit more realistic model. Therefore we add force constants  $C_i$  between all  $i$ 'th nearest neighbours and derive the dispersion relation following the steps in section 3.1. The result is

$$\omega(q) = \sqrt{\sum_{i=1}^{\infty} \frac{4C_i}{m} \sin^2\left(\frac{qai}{2}\right)}. \quad (3.40)$$

The lattice parameter  $a$  is determined to be 1.325Å by simply minimizing the total energy of a linear chain of 25 carbon atoms with the LCBOPII potential. To calculate the phonon dispersion relation we use a  $1 \times 1 \times 25$  supercell with periodic boundary conditions in the  $z$ -direction and one carbon atom per primitive cell. The wavevector  $q$  can take values between  $q = \mathbf{0}$  and  $q = \frac{2\pi}{a}\hat{z}$ . The calculated dispersion relation is shown in figure 3.2. A fit according to equation (3.39) is also shown. The frequencies of the phonon branches are given in inverse centimeters because this is the most used unit in the literature ( $1 \text{ cm}^{-1} = 2.99 \times 10^{10} \text{ Hz} = 0.124 \text{ meV}$ ). Because we cannot simulate a truly one-dimensional system we find three phonon acoustic branches, one longitudinal (LA) and two transverse (TA), as expected in a crystal with one atom per unit cell. The TA modes, with displacements in the  $x$ - and  $y$ -directions are of course degenerate and have the lowest frequencies. The longitudinal mode clearly shows the  $|\sin(\dots)|$  behaviour of equation (3.39) indicating that the nearest neighbour interactions are dominating the vibrational spectrum. The first three theoretical force constants calculated from the potential are listed in table 3.1.

To check the calculated relation we fitted equation (3.40) with force constants up to  $C_3$  to the data. This fit is also shown in figure 3.2. The inclusion of more force constants indeed increases the quality of the fit. The force constants from this fit are shown in table 3.1. The fit reproduces the theoretical force constants very accurately so we can conclude that the code produces correct dispersion relations once the force constants have been calculated. This however implicates nothing about the correctness of the force constants themselves. This is something which can only be checked by applying the machinery to physically existing systems and checking the results with experimental values. This will be done in the following sections for graphene, bilayer graphene graphite and carbon nanotubes.

Table 3.1: First three force constants of the linear atomic carbon chain in  $\text{eV}/\text{\AA}^2$ . Theoretical constants are calculated from the LCBOPII potential

Force constant	Theoretical	Fit from fig. 3.2
$C_1$	58.24	58.24
$C_2$	$8.932 \times 10^{-1}$	$8.932 \times 10^{-1}$
$C_3$	$1.818 \times 10^{-3}$	$1.072 \times 10^{-2}$

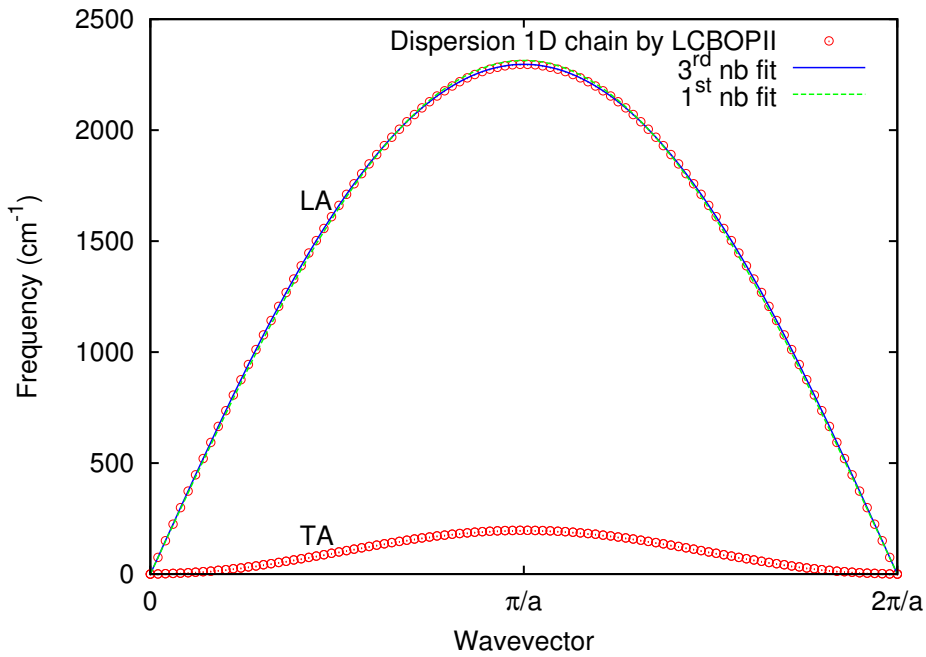


Figure 3.2: Phonon branches of the linear carbon chain with the best fits to equation (3.39), with 1<sup>st</sup> nearest neighbour interactions and (3.40), with 3<sup>rd</sup> nearest neighbour interactions.

### 3.2.2 Graphene

The first truly interesting system of which we will calculate the phonon dispersions is graphene. Since it has only two atoms per unit cell, it has just six phonon branches making it a very apprehensible system to start with<sup>2</sup>. But graphene also is the basic building block of other graphitic materials such as graphite, bilayer graphene and carbon nanotubes. Therefore the properties of the graphene phonon modes will be strongly reflected in all these materials and knowledge of the graphene phonons will help a lot with the understanding of the more complex systems.

#### Calculations and results

Using the technique described in section 3.1 we calculated the phonon dispersion of graphene. The force constants are calculated in a rectangular supercell of  $32 \text{ \AA} \times 38 \text{ \AA}$  containing 468 atoms with periodic boundary conditions in the direction of the sheet ( $xy$ -direction) and free boundary conditions in the  $z$ -direction. The carbon-carbon distance was fixed at  $a_{CC} = 1.4198 \text{ \AA}$ , the value that minimizes the total energy according to LCBOP II at  $-7.3502 \text{ eV/atom}$ .

In order to achieve as accurate results as possible, we explicitly impose the threefold rotation symmetry around the  $z$ -axis through each atom. If for example the force constant matrix between an atom in the reference cell and one of its nearest neighbours has been calculated, then using equation (3.34) the force constants to the other two nearest neighbours can be calculated by using a simple rotation matrix. In this way the force constant matrices up to fifth nearest neighbours are generated from one reference matrix at each neighbour level (see figure 3.3 for the nearest neighbours in graphene). This procedure requires computer code that is specifically written for the case of graphene but it prevents small errors from the numerical differentiation procedure to break the symmetry of the crystal.

In figure 3.4 the resulting phonon dispersion is shown along the three high symmetry lines in the first Brillouin zone connecting the zone center  $\Gamma$ , the  $K$ -point and the  $M$ -point (see section 1.2.1 for a description of the Brillouin zone). As expected, there are six phonon branches including three acoustic

<sup>2</sup>Note that even though graphene is a two-dimensional crystal it is embedded in three dimensional Euclidean space and the atoms are allowed to move in the direction perpendicular to the plane.

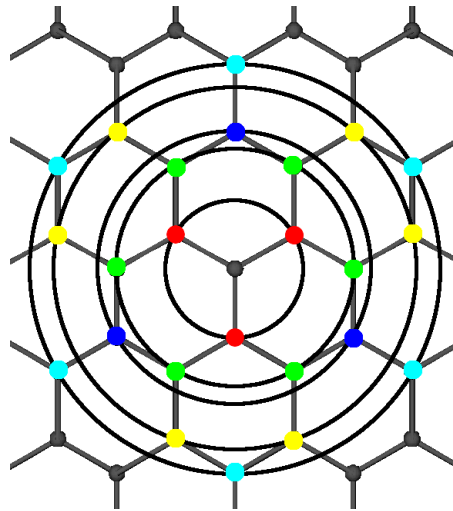


Figure 3.3: Positions of the nearest neighbours in graphene up to 5th nearest neighbours connected by circles for easy viewing.

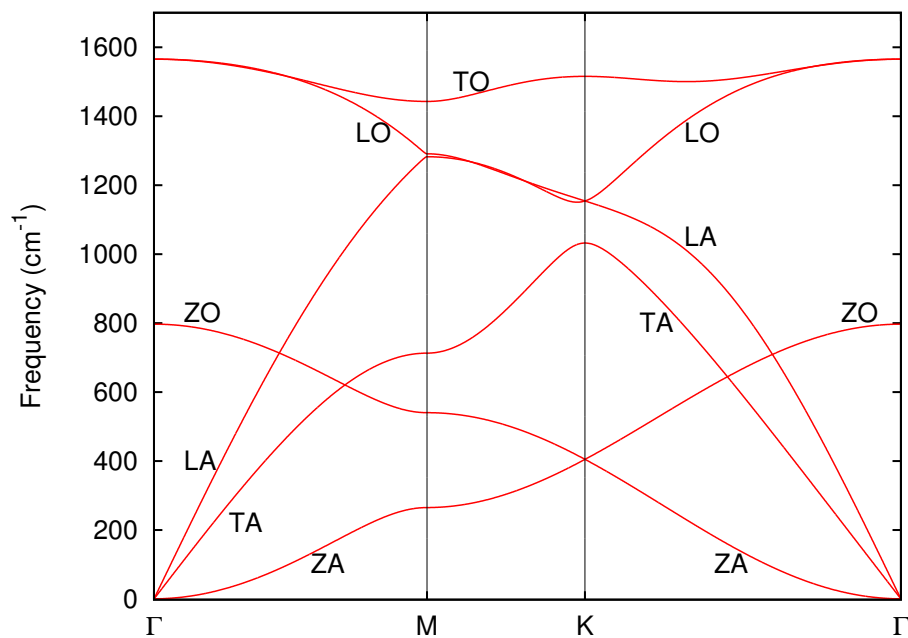


Figure 3.4: Phonon dispersion of graphene from the force constants of LCBOP11.

branches with zero frequency at the zone center corresponding to translations of the entire sheet in three independent directions. The remaining three branches are optical and have finite frequencies at  $\Gamma$ . We name the phonon branches as follows: an L stands for in-plane longitudinal polarization, T for in-plane transverse polarization and Z stands for out-of-plane polarized where the atoms move in the  $z$ -direction perpendicular to the plane. Furthermore we use an A to refer to acoustic modes and an O for optical modes.

The TA and the LA modes show a regular linear dispersion relation near the  $\Gamma$ -point but the out-of-plane ZA mode has a quadratic dispersion relation. The ZA mode is a so called bending mode, the two atoms in the unit cell move in phase in the  $z$ -direction, which, at long wavelengths, tends to bend the surface resulting in rippling of the graphene sheet. The quadratic dispersion behaviour is typical for layered crystals [34]. The softness of this mode also means that it plays a dominant role at low temperatures where the higher energy phonon modes are still not excited. But not only the acoustic out-of-plane branch has a low frequency, the ZO mode also has a considerably lower energy than the other optical branches. This can be explained as a consequence of the fact that the atoms are much more free to move in the direction perpendicular to the plane than in the plane itself. This causes force constants to be lower resulting in lower frequencies. Using group theory one can show that at the  $K$ -point the ZA and ZO modes and the TO and LO modes should be degenerate. These degeneracies are indeed properly reproduced by our calculations.

### Comparison with experiment

As far as we know, the phonon dispersion of graphene has not been measured experimentally but a lot of numerical studies have been done using either *ab initio* techniques ([14, 35, 36, 37]) or force constant models ([2, 38, 39]) which all show that the graphene phonon branches almost coincide with those of graphite. This can be explained as a result of the weak interaction between the graphite layers. For graphite there have been a lot of experimental studies using electron energy loss spectroscopy ([40, 41]), inelastic x-ray scattering ([35, 39])<sup>3</sup>. For this reason we will compare our graphene phonon dispersion to the experimental data for graphite, as shown in figure 3.5. The exact values of the frequencies from experiment and LCBOPII at the high symmetry points are also listed in table 3.2.

The overall agreement with the experiments is not bad considering the potential was not fitted to reproduce graphitic force constants beyond first nearest neighbours. Comparing to the phonon dispersions from other empirical potentials, LCBOPII performs very well. The popular Tersoff [25] and Brenner [26] potentials both predict too high frequencies for the highest optical modes (up to 40% too high for The Tersoff potential), as was recently shown by Lindsay and Broido [45]. These results are shown in figure 3.6. Besides the highest optical modes, also the in-plane acoustic modes (LA and TA) are reproduced better by LCBOPII. The frequencies of the ZA mode are predicted lower than the experimental values by the Tersoff and Brenner potentials, just as we saw for LCBOPII. The longest wavelength ZA phonons however, seem slightly better reproduced by the Tersoff and Brenner potentials than by LCBOPII.

Generally, the shape of the LCBOPII predicted branches is in accordance with the experiments but quantitatively there are pretty large discrepancies. The biggest difference is the shape of the TO mode along the  $M - K$  line where experiments and *ab initio* calculations predict much lower frequencies than the ones found by us. The difference reaches 15% at the  $K$ -point. Another feature that is not present in our dispersion but shows up in all experiments and *ab initio* results is the so called overbending of the LO mode near the  $\Gamma$  point. This means that the highest optical phonon frequency does not occur at the zone center, which is usually the case, but at some other point in the Brillouin zone. The out-of-plane ZA and ZO modes are both found to be a lot softer than the measurements, but their shape is in good agreement. The difference in frequency is at least 16% at the  $K$ -point, where the modes are degenerate. One reason for the lower frequencies is that the experimental results are for graphite where the atoms are less free to move in the out-of-plane direction due to the multiple layers present. This results in higher force constants and higher frequencies. But as we shall later, when covering the graphite dispersion relation, this effect is indeed present but only yields differences in frequency of about  $5\text{-}10\text{ cm}^{-1}$ , not nearly enough to explain the low frequencies of our ZA and ZO modes.

<sup>3</sup>Usually inelastic neutron scattering is used for measuring phonon frequencies but this technique requires relatively large and pure samples which are hard to obtain for graphite.

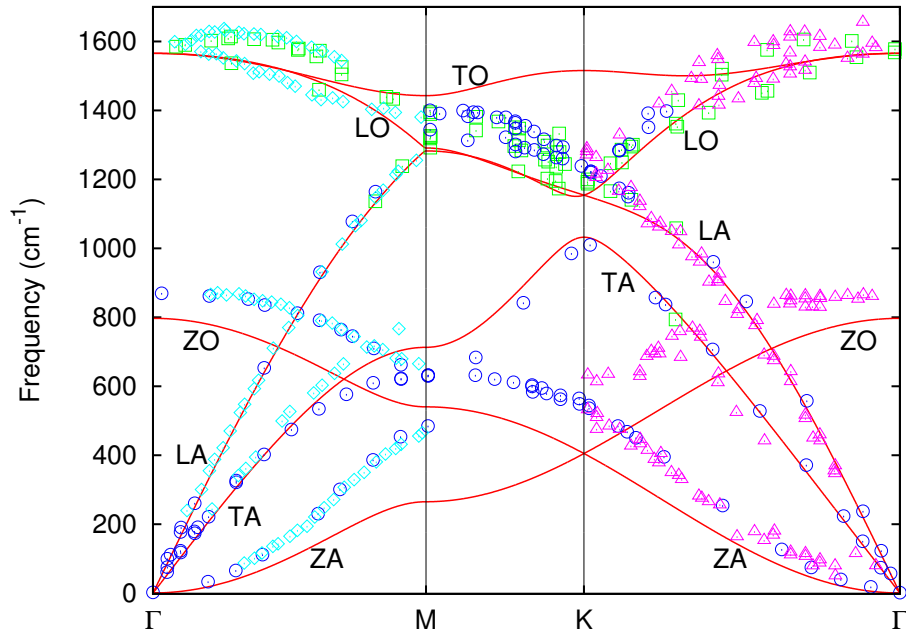


Figure 3.5: Dispersion relation for graphene as calculated from the LCBOP11 force constants (solid line). Experimental data are from inelastic x-ray scattering (squares from [35] and circles from [39]) and electron energy loss spectroscopy (diamonds from [41] and triangles from [40]).

Table 3.2: Graphene phonon frequencies at high symmetry points in  $\text{cm}^{-1}$ . Experimental results are also listed.

Mode	$\Gamma$		M		K	
	LCBOPII	Exp.	LCBOPII	Exp.	LCBOPII	Exp.
ZA	0		265	471 <sup>a</sup> , 465 <sup>b</sup> , 451 <sup>d</sup> , 485 <sup>g</sup>	405	482 <sup>d</sup> , 517 <sup>d</sup> , 530 <sup>e</sup> , 540 <sup>g</sup>
TA	0		713	630 <sup>d</sup> , 631 <sup>g</sup>	1033	1010 <sup>g</sup>
LA	0		1282	1290 <sup>c</sup>	1153	1184 <sup>c</sup> , 1202 <sup>c</sup>
ZO	797	861 <sup>b</sup> , 868 <sup>g</sup>	540	670 <sup>b</sup> , 631 <sup>g</sup>	405	588 <sup>d</sup> , 627 <sup>e</sup> , 540 <sup>g</sup>
LO	1563	1590 <sup>b</sup> , 1575 <sup>f</sup>	1290	1321 <sup>c</sup>	1153	1184 <sup>c</sup> , 1202 <sup>c</sup>
TO	1563	1590 <sup>b</sup> , 1575 <sup>f</sup>	1441	1388 <sup>c</sup> , 1389 <sup>b</sup>	1513	1313 <sup>d</sup> , 1291 <sup>e</sup>

<sup>a</sup> Reference [42].

<sup>b</sup> Reference [41].

<sup>c</sup> Reference [35].

<sup>d</sup> Reference [43].

<sup>e</sup> Reference [40].

<sup>f</sup> Reference [44].

<sup>g</sup> Reference [39].

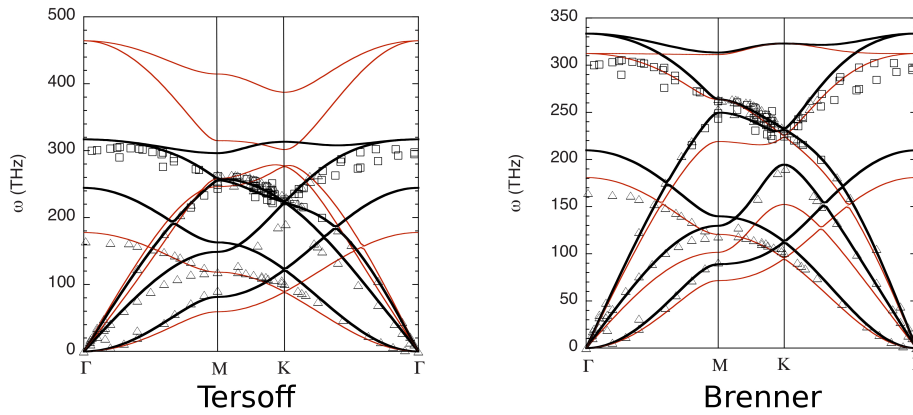


Figure 3.6: Phonon dispersion of graphene calculated from the Tersoff [25] and Brenner [26] empirical potentials published by Lindsay and Broido [45]. The thin (red) lines show the phonon dispersions for the original parameter sets. The thick (black) lines are the phonon dispersions obtained by optimizing these parameters to reproduce the experimental values.

The in-plane acoustic TA and LA modes show a very good agreement with the measurements. The only deviation occurs at the  $M$ -point for the TA branch. At this point however, there is also disagreement between the experimental results. Energy electron loss spectroscopy (EELS) by [41] shows much higher frequencies than the inelastic  $x$ -ray scattering results by [39]. *Ab initio* calculations however seem to be in favour of the latter ([14, 36]) and have suggested that the experiments of [41] are unreliable because EELS selection rules state that the TA mode should be unobservable along the  $\Gamma - M$  line [36]. Their measurement may therefore have been performed on samples of poor quality making them unreliable.

The slopes of the TA and LA branches near the  $\Gamma$ -point both show a good agreement with the experiments, these slopes also determine the sound velocities, which are shown in table 3.3. They are in good agreement with the experimental values from [46] which are again for graphite, but since they are for the in-plane phonon modes they are very similar to those of graphene.

Table 3.3: Sound velocities in of the TA and LA branch of graphene determined by LCBOPII. Experimental values are also given.

Mode	Sound velocity (km/s)	
	LCBOPII	Exp.
TA	13.0	12.3 <sup>a</sup>
LA	20.7	21.0 <sup>a</sup>

<sup>a</sup> Reference [46].

### Force constants of graphene

In the previous section we have calculated the phonon dispersion of graphene from a force constant model based on the LCBOPII potential. The overall agreement with *ab initio* calculations and experimental results are surprisingly good for an empirical potential, as discussed in the previous section. It is interesting however, to take a closer look at the force constants from the LCBOPII potential because they can provide more insight into the discrepancies between our results and the experiments.

In table 3.4 the force constants are listed up to fifth nearest neighbours. The positions of the neighbouring atoms in a graphene sheet are shown in figure 3.3. The force constants are listed in three orthogonal directions. The stretching, ( $\phi_{st}$ ), direction is the direction along the bond, the in-plane, ( $\phi_{ip}$ ), direction is

perpendicular to the stretching direction and in the plane of the graphene sheet, the out-of-plane, ( $\phi_{op}$ ), direction is the force constant corresponding to displacements perpendicular to the graphene sheet, in the  $z$ -direction.

In our software we calculate the force constants  $\phi_{\alpha\beta}(lk, l'k')$  along three Cartesian axes. As can be seen from figure 3.3, the stretching, in-plane and out-of-plane directions coincide with the Cartesian axes (the coordinate system is defined in section 1.2.1) for the first nearest neighbour below the central atom. For the fourth nearest neighbours there is no atom for which the Cartesian axes coincide with the bond directions so we had to apply a rotation to the force constant matrix about the  $z$ -axis through the central atom. Also listed in table 3.4 are the values of the force constants for graphite obtained by Mohr et al. [39] by fitting a force constant model to their experimental data from inelastic x-ray scattering. Since the van der Waals interaction between the layers in graphite are very weak the phonon dispersion relations of graphite and graphene are almost degenerate and the intralayer force constants of graphite will be identical to those of graphene.

Table 3.4: Force constants in  $\text{eV}/\text{\AA}^2$  based on LCBOPII. The stretching column contains the force constant along the bond direction, the in plane constant direction is perpendicular to the bond in the plane of the sheet.

# Neighbour (distance)	Stretch		In-plane			Out-of-plane			
	LCBOPII	Mohr[39]	LCBOPII	Mohr[39]		LCBOPII	Mohr[39]		
1 (1.42 \AA)	$\phi_{st}^1$	26.60	25.880	$\phi_{ip}^1$	8.99	8.420	$\phi_{op}^1$	4.73	6.183
2 (2.46 \AA)	$\phi_{st}^2$	3.37	4.037	$\phi_{ip}^2$	-0.61	-3.044	$\phi_{op}^2$	-0.75	-0.492
3 (2.84 \AA)	$\phi_{st}^3$	0.51	-3.016	$\phi_{ip}^3$	-0.05	3.948	$\phi_{op}^3$	-0.05	0.516
4 (3.76 \AA)	$\phi_{st}^4$	0.02	0.564	$\phi_{ip}^4$	0.00	0.129	$\phi_{op}^4$	0.00	-0.521
5 (4.26 \AA)	$\phi_{st}^5$	0.00	1.035	$\phi_{ip}^5$	0.00	0.110	$\phi_{op}^5$	0.00	0.166

Looking at the force constants in table 3.4 we see that our force constants between the first nearest neighbours are very similar to the fitted force constants from Mohr et al. For second and higher order neighbours however the correspondence between our force constants and the fitted values goes from bad to worse. While the stretching constant between second nearest neighbours differs by 17%, which can still be considered acceptable, the in-plane constants have a difference of 80% which is by no means comparable. Differences between further away neighbours are all incomparable and the general trend is that our force constants drop to zero with increasing distance a lot faster than the fitted constants.

It must be noted however that the force constants from Mohr et al. originate from the fit of an over-simplified model to experimental data and are thus not guaranteed to correspond to the actual force constants. The main assumption their model makes is that the force constant matrix is always diagonal in the Cartesian coordinate system with axes coinciding with the stretching, in-plane and out-of-plane directions. Since they include up to fifth nearest neighbours this leaves them with 15 parameters to fit. The general form of the  $3 \times 3$  force constant matrix between  $n$ -th nearest neighbours of graphene however, is the following:

$$\begin{pmatrix} \phi_{st}^n & \phi_{od}^n & 0 \\ -\phi_{od}^n & \phi_{ip}^n & 0 \\ 0 & 0 & \phi_{op}^n \end{pmatrix}. \quad (3.41)$$

The out-of-plane displacements are completely decoupled from the in-plane displacements as a direct consequence of the reflection symmetry  $\sigma_z$  in the graphene sheet. The off-diagonal terms, the  $\phi_{od}$ 's, are not included in the model of Mohr et al. But upon taking a closer look at the symmetries of the hexagonal lattice in figure 3.3 one can see that this is indeed true for the first, third and fifth neighbours but not for the second and fourth neighbours. The off-diagonal force constants given by LCBOPII are shown in table 3.5. As expected the first, third and fifth neighbours have a zero off-diagonal force constant. The fourth neighbour has a nonzero value but its magnitude is only of the order of  $10^{-6} \text{ eV}/\text{\AA}^2$ . The second neighbours have a force constant of  $1.48 \text{ eV}/\text{\AA}^2$  which is certainly not negligible compared to

Table 3.5: Off-diagonal force constants for graphene as predicted by LCBOPII

# Neighbour	$\phi_{od}$ (eV/Å <sup>2</sup> )
1 (1.42 Å)	0.00
2 (2.46 Å)	1.48
3 (2.84 Å)	0.00
4 (3.76 Å)	$\mathcal{O}(10^{-6})$
5 (4.26 Å)	0.00

the other force constants between second nearest neighbours. The simplified model used by Mohr et al. might explain the differences on the second level of neighbours between LCBOPII and fitted force constants but the fact remains that our force constants fall off very fast compared to all other studies we have compared to ([2, 36, 39]). Since the short-range part of the LCBOPII potential is active up to 2.2 Å, these force constants are mainly determined by the long-range part of the LCBOPII potential<sup>4</sup> (see section 1.5) which does not have the environment dependence which the short-range part has. Instead, it is a smoothly varying Morse function which does not have large second derivatives and thus cannot yield large force constants.

The long-range force constants are important for the dispersion relation of the higher frequency (more than 400 cm<sup>-1</sup>) modes (see [39] and [36]). It is known that a good fit to the high frequency regime of the experimental data requires at least a fourth nearest neighbour force constant model with inclusion of the off-diagonal constant between second neighbours or a fifth nearest neighbour force constant model without the inclusion of off-diagonal constants [47]. In view of this it is not surprising that our own phonon dispersion shows the biggest differences with experiments at high frequencies because our force constants are practically equal to zero beyond third nearest neighbours.

### Modification of in-plane force constants

Even though our potential does not provide them, it is interesting to see how the phonon dispersion evolves if we manually change the force constants from 2<sup>nd</sup> neighbours and beyond to match those of Mohr et al. This is relatively easy to do, because, once the stretching, in-plane and out-of-plane constants are known, the force constant matrices between one of the two atoms in the graphene unit cell and their respective neighbours can be calculated in the Cartesian coordinate system by performing the appropriate rotations of the diagonalized matrix (which has the form of equation (3.41)). Because the model of Mohr et al. does not have any off-diagonal constants we also set these to zero by hand. The force constants between first nearest neighbours, as well as the  $\phi_{op}$ 's, belonging to the out-of-plane displacements are kept at their original LCBOPII values. In figure 3.7 the resulting phonon dispersions are shown for different levels of modified neighbours.

From figure 3.7 we see that changing the second nearest neighbour force constants already improves the dispersion in the high frequency regime. The problematic TO mode is lowered in frequency and the splitting between TO and LO branches along the  $\Gamma - K$  and  $\Gamma - M$  becomes larger. The frequencies at  $\Gamma$  remain practically the same and, as expected, the out-of-plane ZA and ZO branches do not change at all. Another effect of the modification is that the crossing of the ZO and TA branches changes from the  $\Gamma - M$ , to the  $M - K$  interval and the gap between them at the  $M$  point becomes smaller. This makes the dispersion more like the *ab initio* calculations but the good agreement between our TA branch and the measurements by Oshima et. al [41] disappears. These experimental results however have been questioned as discussed in the previous section. Another consequence is that the sound velocity of the TA mode becomes much lower than the LCBOPII value which was in good agreement with observations. Finally the frequency of the TA branch at the  $K$  points gets lowered from 1033 cm<sup>-1</sup> to 843 cm<sup>-1</sup> which is

<sup>4</sup>The short range potential is cut off at 2.2 Å but still has a small effect on the force constants between second nearest neighbours (separated by 2.46 Å). For third nearest neighbours and beyond the short range potential has no influence on the force constants.

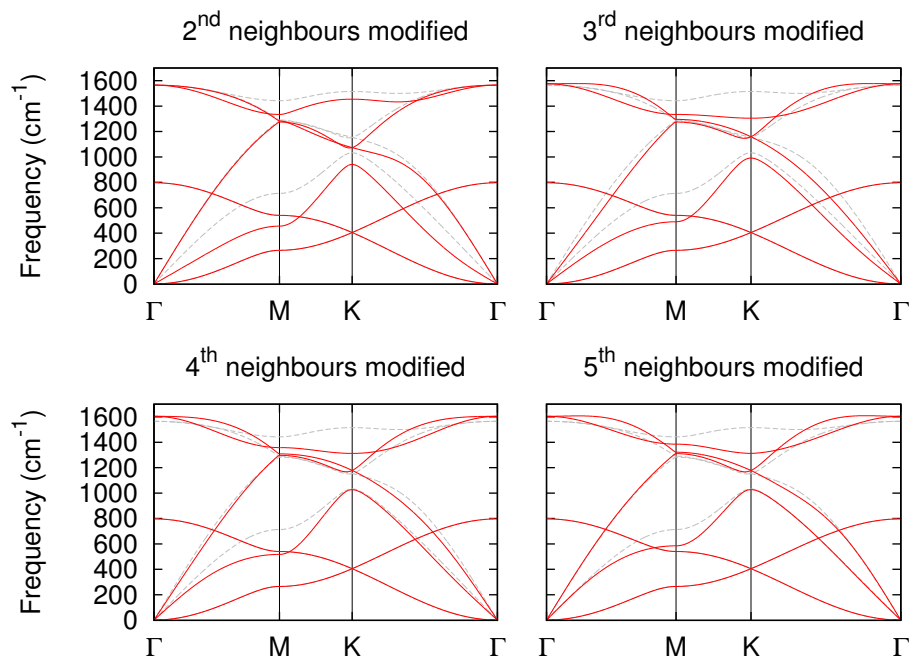


Figure 3.7: Graphene phonon dispersion with the in-plane force constants from second up to the indicated level changed to those from the fit of Mohr et al. [39], listed in table 3.4. The resulting dispersion is the red (solid) line, the original LCBOPII dispersion is the gray (dashed) line.

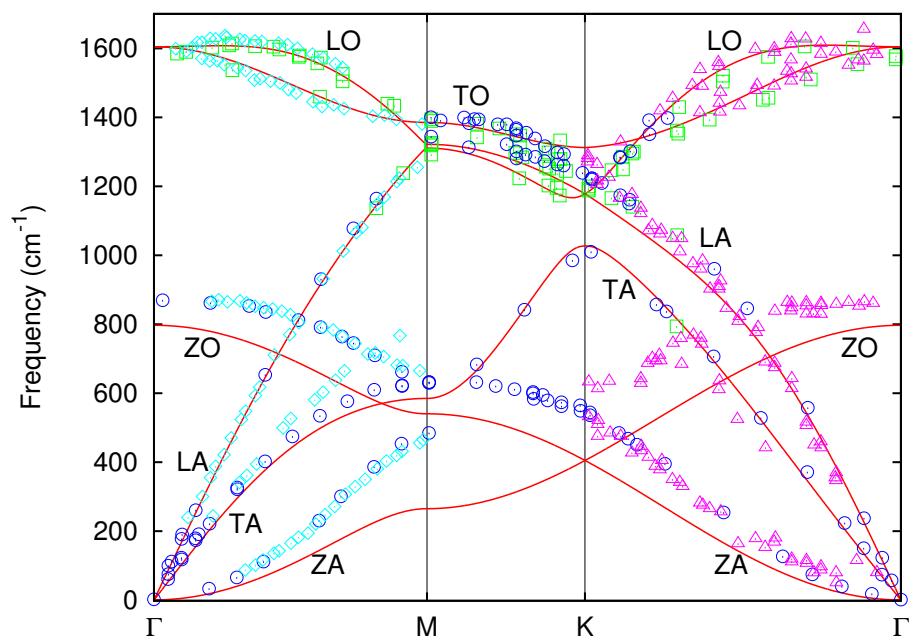


Figure 3.8: Graphene phonon dispersion with the in-plane force constants from 2<sup>nd</sup> to 5<sup>th</sup> nearest neighbours modified to match the fit of [39]. Experimental data is also shown in the same symbols as figure 3.5.

much further from the experimental value of  $1016 \text{ cm}^{-1}$  [39].

Changing the third and fourth nearest neighbour force constants lowers the energy of the TO mode along  $M - K$  even further and the gaps between the TO and LO branches along  $\Gamma - K$  and  $\Gamma - M$  become larger. The crossing of the ZO/TA branches moves closer to the  $M$  point and, the value of the TA branch at the  $K$  point increases back to about the original LCBOPII value. At the zone center itself we also note an increase in the frequencies of the TO and LO modes to  $1604 \text{ cm}^{-1}$  making the correspondence with experiment ( $1590 \text{ cm}^{-1}$  according to [41] and  $1588 \text{ cm}^{-1}$  according to [39]) slightly better.

Finally we also modified the fifth nearest neighbour force constants and obtained the final phonon dispersion shown in figure 3.7 and in figure 3.8, together with the experimental values. Here we see for the first time the overbending effect, the highest frequency does not occur at the zone center but slightly away from it in the LO mode. The sound velocities are almost the same as we found originally and the frequencies at  $\Gamma$  remain the same as in the previous modification. The crossing between the TA and ZO modes shifts again to a point along the  $\Gamma - M$  line but the splitting between the two at the  $M$  point is still much smaller than the gap in our original dispersion. Clearly the high frequency part is greatly improved compared to the original dispersion in figure 3.5. The two out-of-plane modes have not changed because we only modified the in-plane force constants.

### Modification of out-of-plane force constants

Until now we have left the out of-plane-force constants at their original values, thus leaving the ZA and ZO branches unchanged. These branches however also differ significantly from the experimental values. The frequencies predicted by LCBOPII are too soft compared to the experimental results which indicates that our force constants are too small. The quadratic behaviour of the ZA mode close to the zone center is reproduced well by LCBOPII. Physically, this is a very important characteristic because the phonon energies of quadratic modes will remain low for a larger number of wavevectors than for the linear modes. The result is that the ZA branch will have a lot of influence on the behaviour of the system at low temperatures. In particular, it determines the value of the bending rigidity which will be discussed in section 3.3.

Now, we will modify the out-of-plane force constants,  $\phi_{op}^n$ , to see how they affect the frequencies of the ZA and ZO mode. Rather than using the out-of-plane force constants obtained by Mohr et al. [39] we will use those obtained by Tewary et al. [47] which are listed in table 3.6. They were obtained in a similar manner as those from Mohr et al., namely by fitting a model to the experimental graphite dispersion. The reason that we use these force constants, instead of those from Mohr et al. is that Tewary et al. have included interactions only up to fourth nearest neighbours, making the force constants naturally more resemblant to our own.

Table 3.6: Out-of-plane force constants in  $\text{eV}/\text{\AA}^2$  as calculated from the empirical potential of Tewary et al. [47]. LCBOPII values are also listed for easy comparison.

# Neighbour	Out-of-plane		
		LCBOPII	Tewary [47]
1 (1.42 \AA)	$\phi_{op}^1$	4.73	6.17
2 (2.46 \AA)	$\phi_{op}^2$	-0.75	-0.511
3 (2.84 \AA)	$\phi_{op}^3$	-0.05	0.362
4 (3.76 \AA)	$\phi_{op}^4$	0.00	-0.325

The phonon frequencies obtained when changing the out-of-plane force constants for different neighbour levers are shown in figure 3.9. The increase in  $\phi_{op}^1$  increases the phonon frequencies by about  $100 \text{ cm}^{-1}$  which improves the correspondence with experimental values considerably. The quadratic behaviour of the ZA mode at low  $|q|$  however is almost completely lost. The quadratic dispersion is not recovered by changing the second and third neighbour force constants. These modifications shifts the frequencies up a bit more but have little effect on the overall shape of the out-of-plane modes. Changing

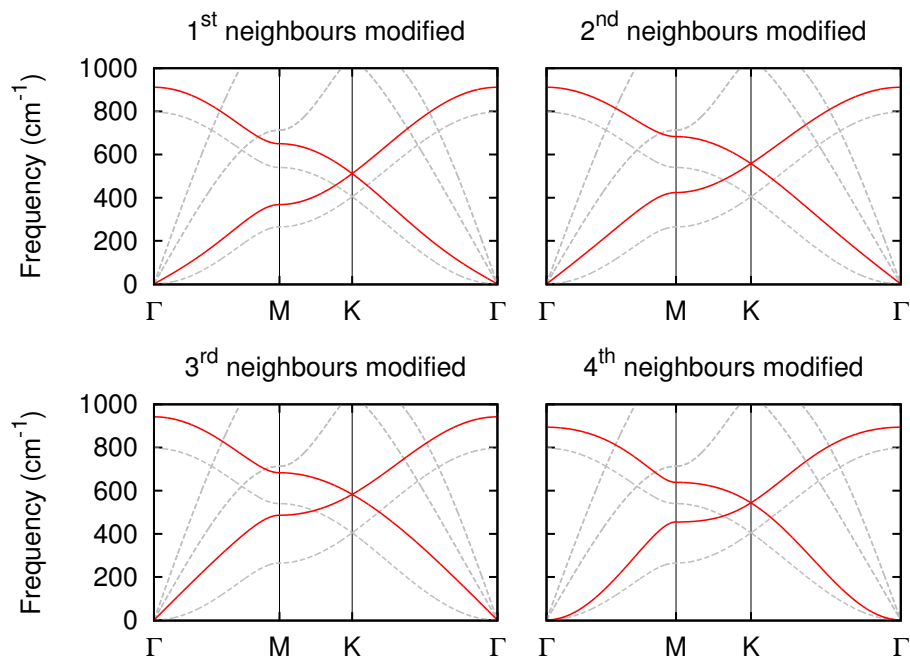


Figure 3.9: Phonon dispersion of graphene with the out-of-plane force constants changed to match those from the fit by Tewary et al. [47]. The red (solid) lines are the out-of-plane modes, which are modified by the changes. Original LCBOP11 frequencies are the gray (dashed) lines.

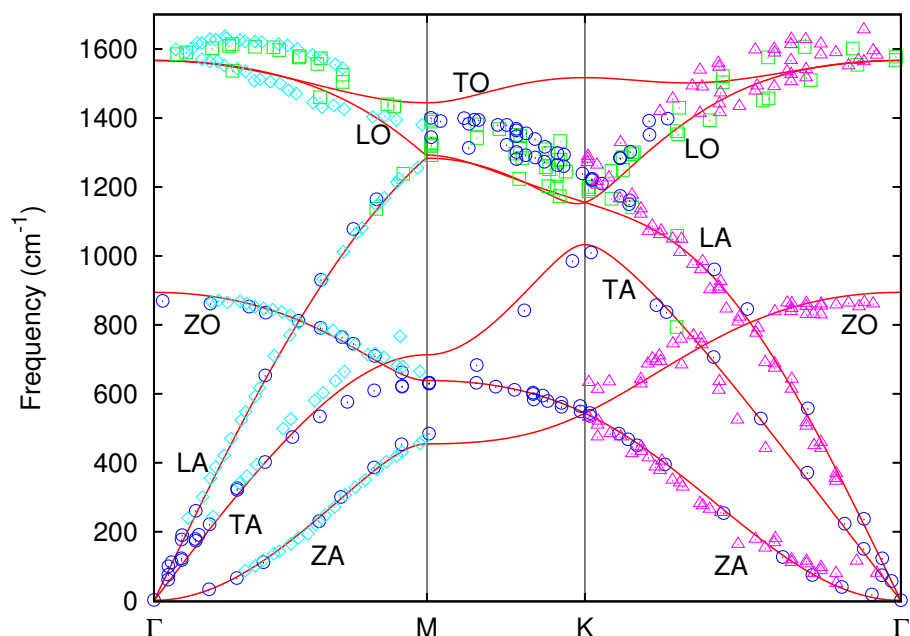


Figure 3.10: Graphene phonon dispersion with the out-of-plane force constants modified to match those from [47]. The in-plane force constants are the LCBOP11 values. Experimental data for graphite is shown in the same symbols as figure 3.5.

the fourth out-of-plane force constant,  $\phi_{op}^4$ , from 0.00 to  $-0.325 \text{ eV}/\text{\AA}^2$  reintroduces the quadratic dispersion of the ZA mode and lowers the frequencies at the  $\Gamma$ ,  $M$  and  $K$  points. The final dispersion is shown with the experimental data in figure 3.10.

By doing these modifications we have of course left our assumption that carbon-carbon interactions are well described by the LCBOPII potential. We have shown however that, for the in-plane modes, it is possible to obtain a much better agreement with experimental data by only modifying the force constants beyond nearest neighbours. In the language of LCBOPII (see 1.5) this means that we have only changed those force constants that are mainly determined by the long-range part of the potential  $V_{ij}^l$ . Consequently it may be possible to improve the LCBOPII potential by only changing the long range interactions and leaving the short range potential, responsible for the good force constants between first nearest neighbours, unchanged. In any case, the phonon spectrum of graphene provides a good test of both the short, and the long-range interactions of the empirical potential. Since a lot of experimental data is available it is an interesting system to use in the process of fitting the parameters of future version of LCBOPII.

### 3.2.3 Graphite

In this section we will cover the phonon dispersion curves of graphite. The unit cell and Brillouin zone of the crystal have been discussed in section 1.3.1. Since the ABABAB (Bernal) stacking of the graphene layers has the lowest cohesive energy and is by far the most naturally abundant type of graphite we will refer to this type simply by graphite. If other stacking forms are described it will be explicitly mentioned.

#### Calculations and results

To calculate the force constants we used a supercell of approximately  $17 \text{\AA} \times 21 \text{\AA} \times 20 \text{\AA}$  containing 840 carbon atoms, in six layers, with periodic boundary conditions in all three directions. The total energy of the crystal is at a minimum when the carbon-carbon distance is  $a_{CC} = a/\sqrt{3} = 1.4194 \text{\AA}$  and the distance between the layers is  $d = c/2 = 3.3672 \text{\AA}$ . In this configuration, every atom has an energy of  $-7.3653 \text{ eV}$ . These parameters give a  $c/a$  ratio (see section 1.3.1 for definition) of 2.739 which is in good agreement with the experimental value of 2.725 [39, 48, 49].

The phonon dispersion thus obtained is shown in figure 3.11 along the high symmetry directions in the Brillouin zone. Graphite has four atoms per unit cell (2 per layer) giving twelve separate phonon branches, but as can be seen from figure 3.11, most branches are almost doubly degenerate and show a very close resemblance to those of graphene. This is because the normal modes of graphite are the same as for graphene but every branch splits into two branches corresponding to identical atoms in the two different layers moving either in-phase or out-of-phase with respect to each other (these out-of-phase modes are denoted by  $O'$  in the branch name). But since the interlayer interaction is very weak this splitting has barely any effect on the frequencies. The one exception is the low frequency ZA branch which splits into the ZA and the  $ZO'$  branch where the layers oscillate as rigid plates, completely out-of-phase with each other in the  $z$ -direction. To see just how similar the dispersions of graphite and graphene really are both have been plotted together in figure 3.12. Only the out-of-plane branches show a significant difference, the branches of graphene are about 5 to  $10 \text{ cm}^{-1}$  lower than those of graphite. This is because atoms in graphene can move more freely in the  $z$ -direction since they are not hindered by atoms in other layers.

Of course, the three-dimensional structure of graphite also allows for phonons with wavevectors perpendicular to graphene planes (the  $\Gamma - A$  direction in figure 3.11). The high frequency modes have very flat dispersions along this line. The lower modes are more interesting and they are shown in figure 3.13 along with the experimental data available. The frequencies at  $A$  are also listed in table 3.7. We should realize, that due to the different direction of the wavevector, the longitudinal modes now correspond to out-of-plane vibrations and the transverse modes to in-plane movement of the atoms. The transverse branches are both doubly degenerate due to the two independent but equivalent directions in the layers. The shape of the dispersion curves is in agreement with the experiments but the transverse branches are too soft. These branches include the shearing motion of the graphene planes, which is determined by the long-range part of LCBOPII. This motion was not included in the fitting of the potential's parameters and

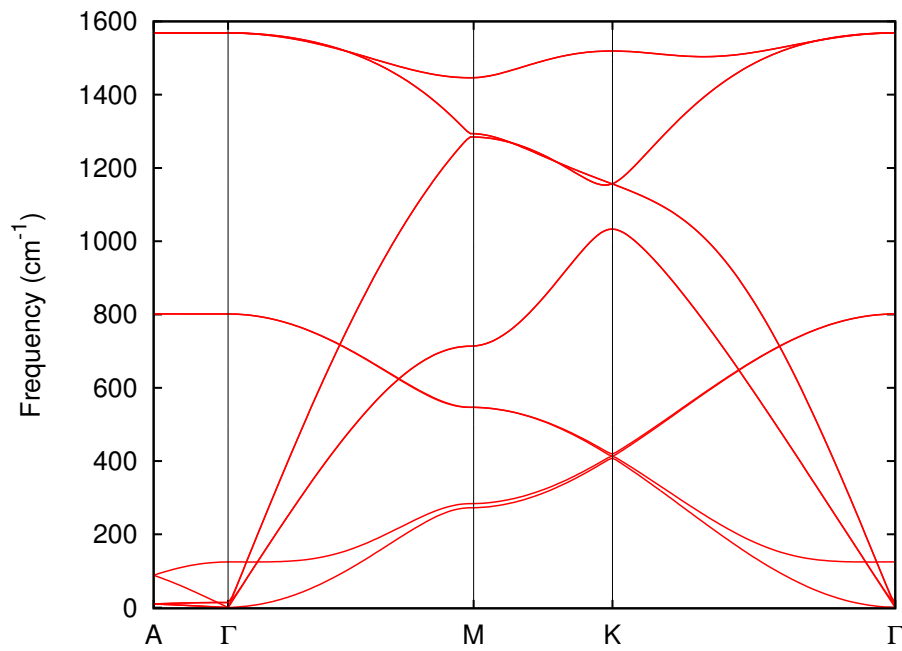


Figure 3.11: Phonon dispersion of graphite in Bernal stacking along the high symmetry lines in the first Brillouin zone.

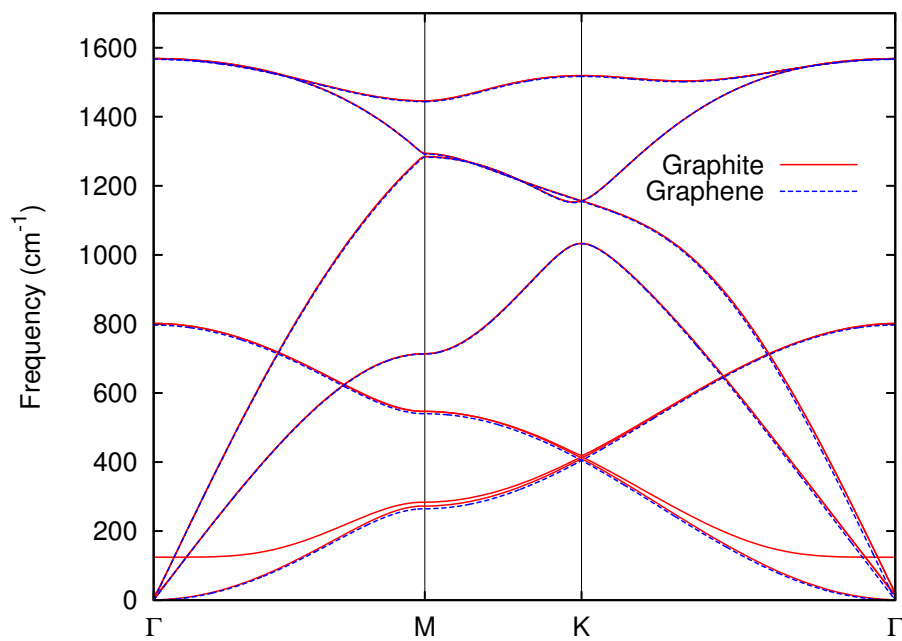


Figure 3.12: In-plane phonon dispersion curves for graphite and graphene from LCBOPIL. They only differ for the low frequency out-of-plane branches.

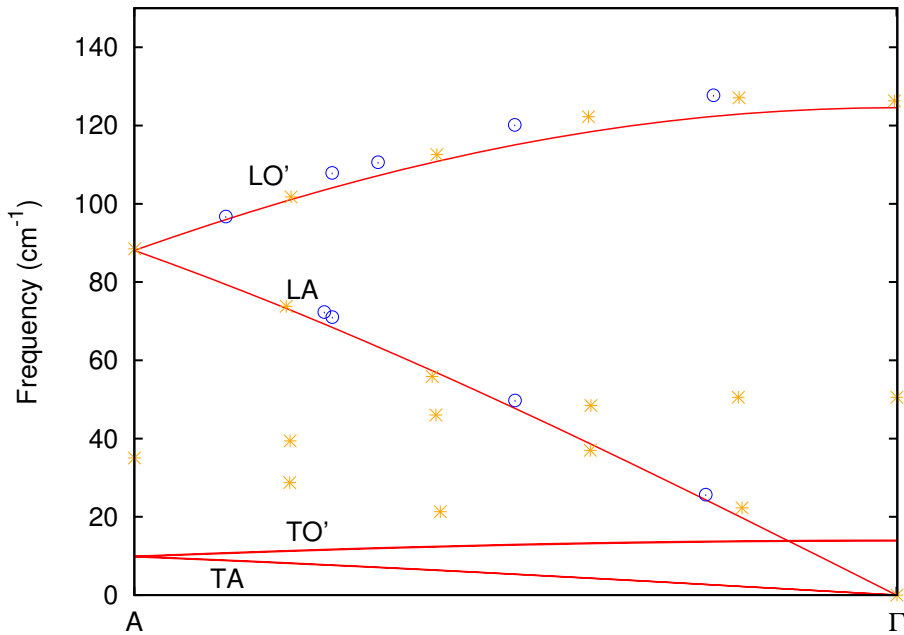


Figure 3.13: Low frequency phonon dispersion of graphite along the  $A - \Gamma$  line together with experimental data. Open circles are inelastic x-ray scattering results from [39], stars are neutron scattering data from [42].

it is known that the energy of this motion is poorly reproduced by LCBOPII. The longitudinal branches on the other hand, are in excellent agreement with the measurements. This however is no surprise realizing that for these modes the planes move as rigid objects so that only the long range interactions play a role and these interactions were fitted to reproduce the elastic constants of graphite accurately [6].

Table 3.7: Graphite phonon frequencies at the  $A$  point together with experimental values if available.

Mode	$A$	
	LCBOPII	Exp.
TA/TO'	10	35 <sup>a</sup>
LA/LO'	88	89 <sup>a</sup>
LO	801	
TO	1568	

<sup>a</sup> Reference [42].

Finally, we also calculate the phonon dispersion for rhombohedral graphite (ABCABC... stacking of the layers). The result is shown in figure 3.14. Since there are now 6 atoms per unit cell there are 18 branches but just as we saw for Bernal stacked graphite most of the branches are (threefold) degenerate and very close to the graphene branches. The three layers in the unit cell result in even more non-degenerate branches in the low frequency dispersion along the  $\Gamma - A$  line. The highest frequency branch in this direction ( $125 \text{ cm}^{-1}$  at  $A$ ) is the mode where all three layers oscillate completely out-of-phase with each other as rigid plates.

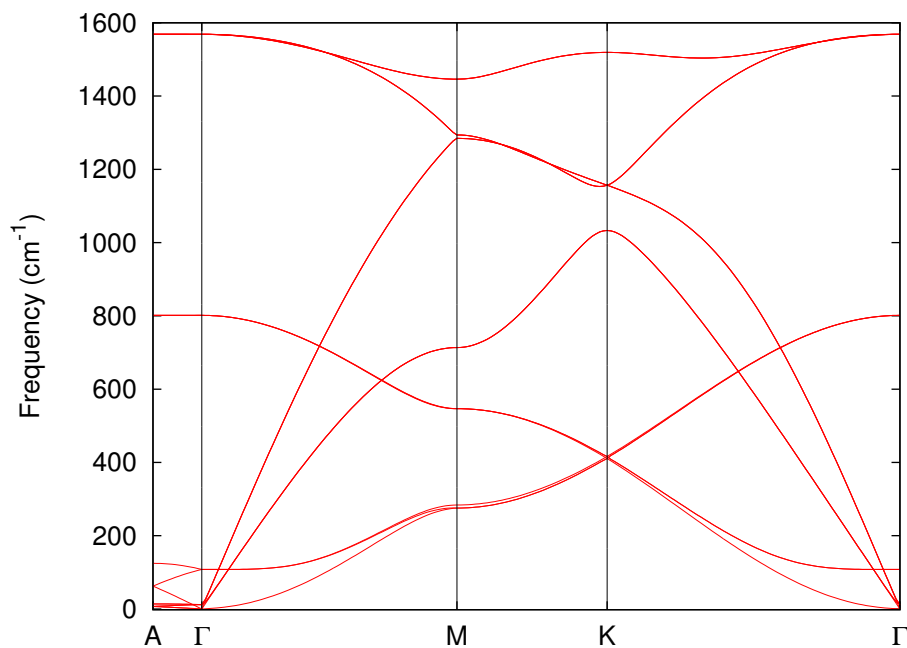


Figure 3.14: Phonon dispersion for rhombohedral (ABCABC... stacking) graphite calculated from LCBOP11.

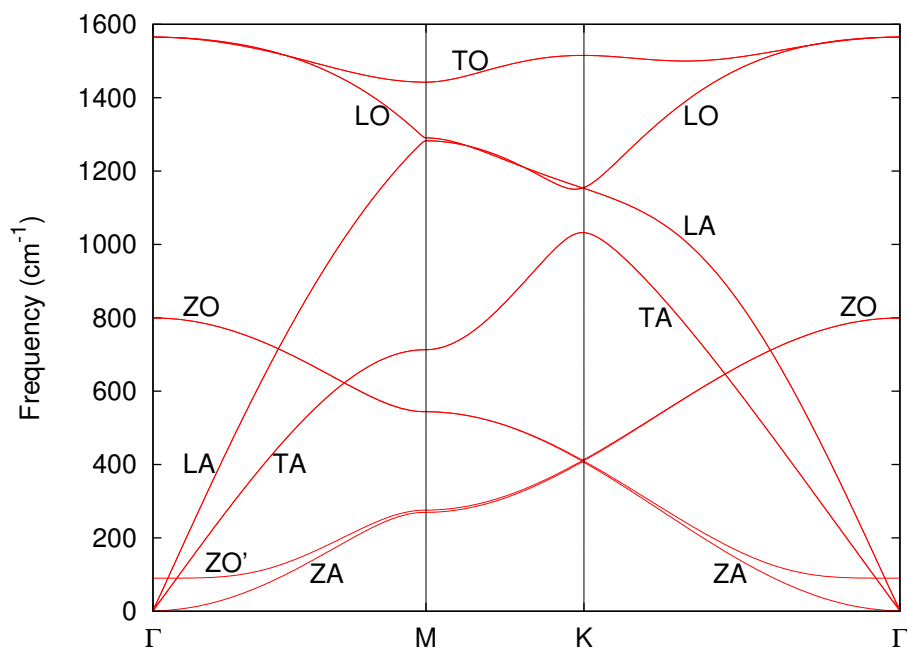


Figure 3.15: Phonon dispersion of bilayer graphene along the high symmetry lines in the Brillouin zone.

### 3.2.4 Bilayer graphene

In recent years not only graphene, but also bilayer graphene has attracted a lot of attention, mainly because of its unique electronic properties, which differ from both single layer graphene and bulk graphite. In this section we will calculate the phonon dispersion of bilayer graphene.

#### Calculations and results

The calculation of the force constants of bilayer graphene was performed on a slab of  $27 \text{ \AA} \times 30 \text{ \AA}$  with periodic boundary conditions in the direction of the plane. The lattice parameters minimizing the total energy are  $a_{CC} = 1.4196 \text{ \AA}$  and  $d = 3.3670 \text{ \AA}$  yielding an energy of  $-7.3628 \text{ eV}$ .

The resulting phonon dispersion is shown in figure 3.15. As we have seen with graphite most of the branches are almost doubly degenerate corresponding to the in-phase and out-of-phase superposition of the graphene modes in the upper and lower layer. Just as for bulk graphite there is an extra low frequency optical primed mode in which the two layers show an out-of-phase breathing motion. This ZO' mode has a frequency of  $90 \text{ cm}^{-1}$  which is in excellent agreement with results from [50] who also report a frequency of  $90 \text{ cm}^{-1}$  based on DFT calculations. This good agreement is again no surprise since the elastic constants between graphite planes which govern this mode were fitted to experimental values.

### 3.2.5 Carbon nanotubes

Since carbon nanotubes are basically just rolled up graphene sheets their phonon dispersion can be obtained by means of zone-folding. This method is explained and applied to (10,10) nanotubes in [2]. The problem with this method is that the effects of the curvature of nanotubes are not taken into account as the force constants from flat graphene are used. Because our method calculates the force constants directly from the total energy of the curved nanotube, curvature effects should be taken into account properly, as long as the LCBOPII potential describes these effect correctly. Just like we have seen in the other systems, SWCNs also have an acoustic mode with a quadratic dispersion relations. This is well known from numerous theoretical papers and numerical studies [15, 37, 38, 51, 52, 53].

#### Calculations and results

We calculate the phonon dispersion of the (10,10) armchair, and the (10,0) zigzag nanotubes. Both types of nanotubes have 40 atoms in their respective unit cells, and thus have 120 separate phonon branches. Due to the symmetry of the nanotubes however, a lot of these branches will be degenerate. The (10,10) nanotube for example effectively has 66 distinct branches of which there are 54 doubly degenerate and 12 are non-degenerate [2].

The force constants were calculated from nanotube structures with minimal energy according to LCBOPII, these were found by scaling the unit cell in the radial and axial direction independently, in order to minimize the cohesive energy. The binding energies of the nanotubes are  $-7.330$  and  $-7.289 \text{ eV/Atom}$  for the (10,10) and (10,0) SWCN respectively. The fact that the value is lower for the armchair nanotube is because its radius is almost twice as large ( $6.78 \text{ \AA}$  versus  $3.91 \text{ \AA}$ ) which means that it has a much lower energy penalty due to the curvature of the graphene sheet.

The calculated phonon dispersions are shown in figure 3.16. The frequencies are calculated along the  $\Gamma - X$  line (see section 1.4.1 for definition), which is half of the first Brillouin zone. These dispersions compare well to the *ab initio* results from Dubay and Kresse [37]. In the low frequency region we see for both nanotubes (see figure 3.17 for a zoom of the dispersion of the (10,10) nanotube) that there are four acoustic modes. There are two linear modes and two, degenerate, quadratic modes. The fact that nanotubes have four acoustic modes, instead of the usual three, is a consequence of the cylindrical symmetry. In addition to the three translational degrees of freedom, nanotubes have an additional rotational symmetry around the nanotube axis. This symmetry results in a phonon mode which twists the nanotube along its axis. At the zone center, this twisting (or torsional) mode becomes a simple rotation which means that it has zero frequency. The longitudinal LA mode, with atom displacements in the  $z$ -direction, is the highest acoustic mode at low  $q$ . The doubly degenerate TA modes correspond to the bending of the nanotube in

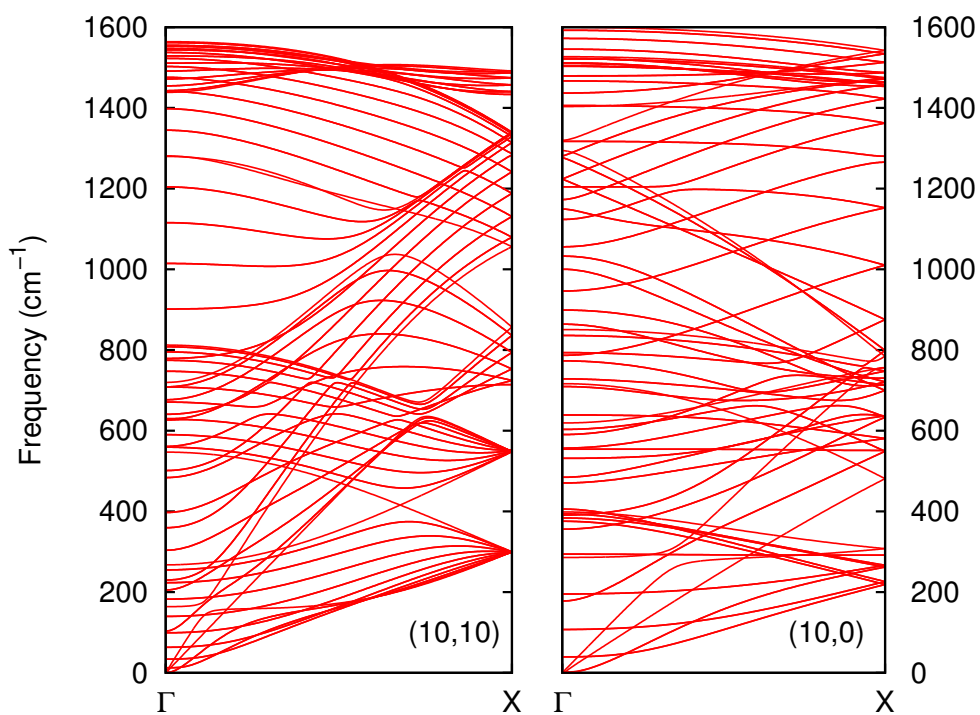


Figure 3.16: Phonon dispersions of the armchair (10,10) tube (left) and the zigzag (10,0) nanotube (right) calculated by LCBOPII.

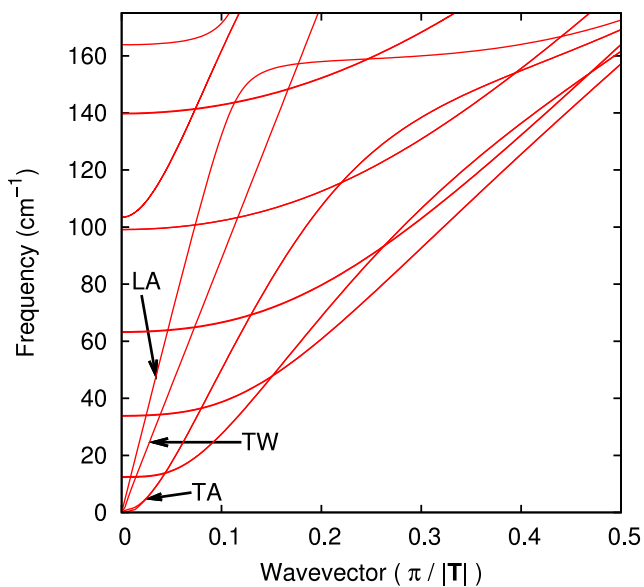


Figure 3.17: Low frequency phonon dispersion of the (10,10) nanotube. The quadratic TA bending mode is doubly degenerate. The TW mode corresponds to the twisting motion of the nanotube along its axis.

two orthogonal directions. These modes are the low frequency modes which are the main contributors to thermal contraction at low temperatures, as explained in chapter 2.

### 3.3 Bending rigidity

The quadratic dispersion of the ZA phonon mode is a characteristic feature of the layered crystals we have considered until now. The coefficient relating  $\omega(\mathbf{q})$  and  $|\mathbf{q}|^2$  determines the bending rigidity,  $\kappa$ , of the crystal. This constant is a measure of the amount of energy that is needed to bend the layers of the crystal. It has been shown by Lifshitz [54] that the dispersion of the ZA branch for graphite, for small wavevectors is given by

$$\omega(\mathbf{q}) = \sqrt{\frac{C_{44}}{\rho} |\mathbf{q}|^2 + \frac{\kappa}{\rho c} |\mathbf{q}|^4}, \quad (3.42)$$

where  $\kappa$  is the bending rigidity,  $C_{44}$  is an elastic constant related to the shearing motion of the graphite planes (see [33, chap. 3]),  $\rho$  is the mass density, and  $c$  is the unit cell height for AB stacked graphite as defined in section 1.3.1. At very low  $|\mathbf{q}|$ ,  $\omega$  will grow linearly due to the term with  $C_{44}$ . But as we shall see, the term including the bending rigidity  $\kappa$  quickly dominates the dispersion at larger  $|\mathbf{q}|$ .

The values that have been reported for the bending rigidity of graphene and graphite differ a lot. Also, experimental data for graphite is often used to determine the bending rigidity of graphene while it is not evident that this is allowed. Even though the van der Waals interactions between the layers in graphite are very weak, it is precisely at the out-of-plane modes that they have the largest effect, as shown in figure 3.12. Intuitively one would expect the bending rigidity to be slightly higher for graphite than for graphene since the layers can move less freely in graphite. Furthermore, the linear term appearing in the dispersion relation (3.42) relation of graphite is not present in the dispersion of the ZA mode for graphene [47, 55]. The bending mode dispersion for graphene is thus purely quadratic and takes the following form [47]:

$$\omega(\mathbf{q}) = \sqrt{\frac{\kappa}{\rho}} |\mathbf{q}|^2, \quad (3.43)$$

where  $\rho$  is now a two-dimensional mass density. An often cited value of  $\kappa$  for graphene is 1.2 eV. It was extracted from the phonon dispersion of graphite, as reported by Tersoff [56]. In the same paper a value of 1.02 eV is calculated from the relation between the cohesive energy and curvature of carbon nanotubes. These calculations were performed based on the Tersoff empirical potential [25]. A few studies have determined  $\kappa$  for graphene based on empirical potentials which were especially designed to reproduce the experimentally measured phonon spectrum of graphite. The first of these, [55], report a  $\kappa$  of 2.1 eV. The second paper, by Tewary and Yang [47], determines a value of 2.13 eV based on the force constants from a modified Tersoff-Brenner potential [26]. They calculate the bending rigidity directly from the out-of-plane force constants by a formula derived in [57]:

$$\kappa = -\frac{\sqrt{3}a^2}{144} \left( \phi_{op}^1 + 18\phi_{op}^2 + 16\phi_{op}^3 + 98\phi_{op}^4 + 162\phi_{op}^5 \right). \quad (3.44)$$

Using the same method, this paper also reports a value of  $\kappa = 0.797$  eV for the original Tersoff-Brenner potential. Finally, Fasolino et al. report a value of 0.82 eV for graphene based on total energy calculations from the LCBOPII potential [5]. But perhaps more important than this value itself is their finding that the bending rigidity is not really a constant, but rather increases with increasing temperature. This behaviour was found by studying the normal-normal correlation function in graphene samples from Monte Carlo simulations. From absolute zero to room temperature, the bending rigidity increases from 0.82 to about 1.1 eV. This helps explain why the values of  $\kappa$  obtained from experimental data of the graphite phonon dispersion (which are taken at room temperature) are higher than the values predicted from empirical potentials which are evaluated at 0 K.

Another reason for the large differences in the values for  $\kappa$  may lie in the definition of  $\kappa$  itself. One has to realize that the  $\kappa$  appearing in equations (3.42) and (3.43) are the bending rigidities corresponding to the unit cell of either graphene or graphite. Since graphite has two layers of graphene in its unit cell the bending rigidity of graphite will be roughly twice that of graphene, assuming that the interlayer

interactions have a small effect. To illustrate this further we consider the coefficients of the quadratic terms in the dispersions of graphite and graphene. For clarity we will denote the bending rigidity of graphite from (3.42) by  $\kappa_{bulk}$  and the one for the single layer from equation (3.43) by  $\kappa_{SL}$ . The coefficient for graphite is

$$\frac{\kappa_{bulk}}{\rho c} = \frac{\kappa_{bulk}}{c} \frac{V_c}{Nm_c} = \frac{\kappa_{bulk}}{c} \frac{\frac{1}{2}3\sqrt{3}a_{CC}^2 c}{4m_c} = \frac{\kappa_{bulk}3\sqrt{3}a_{CC}^2}{8m_c}. \quad (3.45)$$

The coefficient for graphene, from equation (3.43), is the following:

$$\frac{\kappa_{SL}}{\rho} = \kappa_{SL} \frac{A_c}{Nm_c} = \kappa_{SL} \frac{\frac{1}{2}3\sqrt{3}a_{CC}^2}{2m_c} = \frac{\kappa_{SL}3\sqrt{3}a_{CC}^2}{4m_c}. \quad (3.46)$$

These two coefficients are of course not exactly equal, due to the weak interlayer interactions, but it is clear from figure 3.12 that they cannot differ much. But, by comparing equations (3.45) and (3.46), we see that there is a factor two difference between the two expressions. From this we can conclude that  $\kappa_{bulk} \approx 2\kappa_{SL}$ . It is thus more insightful to talk about the bending rigidity *per layer*, and this is how we will define  $\kappa$  in the remainder of this thesis. This factor two might also explain the large differences in the values reported by other studies. The values of 2.1 and 2.13 eV would imply a  $\kappa$  of about 1.05 eV per layer which is consistent with the other values obtained from room temperature observations.

We have mentioned several techniques to calculate the bending rigidities of graphene and graphite. Now we will employ three of these techniques to determine the bending rigidity ourselves. The first is the determination of  $\kappa$  by directly fitting the formulas (3.42) and (3.43) to the calculated dispersion of the ZA modes. The second approach is a direct total energy calculation of zigzag carbon nanotubes of varying radius and the third is the usage of equation (3.44). A fourth method, that can extract  $\kappa$  from normal-normal correlation functions, used in [58] will complement the results. Results from all three methods are summarized in table 3.8.

Table 3.8: Bending rigidities obtained from the LCBOPII potential through different methods.

Method	$\kappa$ (eV)
Graphene ZA mode, eq (3.43)	$0.69 \pm 0.02$
Graphite ZA mode, eq (3.42)	$0.69 \pm 0.01$
Nanotube curvature, eq (3.47)	0.69
Graphene force constants, eq (3.46)	0.70

### Bending rigidity calculations from the acoustic out-of-plane phonon branch

The acoustic ZA branch of graphene has a purely quadratic dispersion given by equation (3.43). We have fitted this equation to the phonon dispersion of the ZA mode. The resulting value for the bending rigidity is  $0.69 \pm 0.02$  eV.

The fit was calculated along the  $\Gamma - M$  line of the phonon spectrum, but we have checked that we obtain the same results when fitting the phonon dispersion to the  $\Gamma - K$  line. Since equation (3.43) is only valid for low  $|q|$  we had to decide up to what value of  $|q|$  to fit the equation. We found that a maximum wavevector in the range of 0.2 to 0.4  $\text{\AA}^{-1}$  gives good quality fits and a relatively small error of 0.02 eV in the resulting value for  $\kappa$ . To see how this maximum value of  $|q|$  compares to other results we plotted equation (3.42) in figure 3.18 with  $\kappa = 1.06$  eV per layer (as found by [47]) and  $C_{44} = 4.5$  GPa (as reported in [59, page 59-60]). The correspondence with the experimental data, which are also shown in the figure, is indeed good up to at least 0.4  $\text{\AA}^{-1}$ . The dispersions according to LCBOPII, also shown in the figure, clearly predict smaller values of  $\kappa$  which can be explained as an effect of temperature as discussed above. If we zoom in further on the origin we can clearly see that the dispersion of graphite starts off linearly and later becomes quadratic while the dispersion of graphene is purely quadratic thus confirming qualitatively equations (3.42) and (3.43).

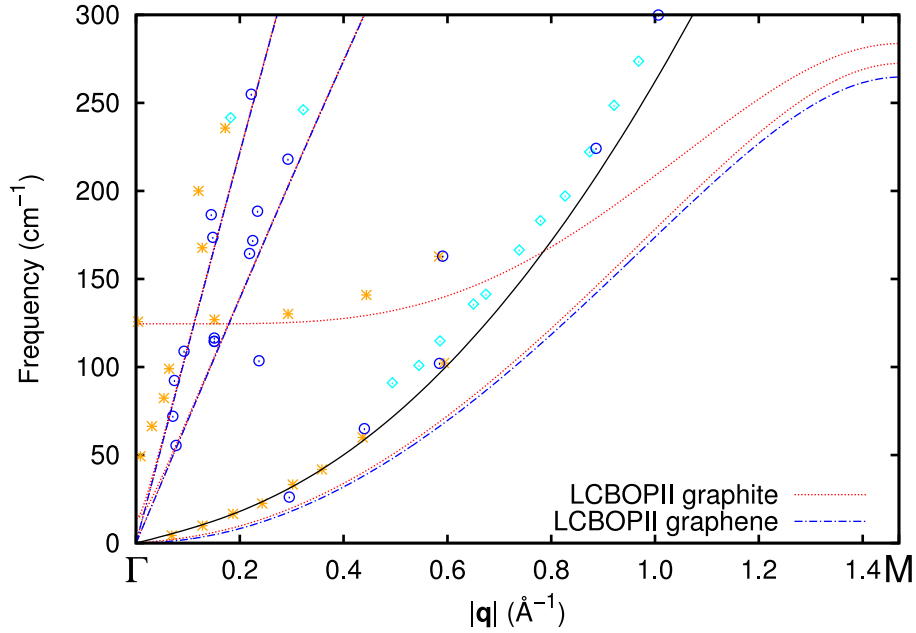


Figure 3.18: Low energy part of the graphene and graphite phonon dispersions along the  $\Gamma - M$  line. The experimental for graphite is from [39] (circles), [42] (stars) and [41] (diamonds). The solid line is dispersion for graphite as given by equation (3.42) with  $C_{44} = 4.5$  GPa (experimental result from [59, page 59-60]) and  $\kappa = 1.06$  eV per layer (.

We fitted the dispersion of the graphite ZA mode according to LCBOP1I to equation (3.42) with the same maximum value of  $|q|$  as for graphene. The resulting value for  $\kappa$  is  $0.69 \pm 0.01$  eV and  $C_{44}$  is equal to  $(5.8 \pm 0.2) \times 10^8$  Pa.

The values of  $\kappa$  for graphite and graphene are the same, save for the larger error margins of graphene. This result is compatible with the findings from [58], which shows that the bending rigidities of graphene and bilayer graphene are almost the same if one takes the bending rigidity per layer. The value of  $C_{44}$  is much lower than the experimental value of 4.5 GPa. This is not surprising recalling that the energy of the shearing motion of the graphene layers in graphite, the TA and TO' branches along  $A - \Gamma$ , is not well reproduced by LCBOP1I as we have seen from figure 3.13. This shearing motion is precisely what determines the value of  $C_{44}$  (see [33, chap. 2]).

### Bending rigidity from direct energy calculations

The second method of calculating the bending rigidity applies only to a single sheet of graphene. As explained in [56] the energy required to bend a flat graphene sheet into a nanotube is equal to

$$\mathcal{E} = \frac{1}{2}\kappa H^2, \quad (3.47)$$

where  $\mathcal{E}$  is the energy of the tube per unit area and  $H$  is the curvature, namely one over the radius of the nanotube. We calculated the energy of several zigzag nanotubes with radii ranging from 23 to 55 Å. The results are shown in figure 3.19. Indeed, the energy increases linearly with the curvature squared as given by (3.47). The slope calculated from the best linear fit to this data gives a value of  $\kappa = 0.69$  eV,

which is in agreement with the previous results. As noted in [56] the chirality of the nanotube does not have influence on this result because the graphene sheet is elastically isotropic.

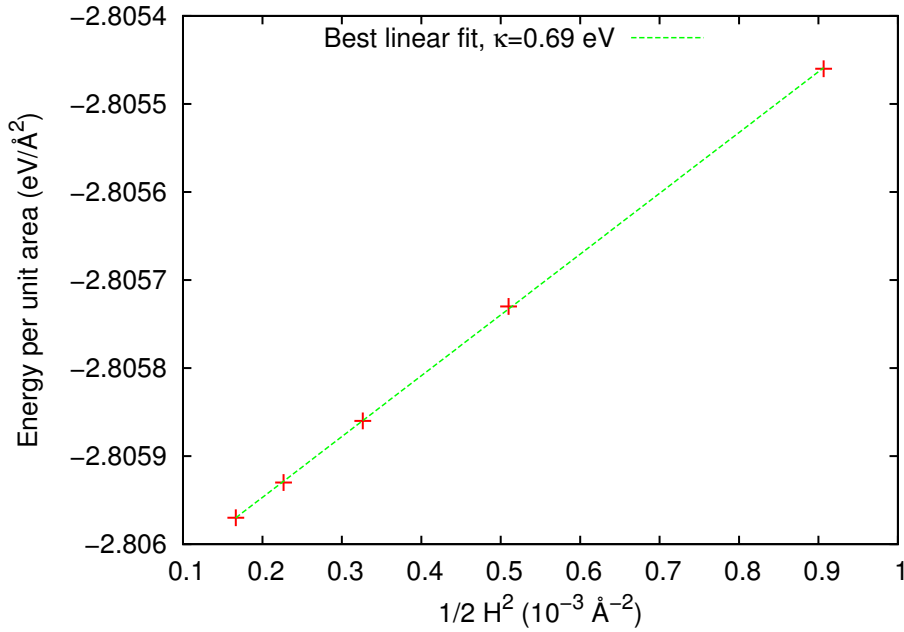


Figure 3.19: Energy per unit area of zigzag nanotubes of varying curvature,  $H$ . The slope of the curve gives the bending rigidity  $\kappa = 0.69$  eV from equation (3.47).

### Bending rigidity from interatomic force constants

As derived in [57], one can also calculate the bending rigidity of graphene directly from the force constants by means of equation (3.44). With the force constants from LCBOPII, listed in table 3.4, we calculate a value of  $\kappa = 0.698$  eV.

The three methods described above all give a value of  $\kappa$  around 0.69 eV per layer. This result is slightly lower than the other zero temperature values of 0.79 and 0.82 eV ([47] and [5]) but it is still comparable. The fact that the three different methods yield the same value for  $\kappa$  gives us confidence that the value of 0.69 eV is reliable. Other results in the literature are derived from the phonon spectrum of graphite taken at room temperature and give higher values of  $\kappa$ . This is explained by the temperature dependence of the bending rigidity as reported by Zakharchenko et al. [58]. This finding means that a direct fit to experimental values obtained at room temperature is bound to give too high values of  $\kappa$ .

Finally, we comment on the apparent discrepancy in the values of  $\kappa$  from LCBOPII. We report a value of 0.69 eV here, but MC simulations from LCBOPII give  $\kappa=0.82$  eV [5]. This difference is due to the functional form of the torsion energy, one of the contributions to the cohesive energy in LCBOPII. This function gives the energy cost for a torsion angle in a carbon-carbon bond in a graphitic environment which, due to the curvature, is present in all nanotubes. As it is currently implemented in the potential, the function gives too low energies costs for small torsion angles. Unfortunately, the systems we are considering fall precisely in the category of systems with small torsion angles, e.g. large diameter nanotubes and the small displacements used to calculate interatomic force constants for the phonon spectrum. The value of 0.69 reported here, was calculated without this torsion contribution. If the contribution is included, the linear relation from figure 3.19 becomes nonlinear and the value of  $\kappa$  depends on the radius of the nanotubes considered. The value of  $\kappa = 0.82$  eV can be obtained from nanotubes with radii of 11 Å and lower. In MC simulations of course, the system is not restricted to the small torsion angles and

the resulting value of  $\kappa$  is therefore larger.

The value of 0.69 eV is thus the bending rigidity from LCBOPII without the inclusion of torsion effects. The true value of  $\kappa$  from LBOPII at zero temperature remains undetermined (Monte Carlo simulations are only performed at finite temperatures), all we can say is that it is higher than 0.69 eV although probably not very much higher since torsion is only a secondary contribution. With the current implementation of the torsion energy it is not possible to determine  $\kappa$  with any of the three techniques used in this section because all three are limited to small torsion angles.

### 3.4 Free energy minimization and thermal expansion

The quasiharmonic approximation introduces anharmonic effects by making the phonon frequencies dependent on the lattice parameters as discussed in section 3.1.2. The equilibrium state of the crystal at finite temperature can be found by minimizing the free energy which is given by the expression (3.28). We repeat the formula here for easy reading:

$$\begin{aligned} F(\{\mathbf{a}_i\}, T) &= U(\{\mathbf{a}_i\}) + F_{zp}(\{\mathbf{a}_i\}) + F_{therm}(\{\mathbf{a}_i\}, T) \\ &= U(\{\mathbf{a}_i\}) + \sum_{qj} \frac{\hbar\omega(\mathbf{q}, j, \{\mathbf{a}_i\})}{2} + k_B T \sum_{qj} \ln \left[ 1 - \exp \left( -\frac{\hbar\omega(\mathbf{q}, j, \{\mathbf{a}_i\})}{k_B T} \right) \right]. \end{aligned}$$

The first term,  $U$ , is simply the cohesive energy of the lattice. It is independent of temperature and will increase if any of the  $\mathbf{a}_i$  increases or decreases from its equilibrium value. The second term,  $F_{zp}$ , describes the effect of the zero-point vibrations of the collection of quantum harmonic oscillators. This term is also independent of temperature and always has a positive contribution to the free energy. It depends on the lattice constants through the dependence on the phonon frequencies and generally we expect this term to decrease with increasing  $\mathbf{a}_i$  (since most modes have positive Grüneisen parameters). It is also useful to keep in mind that the high frequency (optical) modes will contribute the most to this term. Finally there is the third term,  $F_{therm}$ , which depends on both temperature and the lattice constants. For  $T = 0$  this term is equal to zero and with increasing temperature its value decreases. At low temperatures the value of this term is almost solely determined by the lowest frequency modes as the high frequency modes cannot yet be excited.

In this section we will perform a minimization of the free energy of the graphitic crystals we have studied before.

#### 3.4.1 Graphene

The phonon dispersion of graphene has been discussed in detail in section 3.2.2. To study the effects of a change in lattice parameter qualitatively we have calculated the phonon spectrum at three values of the carbon-carbon distance  $a_{CC}$ . The resulting dispersion curves are shown in figure 3.20. To make the effects clearly visible we have chosen the three values of  $a_{CC}$  separated by intervals of 0.01 Å. The in-plane modes (L and T modes) behave as one would normally expect from phonon modes. With increasing lattice parameter, the force constants become lower and the phonon frequencies go down. The two out-of-plane (Z) modes however show exactly the opposite behaviour. When the lattice parameter is increased, the tension in the graphene sheet grows making out-of-plane motion of the atoms more difficult. The out-of-plane force constants thus increase and the phonon frequencies go down. This effect was called the membrane effect by E.M. Lifshitz when he first predicted it in 1952 [54].

From figure 3.20 we can already see that the in-plane modes will have positive Grüneisen parameters, so they will promote thermal expansion. The out-of-plane modes have negative Grüneisen parameters, leading to thermal contraction. The low frequencies of the out-of-plane ZA mode, resulting from the quadratic dispersion relation, mean that this mode is easily excited at low temperatures and will have a large contribution to the overall thermal expansion. The carbon-carbon distances chosen in figure 3.20 are all larger than the zero temperature equilibrium value of 1.4198 Å. This is because when the lattice parameter is decreased too much, some of the eigenvalues of the dynamical matrix become negative,

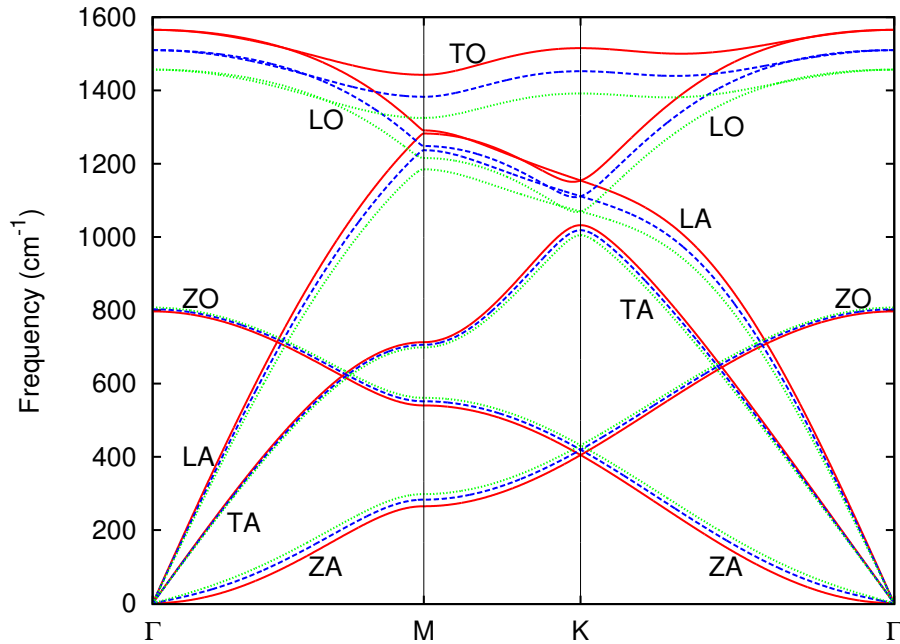


Figure 3.20: Phonon dispersion of graphene at three different lattice parameters. The red (solid) curve is at  $a_{CC} = 1.42 \text{ \AA}$ , the blue (dashed) curve is at  $a_{CC} = 1.43 \text{ \AA}$  and the green (dotted) curve is at  $a_{CC} = 1.44 \text{ \AA}$ .

resulting in imaginary phonon frequencies<sup>5</sup>. As explained in section 3.1 this implies that the crystal is unstable. The mode whose frequencies become imaginary is the ZA bending mode. To demonstrate this, we show  $\omega^2$  close to the zone center as a function of  $|q|$  in figure 3.21. At the equilibrium value,  $a_{CC} = 1.4198 \text{ \AA}$ , all eigenvalues are positive, no matter how close to  $\Gamma$ . When  $a_{CC}$  is decreased to  $1.4196 \text{ \AA}$  the eigenvalues,  $\omega^2$ , become negative close to the zone center. As  $a_{CC}$  is lowered further, the effect increases as can clearly be seen from figure 3.21.

The appearance of these nonphysical eigenvalues is a clear sign that the approximations of our method do not suffice to give a proper description of graphene at these lattice constants. This is not very surprising. In our calculations we assume the graphene sheet to be perfectly flat while, in fact, it is well known from both theory and experiments that graphene sheets are not flat but rippled at finite temperatures [5, 60]. Anharmonic coupling, between the in-plane stretching and out-of-plane bending modes, suppresses the long-wavelength fluctuations and thereby stabilizes the membrane. The fact that our calculations predict instability due to precisely these bending modes are an indication that anharmonic effects are not taken into account well enough by the quasiharmonic approximation. The negative eigenvalues, indicating an instability of the crystal, were also found by Schelling et al. [15], who calculated the phonon dispersion of graphene based on the Tersoff potential [25].

A direct consequence of these results is that we cannot calculate the free energy from equation (3.28) at carbon-carbon distances smaller than  $1.4198 \text{ \AA}$ . Since the coefficient of thermal expansion of graphene is predicted to be negative [13, 14] we will probably not be able to find the free energy minimum at all temperatures.

### Calculation and results

The free energy of graphene is calculated from expression (3.28) as a function of  $a_{CC}$  and temperature. The summation over the Brillouin zone is performed on a sufficiently dense Monkhorst-Pack mesh as described in section 3.1.4. To determine how many  $q$ -points are needed, we calculate the free energy for

<sup>5</sup>The eigenvalues of the dynamical matrix are equal to  $\omega^2(q, j)$  as derived in section 3.1.

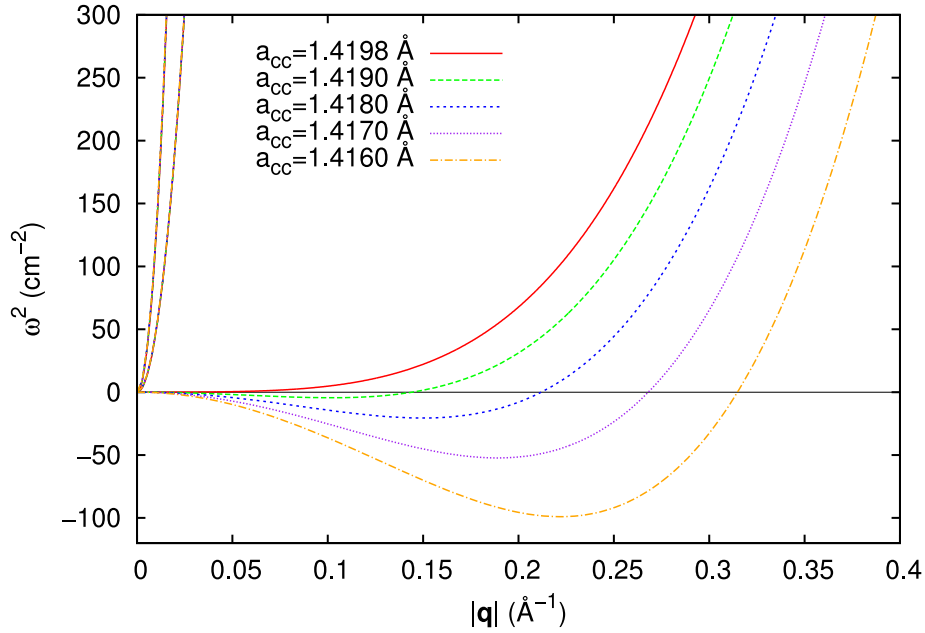


Figure 3.21: Instability of the flat graphene sheet results from imaginary phonon frequencies at small carbon-carbon distances. The ZA bending mode shows negative  $\omega^2$  close to the zone center  $\Gamma$ , along the  $\Gamma - M$  line, for lattice parameters smaller than the equilibrium value  $a_{CC} = 1.4198 \text{ \AA}$ . The value of  $|M|$  is  $1.47 \text{ \AA}^{-1}$ .

several meshes and check the convergence of the free energy. We performed these calculations at  $T = 50 \text{ K}$  and  $a_{CC} = 1.4226 \text{ \AA}$ , the value which was found to minimize the free energy at this temperature. The large increase with respect to the value of  $1.4198 \text{ \AA}$  at zero temperature is due to the effect of zero point motion as we will discuss later. All meshes include an offset, equal to half the binsize, from the zone center. The free energy curve is shown in figure 3.22. From this figure we conclude that a  $60 \times 60$  mesh with 3600  $q$ -points is sufficiently dense. All the following calculations were performed on this mesh. To get an impression of the binsize of this mesh, we plotted a grid with the correct spacing on top of the graphene phonon dispersion in figure 3.23.

Before we continue with the thermal expansion of graphene we consider the effect of the zero point term,  $F_{zp}$ , of the free energy. Upon adding the contribution from this term the equilibrium lattice constant at zero temperature increases from  $1.4198 \text{ \AA}$  to  $1.4257 \text{ \AA}$ . This is an increase of 0.4%, which is comparable to the 0.3% found by Mounet and Marzari by *ab initio* calculations [14]. At low temperatures the contribution from the zero point motion is much larger than the contribution from the thermal term  $F_{therm}$ . At 50 K for example, the typical  $F_{therm}$  is of the order of  $10^{-4} \text{ eV}$  per atom while the magnitude of  $F_{zp}$  is about 0.16 eV per atom at any temperature. The contributions from the two terms become comparable at around 1000 K. The contributions from  $F_{zp}$  and  $F_{therm}$  at 300 K are shown in figure 3.24. At this temperature, the zero point contribution is still an order of magnitude larger than the contribution from  $F_{therm}$ .

The free energy was calculated every 20 Kelvin for 60, equally spaced, lattice parameters between  $1.4194$  and  $1.4312 \text{ \AA}$ . At every temperature, the lattice parameter minimizing the free energy was calculated by fitting a polynomial to the free energy data. The resulting carbon-carbon distance, as a function of temperature, is shown in the left plot of figure 3.25. By direct numerical differentiation we also calculated the corresponding coefficient of thermal expansion,  $\alpha$ , which is shown in the right plot of figure

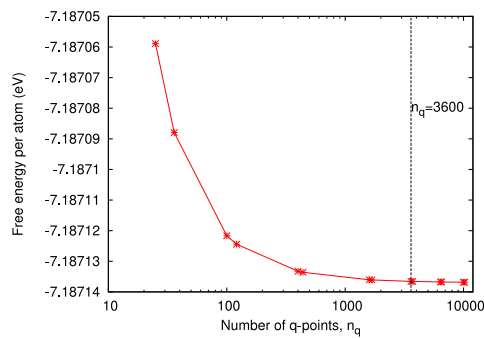


Figure 3.22: Convergence of the free energy of graphene with increasingly dense Monkhorst-Pack mesh. Value of  $n_q = 3600$  is used for further calculations.

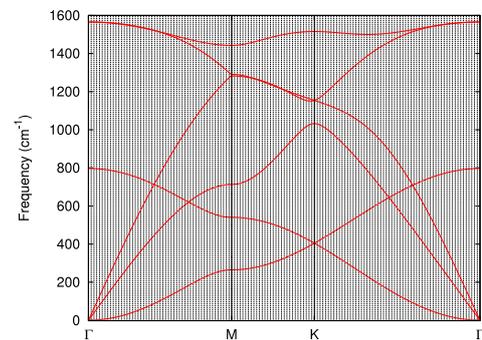


Figure 3.23: Bin spacing of the Monkhorst-Pack mesh with  $n_q = 3600$  used to minimize the free energy for graphene.

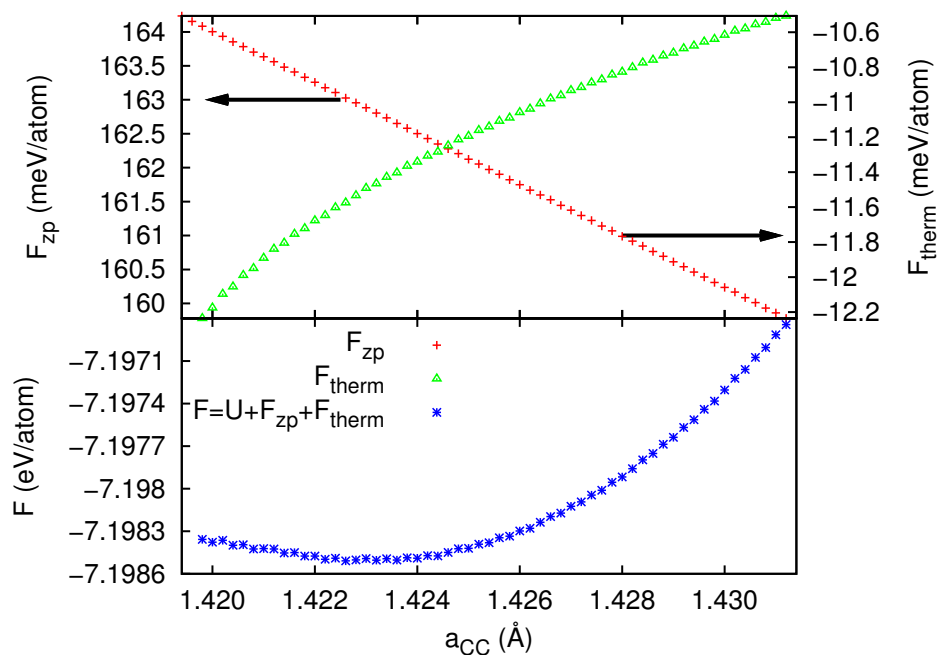


Figure 3.24: Contributions to the free energy from zero point motion  $F_{zp}$  and the temperature dependent term  $F_{therm}$  for graphene at  $T = 300$  K. The lower figure show the resulting free energy curve,  $F = U + F_{zp} + F_{therm}$ .

3.25. As expected, the carbon-carbon distance indeed decreases with increasing temperature leading to a negative coefficient of thermal expansion. At room temperature we find a value of  $\alpha = -10 \times 10^{-6} \text{ K}^{-1}$ . The main reason for the negative coefficient is the quadratic ZA mode which becomes softer with decreasing carbon-carbon distance.

Due to the appearance of negative eigenvalues, for lattice parameters smaller than  $1.4198 \text{ \AA}$ , we cannot find the minimum of the free energy for temperatures higher than 340 K. Up to this temperature the results agree qualitatively with *ab initio* quasiharmonic results from [14] and LCBOPII-based Monte Carlo results from [58]. Both studies predict a negative coefficient of thermal expansion for graphene with values of  $-3.5 \times 10^{-6} \text{ K}^{-1}$  and  $-(4.8 \pm 1) \times 10^{-6} \text{ K}^{-1}$  respectively. The Monte Carlo study however, reports a positive  $\alpha$  for temperatures above 900 K while the quasiharmonic study finds negative  $\alpha$  over the whole studied temperature range (up to 2300 K). A value of  $-18.2 \times 10^{-6} \text{ K}^{-1}$  is reported in [15]. This value was calculated from the mode-dependent Grüneisen parameters obtained from the Tersoff potential.

There is one experimental result available from Bao et al. [16] who report a value of  $-7 \times 10^{-6} \text{ K}^{-1}$  from measurements up to 400 K. The values reported by other studies differ too much to comment on the correctness of our findings. But as we have seen, the applicability of the quasiharmonic approximation to graphene not obviously guaranteed. Therefore, the value from [58], which takes into account all anharmonic effects, seems more reliable.

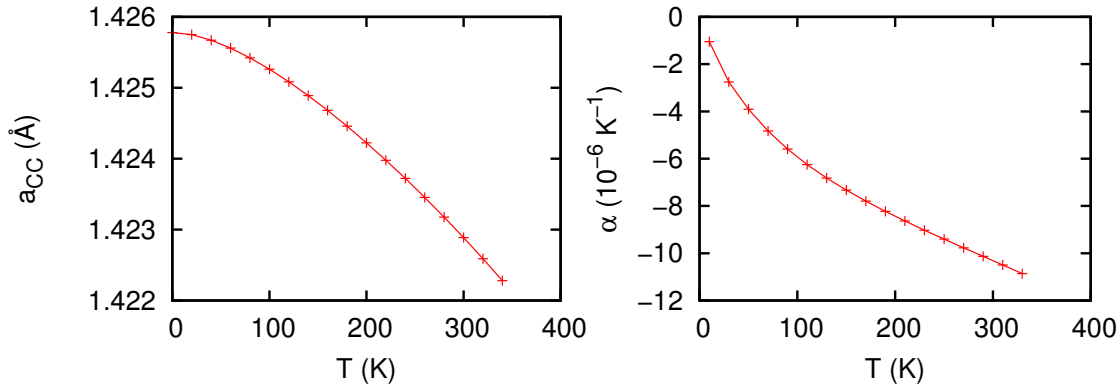


Figure 3.25: Left: lattice parameter of  $a_{CC}$  as a function of temperature graphene obtained by direct minimization of the free energy. Right: corresponding coefficient of thermal expansion for graphene.

### Grüneisen parameters

The mode-dependent Grüneisen parameters for graphene were calculated by numerical differentiation of the phonon frequencies with respect to the carbon-carbon distance  $a_{CC}$ . Following [14] we have used the definition

$$\gamma(\mathbf{q}, j) = -\frac{a_{CC}}{2\omega(\mathbf{q}, j)} \frac{d\omega(\mathbf{q}, j)}{da_{CC}}.$$

The derivatives were taken based on the central difference around  $a_{CC} = 1.42 \text{ \AA}$  with an  $\epsilon$  of  $0.005 \text{ \AA}$ . This means that the lower value of  $a_{CC}$  used is equal to  $1.4195 \text{ \AA}$ , which is unfortunately too much compressive strain to keep the crystal stable, and gives imaginary phonon frequencies. These frequencies cannot be used to take derivatives in order to determine the Grüneisen parameters. Therefore, at wavevectors very close to  $\Gamma$  (refer to figure 3.21) have been calculated using the less accurate forward difference algorithm. There is no way to avoid these troubles if we want to take the derivative at the equilibrium lattice constants, because the smallest decrease in lattice parameter already results in some imaginary frequencies. The resulting Grüneisen parameters are shown in figure 3.26. Indeed, the out-of-plane modes show negative  $\gamma(\mathbf{q}, j)$ , which means that they will contribute to thermal contraction. The Grüneisen parameters of the ZA mode become as low as -300 close to the zone center (but still not that close to  $\Gamma$  that frequencies

are imaginary). These very low parameters, together with the low frequencies of the ZA mode, make it by far the most influential mode on the thermal expansion at low temperature, when other phonon modes are still not excited.

The calculated Grüneisen parameters compare well with the results from Mounet and Marzari [14]. They report less negative values for the ZA mode (down to -80 for graphene), which is in agreement with their lower value of  $\alpha$ .

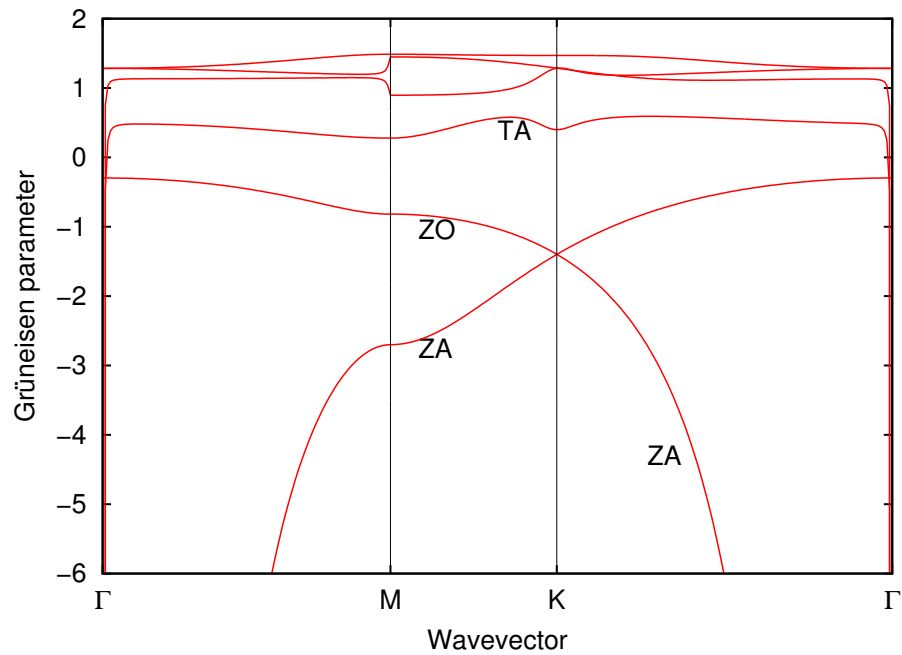


Figure 3.26: Mode dependent Grüneisen parameters for graphene. The two negative branches are the out-of-plane modes.

### 3.4.2 Graphite

The thermal expansion of graphite is highly anisotropic. It is known that at room temperature the coefficient of thermal expansion in the direction of the basal plane is negative, while the coefficient normal to this plane is much larger and positive [59, 61]. Measurements by Bailey and Yates [61] give values of  $\alpha = -1.28 \times 10^{-6} \text{ K}^{-1}$  in the in-plane direction and  $\alpha_c = 2.72 \times 10^{-5} \text{ K}^{-1}$  along the  $c$ -axis (perpendicular to the planes) at 270 K. Just as in graphene, the negative thermal expansion is due to the out-of-plane phonon modes which have negative Grüneisen parameters. This can also be seen from figure 3.27, where the phonon dispersion of graphite by LCBOP-II is shown at three different carbon-carbon distances with the interplane distance  $c/2$  held constant at 3.3672 Å. The ZA, ZO and ZO' branches show a decrease in frequency with increasing in-plane lattice parameter indicating negative Grüneisen parameters.

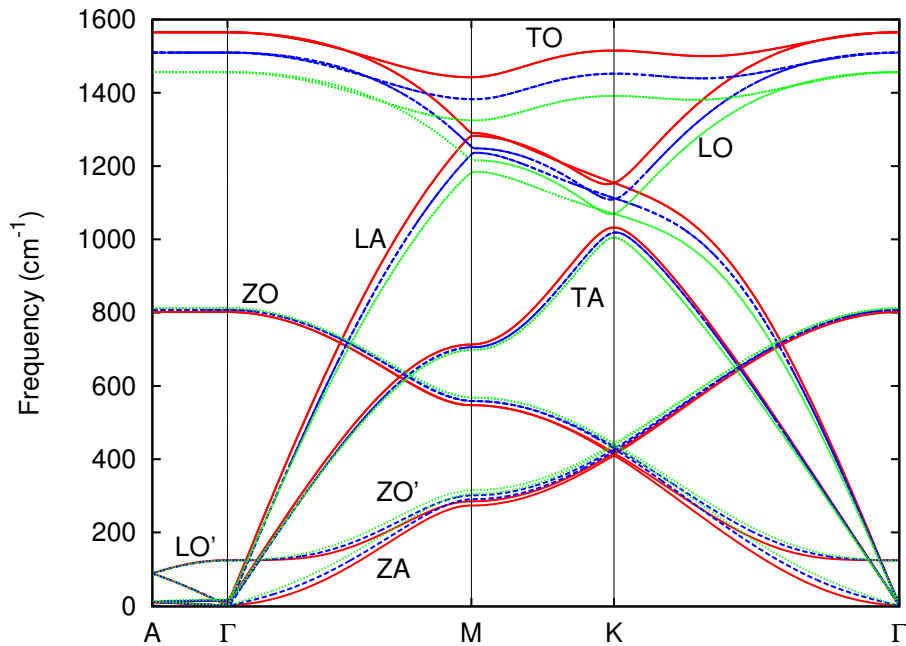


Figure 3.27: Phonon dispersion of graphite at three different lattice parameters. The red (solid) curve is at  $a_{CC} = 1.42 \text{ \AA}$ , the blue (dashed) curve is at  $a_{CC} = 1.43 \text{ \AA}$  and the green (dotted) curve is at  $a_{CC} = 1.44 \text{ \AA}$ .

The interlayer interaction in graphite restricts out-of-plane fluctuations when compared to graphene. This means that the out-of-plane modes in graphite will contribute less to the thermal contraction than in graphene resulting in a smaller coefficient of thermal expansion. This is confirmed by Mounet and Marzari [14] who calculated the thermal expansion of graphite and graphene in the quasiharmonic approximation based on *ab initio* phonon dispersions. The restriction of the out-of-plane modes also shows when we look at the frequencies of the ZA mode at smaller than equilibrium carbon-carbon distances. For graphene, we have seen that imaginary frequencies appear at bond lengths immediately below the equilibrium lattice constant. For graphite however, we can decrease the bond length from the equilibrium 1.4194 Å down to 1.4182 Å before imaginary frequencies appear for the ZA mode close to  $\Gamma$ . This is an indication that anharmonic effects play a less important role in graphite than in graphene.

#### Calculation and results

For the determination of the free energy minimum of graphite we have used a  $60 \times 60 \times 19$  Monkhorst-Pack  $q$ -point mesh containing 68400 points. We kept the interplane distance constant at the zero temperature value of 3.3672 Å during all calculations. Since we know that the thermal expansion along the  $c$ -axis is significant, this is not the most realistic choice. But since the interlayer interactions are weak the influence of the interplane distance should be limited. By only varying the carbon-carbon distance, the

computation time is reduced greatly because phonon frequencies need to be calculated for all carbon-carbon distances once, and not separately for every temperature due to the changing interlayer distance. The free energy was calculated for 66 carbon-carbon distances ranging from 1.4188 to 1.4318 Å at temperatures from 0 to 2400 K separated by 20 K intervals. As was the case for graphene, the zero point motion increases the bond length by 0.4% from 1.4194 to 1.4254 Å.

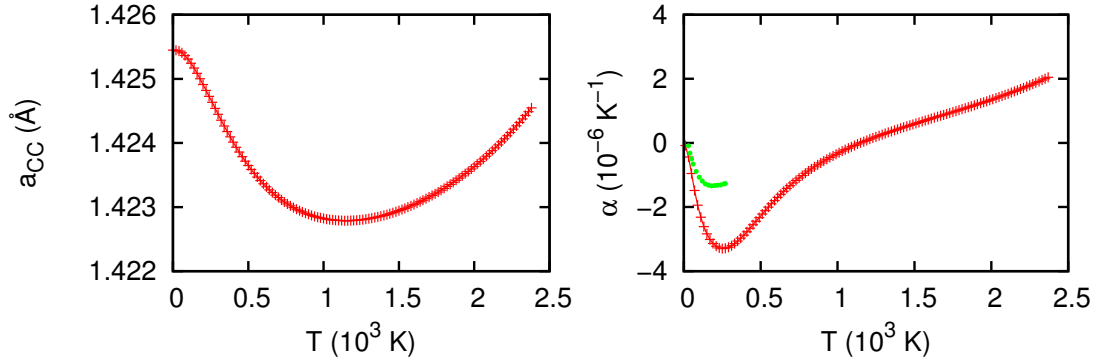


Figure 3.28: Left: carbon-carbon distance in graphite as a function of temperature from direct free energy minimization based in the LCBOPII potential. Right: the corresponding coefficient of thermal expansion,  $\alpha$  and experimental results from [61] (green circles).

The resulting temperature dependence of the carbon-carbon distance and the corresponding coefficient of thermal expansion are shown in figure 3.28. In contrast to graphene, we were able to determine the minimum free energy of graphite for all studied temperatures. In the basal plane direction, the lattice contracts up to 1150 K and starts expanding at higher temperatures. This is qualitatively in agreement with *ab initio* results from [14]. The coefficient of thermal expansion has a minimum at 250 K of  $-3.3 \times 10^{-6} \text{ K}^{-1}$ . This is a much smaller value than the  $-10 \times 10^{-6} \text{ K}^{-1}$  that was found for graphene which confirms that anharmonic effects in graphene have a much larger influence than in graphite. Compared with experimental values from [61] however, our calculations still predict a too low value for  $\alpha$  as can be seen from figure 3.28.

### 3.4.3 Bilayer graphene

Thermal expansion in bilayer graphene at low temperatures is, just as in graphite and graphene, mainly determined by the long-wavelength out-of-plane phonons modes. Since we have seen negative in-plane thermal expansion at low temperatures for both graphite and graphene we expect the same behaviour for bilayer graphene. The fact that the graphene layers in the bilayer system both have one neighbouring layer suggests that movement normal to the planes is more restricted than in the single layer case and more free than in graphite. This means that the coefficient of thermal expansion will be in between the two values from single layer graphene and graphite. This is also found by Monte Carlo simulations with the LCBOPII potential in [58]. Experimental results on the thermal expansion of bilayer graphene are, to the best of our knowledge, not available.

### 3.4.4 Calculations and results

The free energy calculations on bilayer graphene were performed on the same  $60 \times 60$   $q$ -point mesh as was used for graphene. The distance between the two planes was again kept constant at the zero temperature equilibrium value of  $3.3670 \text{ \AA}$ . For the same reasons as in single layer graphene we were unable to determine the thermal expansion in the whole temperature range up to 2500 K. We were able to find the minima of the free energy up to 600 K. The results are shown in figure 3.29.

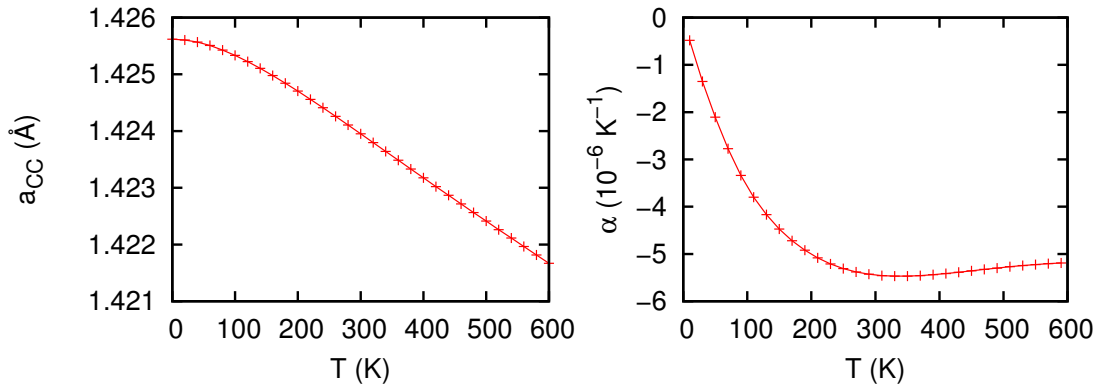


Figure 3.29: Left: carbon-carbon distance in bilayer graphene as a function of temperature from direct free energy minimization based in the LCBOPII potential. Right: the corresponding coefficient of thermal expansion.

As we had expected, the coefficient of thermal expansion is negative and its value is larger than for graphite, but smaller than for the single layer. There appears to be a minimum of  $-5.5 \times 10^{-6} \text{ K}^{-1}$  at 330 K. This temperature is in agreement with the Monte Carlo results from [58] but the value of  $\alpha$  we find is slightly larger than the  $(-3.0 \pm 0.7) \times 10^{-6} \text{ K}^{-1}$  which they report. One reason for this is that this value is an average over the temperature range 0-300 K while our value is the absolute minimum. For easy comparison, the quasiharmonic results for graphene, bilayer graphene and graphite are shown together in figure 3.30.

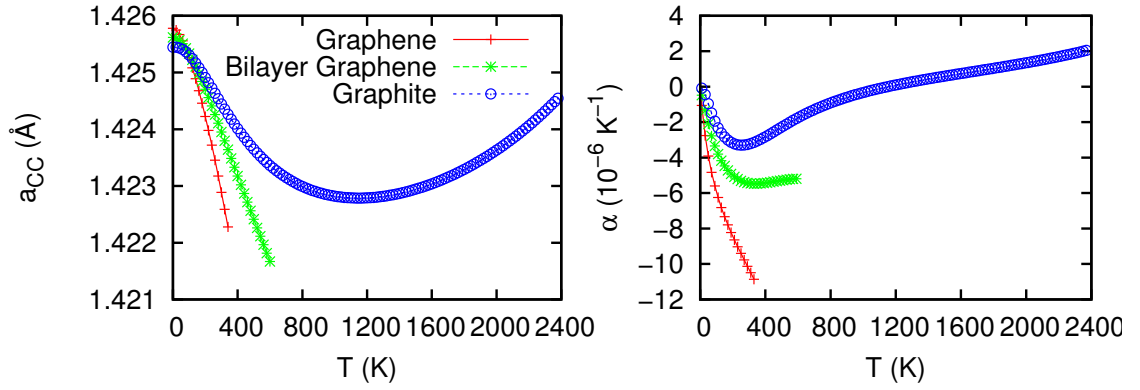


Figure 3.30: Quasiharmonic results for the temperature dependence of the carbon-carbon distance and the corresponding coefficient of thermal expansion for graphene, graphite and bilayer graphene.

### 3.4.5 Carbon nanotubes

The final carbon allotrope to which we will apply the quasiharmonic approximation are the carbon nanotubes. Due to the complex structure of the nanotubes it would take too much computation time to determine the radial and axial coefficients of thermal expansion separately and we therefore focus on the volumetric coefficient of thermal expansion  $\alpha_v$  which is defined as

$$\alpha_v = \frac{1}{V} \frac{dV}{dT}. \quad (3.48)$$

This means that we start from a minimal energy carbon nanotube sample and calculate the phonon dispersions of the sample at different volumes by isotropically scaling the atomic coordinates and determining the interatomic force constants.

#### Calculations and results

The free energy calculations were performed on the (10,10) armchair nanotube which has a radius of 6.780 Å. This nanotube was chosen because it is naturally abundant and is therefore widely used in other numerical and theoretical studies. This is also the nanotube type that was used in section 2.1.2 for Monte Carlo simulations with wavemoves.

As noted in section 3.2.5 the phonon dispersion relations of carbon nanotubes can be approximated by zone folding the phonon spectrum of graphene (save for the effects of curvature). Since we know that the out-of-plane, low-frequency phonon modes of graphene have negative Grüneisen parameters we also expect to see modes with negative parameters in the low frequency region of the nanotube. Due to the rolling up process of the graphene sheet the out-of-plane modes become radial modes in the nanotube, but it seems reasonable to expect that the sign of the Grüneisen parameters will not change in the process.

To test this conjecture we calculated the phonon frequencies of the (10,10) nanotube at its equilibrium configuration, and in the configuration with all coordinates increased by 1 %. In figure 3.31 we see that indeed, the lower energy modes show an increase in frequency with increasing volume indicating negative Grüneisen parameters. The highest mode with negative Grüneisen parameter has a frequency of  $800 \text{ cm}^{-1}$  at the zone center which is in agreement with the frequency of the ZO mode in graphene. The doubly degenerate, quadratic, transverse bending mode also has a negative Grüneisen parameter and will thus contribute to negative thermal expansion.

The one-dimensional Brillouin zone of the carbon nanotube means that the number of  $q$ -points needed to integrate over the Brillouin zone is much lower than for graphene or graphite. It was found that a Monkhorst-Pack mesh containing 75 points and an offset equal to half the binsize was enough to properly converge the free energy of the carbon nanotube.

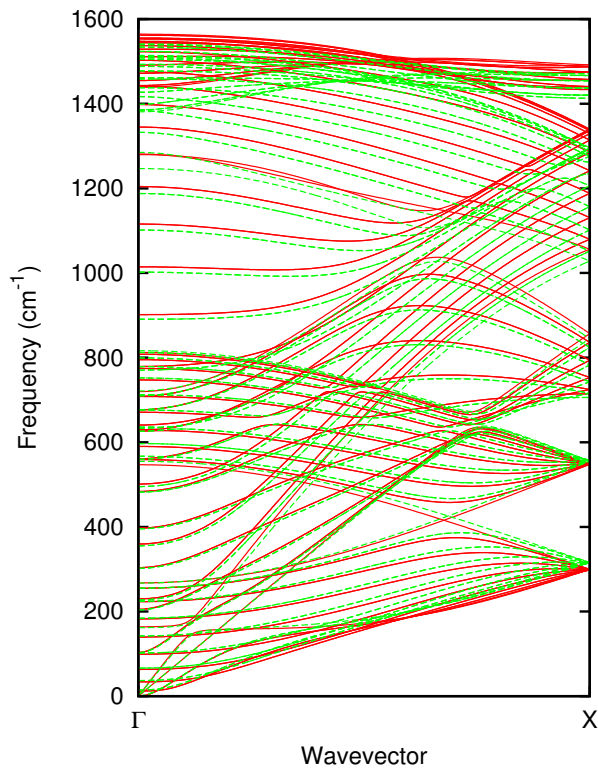


Figure 3.31: Phonon dispersion of the (10,10) armchair nanotube at two different volumes. The red (solid) lines are the phonon frequencies at the equilibrium structure, the green (dotted) lines at the phonon frequencies with all coordinates scaled by a factor 1.01.

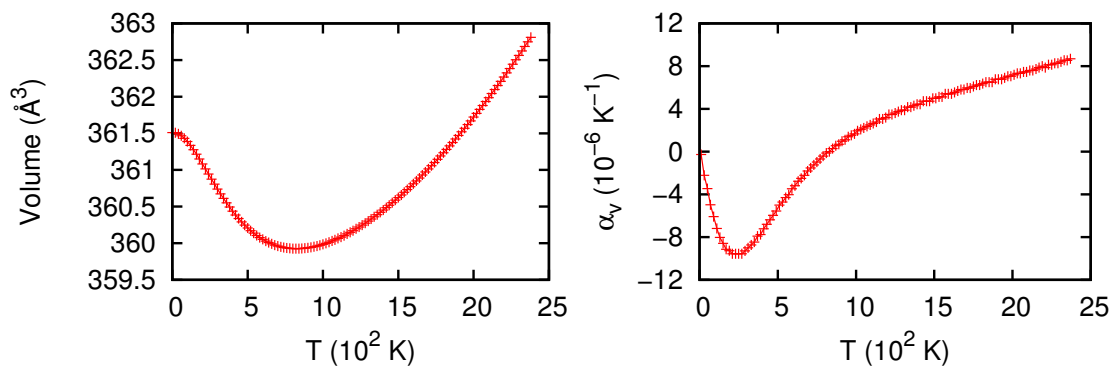


Figure 3.32: Left: unit cell volume of the (10,10) nanotube as a function of temperature obtained by free energy minimization in the quasiharmonic approximation. Right: corresponding volumetric coefficient of thermal expansion  $\alpha_v$ .

The free energy was calculated according to formula (3.28) for 200 configurations with equally spaced radii ranging from 6.746 Å to 7.022 Å. The minima of the free energy were determined up to 2400 K. The equilibrium volume as a function of temperature is shown in the left panel of figure 3.32. The corresponding volumetric coefficient of thermal expansion is shown in the same figure on the right.

We see the same trend in the coefficient of thermal expansion as we have seen for graphite and (bilayer) graphene. The coefficient is negative for low temperatures and becomes positive after some crossover temperature. In this case, we find a minimum value of  $\alpha_v = -9.6 \times 10^{-6} \text{ K}^{-1}$  at  $T = 270 \text{ K}$ . Even though this result supports the results of Kwon et al. [19], who find the same behaviour of the volumetric coefficient of thermal expansion in the (10,10) nanotube, it contradicts our earlier findings from atomistic simulations. We will elaborate on this discrepancy in the following section.

### 3.5 Discussion of the quasiharmonic results

The results on the coefficients of thermal expansion (CTEs) for carbon nanotubes we find from Monte Carlo simulations and from the quasiharmonic approximation are not consistent with each other. The quasiharmonic approach predicts a negative volumetric coefficient of thermal expansion for the (10,10) nanotube at low temperature which becomes positive for temperature higher than 830 K. Contradictively, we found positive coefficients of thermal expansion for the same nanotube in both radial and axial directions in the temperature range from 50 to 400 K by means of Monte Carlo simulations in section 2.1.2.

One obvious approximation we have used in the quasiharmonic approximation that is not present in the Monte Carlo simulations is the treatment of isotropic thermal expansion only. But since the MC simulations predicted positive CTEs in both radial and axial directions this cannot explain the different outcomes of the two methods. Since the results from scientific literature are also highly contradictory, as discussed in section 2.1.1, they do not offer much help in determining which of the two methods is the most reliable.

Another point is that the atomistic simulations we have performed are completely classical, whereas the free energy minimization procedure includes the quantum distribution of the phonons. In the classical approximation all vibrational modes are equally excited while in the quantum case higher energy phonon cannot exist at low temperatures. The classical approximation is justified in most solids at relatively low temperatures (below room temperature) but for graphitic crystals this temperature might be a lot higher. The heat capacity calculated for graphene and graphite by Mounet and Marzari [14] reaches a constant value at temperatures well above 1000 K indicating a very high Debye temperature. On the other hand, classical Molecular Dynamics simulations have reported negative coefficients of thermal expansion in carbon nanotubes [19, 22].

The Monte Carlo method however has the advantage that it takes into account all anharmonic effects in the system whereas the quasiharmonic approximation only weakly includes anharmonicity by dependence of the phonon frequencies on lattice parameters. Stronger anharmonic effects such as phonon-phonon interactions are neglected in this approximation. These processes however can have strong influence on the crystal structure. For example, this is the case in graphene, which is even stabilized by the anharmonic coupling of bending and stretching modes [5].

We have also seen that the bending rigidity,  $\kappa$ , of graphene layers increases with temperature which suggests that the ZA phonon mode, to which the bending rigidity is intimately related, is also dependent on temperature. The increase of  $\kappa$  would, by this reasoning, increase the frequencies of the ZA mode at finite temperatures, thereby decreasing the Grüneisen parameters. This would, in turn, mean that the contribution to the thermal expansion from this mode is decreased leading to higher CTEs over the whole range of graphene-based crystals. This increase of CTEs would not be unrealistic. Since, if we look back, the CTEs for graphene and bilayer graphene are both lower than the values found by Monte Carlo simulations based on LCBOPII (performed by Zakharchenko et al. [58]). Also in the case of graphite do we find a lower CTE than the one measured experimentally. By the same reasoning, the CTE of carbon nanotubes would also be affected, improving the correspondence with our Monte Carlo results. To see if the temperature-dependence of the phonon spectra does indeed play an important role another method is needed for the calculation of the phonon dispersions. A good candidate for such calculations is the Self Consistent Ab Initio Lattice Dynamics (SCAILD) method developed by P. Souvatzis [62]. With this method it is possible to calculate phonon dispersions of solids at finite temperatures taking into account phonon-phonon interactions in a self-consistent manner. This method could, in principle, be used in combination with the LCBOPII potential. Unfortunately, there was no time to perform these calculations for this thesis but it certainly is an interesting subject for future research. Until this method has been tried, it is at least difficult to trust the results from the quasiharmonic approximation as its applicability is not naturally guaranteed in systems such as graphene and its derivatives.

## Summary and conclusions

We have studied the thermal expansion of carbon nanotubes by means of Monte Carlo simulations in the  $NpT$  ensemble using the LCBOPII empirical potential [6]. The coefficients of thermal expansion were found to be positive in both the radial and axial direction. The coefficient of thermal expansion of the individual bond lengths is a factor two larger than the global coefficients which leads us to conclude that low energy vibrational modes contribute towards negative thermal expansion. To ensure that these modes were sufficiently sampled in the Monte Carlo routine we introduced wave moves as an additional Monte Carlo move and used supercells up to 1000 Å in length to accommodate long-wavelength modes. These changes were found to have an insignificant effect on the coefficients of thermal expansion.

By means of lattice dynamics we calculated the phonon dispersions of graphite, graphene and carbon nanotubes in the harmonic approximation, again based on the LCBOPII potential. The overall agreement of the phonon dispersions with experiments is fairly good, and much better compared to results from other empirical potentials. Analysis of the interatomic force constants revealed that particularly the longer range force constants are predicted too low by LCBOPII to reproduce the finer details of the phonon spectra correctly. It was shown that agreement with experiments can be greatly improved by modifying the force constants beyond first nearest neighbours, which are determined by the long-range part of LCBOPII. This means that the accuracy of the empirical potential can be improved by making modifications to the long-range interactions and leaving the short-range, bond-order part of the potential unchanged.

From the low-frequency parts of the phonon spectra of graphite and graphene we determined the sound velocities of the linear phonon branches and the bending rigidity of a graphene sheet. The sound velocities are in good agreement with experimental values. The bending rigidity,  $\kappa$ , was determined to be 0.69 eV per graphene layer. This is a lower than the one given by experiments values, but Monte Carlo simulations [5, 58] have shown that  $\kappa$  increases with temperature which explains our lower value.

We determined the thermal expansion of graphene, graphite and carbon nanotubes from the phonon spectra in the quasiharmonic approximation. It was shown that acoustic out-of-plane phonon modes play a key role in the thermal expansion of these systems. By minimization of the free energy, negative coefficients of thermal expansion were found at low temperatures for all systems. In the case of graphene and bilayer graphene however, we were not able to determine the coefficients of thermal expansion for all temperatures due to imaginary phonon frequencies at small lattice parameters. This points to instabilities in the system and makes us doubt whether the application of the quasiharmonic approximation is justified in these systems, where anharmonic effects are believed to play an important role. Further research is needed on the subject to obtain more reliable results and to resolve the much disputed matter of the thermal expansion of carbon nanotubes. A suitable candidate for the continuation of this work is the SCAILD method [62] which can self-consistently determine phonon spectra at finite temperatures and which accounts for anharmonic effects better than the quasiharmonic approximation.



# References

- [1] Mikhail I. Katsnelson. Graphene: carbon in two dimensions. *Mat. Today*, 10(1-2):20–27, 2007.
- [2] R. Saito, G. Dresselhaus, and M. S. Dresselhaus. *Physical Properties of Carbon Nanotubes*. World Scientific Publishing Company, 1998.
- [3] K. S. Novoselov, A. K. Geim, S. V. Morozov, D. Jiang, Y. Zhang, S. V. Dubonos, I. V. Grigorieva, and A. A. Firsov. Electric Field Effect in Atomically Thin Carbon Films. *Science*, 306(5696):666–669, 2004.
- [4] N. D. Mermin. Crystalline order in two dimensions. *Phys. Rev.*, 176(1):250–254, 1968.
- [5] A. Fasolino, J. H. Los, and M. I. Katsnelson. Intrinsic ripples in graphene. *Nat. Mater.*, 6(11):858–861, 2007.
- [6] J. H. Los and A. Fasolino. Intrinsic long-range bond-order potential for carbon: Performance in monte carlo simulations of graphitization. *Phys. Rev. B*, 68(2):024107, 2003.
- [7] H.W. Kroto, J.R. Heath, S.C. Obrien, R.F. Curl, and R.E. Smalley. C-60 - Buckminsterfullerene. *Nature*, 318(6042):162–163, 1985.
- [8] S. Iijima. Helical microtubules of graphitic carbon. *Nature*, 354:56–58, 1991.
- [9] S Iijima and T Ichihashi. Single-shell carbon nanotubes of 1-nm diameter. *Nature*, 363(6430):603–605, 1993.
- [10] Jan H. Los, Luca M. Ghiringhelli, Evert Jan Meijer, and A. Fasolino. Improved long-range reactive bond-order potential for carbon. i. construction. *Phys. Rev. B*, 72(21):214102, 2005.
- [11] Luca M. Ghiringhelli, Jan H. Los, Evert Jan Meijer, A. Fasolino, and Daan Frenkel. Modeling the phase diagram of carbon. *Phys. Rev. Lett.*, 94(14):145701, 2005.
- [12] L. M. Ghiringhelli, C. Valeriani, J. H. Los, E. J. Meijer, A. Fasolino, and D. Frenkel. State-of-the-art models for the phase diagram of carbon and diamond nucleation. *Mol. Phys.*, 106(16):2011–2038, 2008.
- [13] K. V. Zakharchenko, M. I. Katsnelson, and A. Fasolino. Finite temperature lattice properties of graphene beyond the quasiharmonic approximation. *Phys. Rev. Lett.*, 102(4):046808, 2009.
- [14] Nicolas Mounet and Nicola Marzari. First-principles determination of the structural, vibrational and thermodynamic properties of diamond, graphite, and derivatives. *Phys. Rev. B*, 71(20):205214, 2005.
- [15] P. K. Schelling and P. Keblinski. Thermal expansion of carbon structures. *Phys. Rev. B*, 68(3):035425, 2003.
- [16] Wenzhong Bao, Feng Miao, Zhen Chen, Hang Zhang, Wanyoung Jang, Chris Dames, and Chun Ning Lau. Controlled ripple texturing of suspended graphene and ultrathin graphite membranes. *Nat. Nano.*, 4(9):562–566, 2009.
- [17] Nachiket R. Raravikar, Pawel Keblinski, Apparao M. Rao, Mildred S. Dresselhaus, Linda S. Schadler, and Pulickel M. Ajayan. Temperature dependence of radial breathing mode raman frequency of single-walled carbon nanotubes. *Phys. Rev. B*, 66(23):235424, 2002.

- [18] Chunyu Li and Tsu-Wei Chou. Axial and radial thermal expansions of single-walled carbon nanotubes. *Phys. Rev. B*, 71(23):235414, 2005.
- [19] Young-Kyun Kwon, Savas Berber, and David Tománek. Thermal contraction of carbon fullerenes and nanotubes. *Phys. Rev. Lett.*, 92(1):015901, 2004.
- [20] H. Jiang, B. Liu, Y. Huang, and K. C. Hwang. Thermal expansion of single wall carbon nanotubes. *J. Eng. Mater. Tech.*, 126(3):265–270, 2004.
- [21] Jin-Wu Jiang, Jian-Sheng Wang, and Baowen Li. Thermal expansion in single-walled carbon nanotubes and graphene: Nonequilibrium green’s function approach. *Phys. Rev. B*, 80(20):205429, 2009.
- [22] Guoxin Cao, Xi Chen, and Jeffrey W. Kysar. Thermal vibration and apparent thermal contraction of single-walled carbon nanotubes. *J. Mech. Phys. Solids*, 54(6):1206–1236, 2006.
- [23] Daan Frenkel and B. Smit. *Understanding Molecular Simulation: From Algorithms to Applications*. Academic Press, 1996.
- [24] N. Metropolis, A. W. Rosenbluth, M. N. Rosenbluth, A. H. Teller, and E. Teller. Equation of state calculations by fast computing machines. *Journal of Chemical Physics*, 21:1087–1092, 1953.
- [25] J. Tersoff. Empirical interatomic potential for carbon, with applications to amorphous carbon. *Phys. Rev. Lett.*, 61(25):2879–2882, 1988.
- [26] Donald W. Brenner. Empirical potential for hydrocarbons for use in simulating the chemical vapor deposition of diamond films. *Phys. Rev. B*, 42(15):9458–9471, 1990.
- [27] Yutaka Maniwa, Ryuji Fujiwara, Hiroshi Kira, Hideki Tou, Hiromichi Kataura, Shinzo Suzuki, Yohji Achiba, Eiji Nishibori, Masaki Takata, Makoto Sakata, Akihiko Fujiwara, and Hiroyoshi Suematsu. Thermal expansion of single-walled carbon nanotube (swnt) bundles: X-ray diffraction studies. *Phys. Rev. B*, 64(24):241402, 2001.
- [28] Xueshen Wang, Qunqing Li, Jing Xie, Zhong Jin, Jinyong Wang, Yan Li, Kaili Jiang, and Shoushan Fan. Fabrication of ultralong and electrically uniform single-walled carbon nanotubes on clean substrates. *Nano Lett.*, 9(9):3137–3141, 2009.
- [29] J. H. Los, M. I. Katsnelson, O. V. Yazyev, K. V. Zakharchenko, and A. Fasolino. Scaling properties of flexible membranes from atomistic simulations: Application to graphene. *Phys. Rev. B*, 80(12):121405, 2009. doi: 10.1103/PhysRevB.80.121405.
- [30] N.W. Ashcroft and N.D. Mermin. *Solid State Physics*. Harcourt College Publishers, Orlando, 1976.
- [31] Linear algebra package. <http://www.netlib.org/lapack>.
- [32] Hendrik J. Monkhorst and James D. Pack. Special points for brillouin-zone integrations. *Phys. Rev. B*, 13(12):5188–5192, 1976.
- [33] C Kittel. *Introduction to Solid State Physics*. John Wiley & Sons, 2005.
- [34] Hartmut Zabel. Phonons in layered compounds. *J. Phys-condens. Mat.*, 13(34):7679, 2001.
- [35] J. Maultzsch, S. Reich, C. Thomsen, H. Requardt, and P. Ordejón. Phonon dispersion in graphite. *Phys. Rev. Lett.*, 92(7):075501, 2004.
- [36] Ludger Wirtz and Angel Rubio. The phonon dispersion of graphite revisited. *Solid State Communications*, 131(3-4):141–152, 2004.
- [37] O. Dubay and G. Kresse. Accurate density functional calculations for the phonon dispersion relations of graphite layer and carbon nanotubes. *Phys. Rev. B*, 67(3):035401, 2003.

- [38] Janina Zimmermann, Pasquale Pavone, and Gianaurelio Cuniberti. Vibrational modes and low-temperature thermal properties of graphene and carbon nanotubes: Minimal force-constant model. *Phys. Rev. B*, 78(4):045410, 2008.
- [39] M. Mohr, J. Maultzsch, E. Dobardžić, S. Reich, I. Milošević, M. Damnjanović, A. Bosak, M. Krisch, and C. Thomsen. Phonon dispersion of graphite by inelastic x-ray scattering. *Phys. Rev. B*, 76(3): 035439, 2007.
- [40] Susanne Siebentritt, Roland Pues, Karl-Heinz Rieder, and Alexander M. Shikin. Surface phonon dispersion in graphite and in a lanthanum graphite intercalation compound. *Phys. Rev. B*, 55(12): 7927–7934, 1997.
- [41] C. Oshima, T. Aizawa, R. Souda, Y. Ishizawa, and Y. Sumiyoshi. Surface phonon dispersion curves of graphite (0001) over the entire energy region. *Solid State Commun.*, 65(12):1601 – 1604, 1988.
- [42] R. Nicklow, N. Wakabayashi, and H. G. Smith. Lattice dynamics of pyrolytic graphite. *Phys. Rev. B*, 5(12):4951–4962, 1972.
- [43] H. Yanagisawa, T. Tanaka, Y. Ishida, M. Matsue, E. Rokuta, S. Otani, and C. Oshima. Analysis of phonons in graphene sheets by means of hreels measurement and ab initio calculation. *Surf. Interface Anal.*, 37(2):133–136, 2005.
- [44] F. Tuinstra and J. L. Koenig. Raman spectrum of graphite. *The Journal of Chemical Physics*, 53(3): 1126–1130, 1970.
- [45] L. Lindsay and D. A. Broido. Optimized tersoff and brenner empirical potential parameters for lattice dynamics and phonon thermal transport in carbon nanotubes and graphene. *Phys. Rev. B*, 81 (20):205441, 2010.
- [46] M. S. Dresselhaus and M. S. Dresselhaus. *Graphite fibers and filaments / M.S. Dresselhaus ... [et al.]*. Springer-Verlag, Berlin ; New York :, 1988.
- [47] V. K. Tewary and B. Yang. Parametric interatomic potential for graphene. *Phys. Rev. B*, 79(7):075442, 2009.
- [48] You Xiang Zhao and Ian L. Spain. X-ray diffraction data for graphite to 20 gpa. *Phys. Rev. B*, 40(2): 993–997, 1989.
- [49] M. Hanfland, H. Beister, and K. Syassen. Graphite under pressure: Equation of state and first-order raman modes. *Phys. Rev. B*, 39(17):12598–12603, 1989.
- [50] Jia-An Yan, W. Y. Ruan, and M. Y. Chou. Phonon dispersions and vibrational properties of monolayer, bilayer, and trilayer graphene: Density-functional perturbation theory. *Phys. Rev. B*, 77(12): 125401, 2008.
- [51] Hidekatsu Suzuura and Tsuneya Ando. Phonons and electron-phonon scattering in carbon nanotubes. *Phys. Rev. B*, 65(23):235412, 2002.
- [52] S. V. Goupalov. Continuum model for long-wavelength phonons in two-dimensional graphite and carbon nanotubes. *Phys. Rev. B*, 71(8):085420, 2005.
- [53] Lin-Hui Ye, Bang-Gui Liu, Ding-Sheng Wang, and Rushan Han. Ab initio phonon dispersions of single-wall carbon nanotubes. *Phys. Rev. B*, 69(23):235409, 2004.
- [54] I. M. Lifshitz. *Zh. Eksp. Teor. Fiz.*, 22:475, 1952.
- [55] Vasili Perebeinos and J. Tersoff. Valence force model for phonons in graphene and carbon nanotubes. *Phys. Rev. B*, 79(24):241409, 2009.
- [56] J. Tersoff. Energies of fullerenes. *Phys. Rev. B*, 46(23):15546–15549, 1992.

- [57] B. Yang and V. K. Tewary. Multiscale green's function for the deflection of graphene lattice. *Phys. Rev. B*, 77(24):245442, 2008.
- [58] K. V. Zakharchenko, J. H. Los, M. I. Katsnelson, and A. Fasolino. Atomistic simulations of structural and thermodynamic properties of bilayer graphene. *Phys. Rev. B*, 81(23):235439, 2010.
- [59] H.O. Pierson. *Handbook of Carbon, Graphite, Diamond and Fullerenes: Properties, Processing and Applications*. Noyes Publications, Park Ridge, NJ, 1993.
- [60] Jannik C. Meyer, A. K. Geim, M. I. Katsnelson, K. S. Novoselov, T. J. Booth, and S. Roth. The structure of suspended graphene sheets. *Nature*, 446(7131):60–63, 2007.
- [61] A.C. Bailey and B Yates. Anisotropic thermal expansion of pyrolytic graphite at low temperatures. *J. Appl. Phys.*, 41(13):5088–, 1970.
- [62] P. Souvatzis, O. Eriksson, M. I. Katsnelson, and S. P. Rudin. Entropy driven stabilization of energetically unstable crystal structures explained from first principles theory. *Phys. Rev. Lett.*, 100(9):095901, 2008.